*Prog. Oceanog.* Vol. 21, pp. 1–105, 1988.
Printed in Great Britain. 

0079-6611/88 $0.00 + .50


# The Flow of Atlantic Water Through the Strait of Gibraltar

DAVID M. FARMER* and LAURENCE ARMI†

# The Flow of Mediterranean Water Through the Strait of Gibraltar

LAURENCE ARMI† and DAVID M. FARMER*

*(Received 1 April 1988 and in final form 31 October 1988)*

**Abstract** — We describe and analyze observations of the water exchange through the Strait of Gibraltar. The primary observations were taken in April 1986 and included data from moored recording instruments at four locations in the strait, together with an intensive survey by ship. These measurements included extensive CTD profiling, acoustic Doppler current profiling, numerous profiles from expendable instruments, and imaging using a high-frequency echo sounder.

The analysis focuses on the internal hydraulics of the Strait and in particular the presence of hydraulic controls and their influence on the exchange. Our observations during April 1986 show that the maximal exchange condition, in which a subcritical flow is bounded by supercritical flow at both ends of the Strait, did occur, although with various subtleties not explicitly incorporated in our previous theoretical developments.

The Atlantic water, moving east along the surface, encounters a control at Tarifa Narrows in the eastern part of the Strait. The Mediterranean water passes through controls both at Camarinal Sill and at Spartel Sill, further west. At our westernmost mooring at Spartel, the outflowing Mediterranean water is continuously supercritical, with little tidal variability. The control at Camarinal Sill is periodically lost due to tidal action and reappears on a reverse flow during a falling spring tide. Tangier Basin, bounded by Camarinal and Spartel Sills, acts as an internal reservoir for the outflowing Mediterranean water, the interface rising and falling through each tidal cycle. During spring tides, the Tangier Basin interface rises high enough to flood the control at Camarinal Sill and produces a reverse flow of the lower layer. When control is lost at Camarinal Sill a travelling bore is released. This bore may modify the location of the control acting on the surface layer in Tarifa Narrows. The Atlantic water enters the Alboran Sea as a jet which may have a well-defined northern boundary where it separates from the European coast; this boundary may be identified by the presence of a slick. Although the internal jump west of Camarinal Sill is almost certainly an area of intense mixing, frictional effects do not appear to be dominant in the subcritical portion of the flow.

*Institute of Ocean Sciences, P.O. Box 6000, Sidney, B.C. V8L 4B2, Canada

†Scripps Institution of Oceanography, La Jolla, California, 92093, U.S.A.

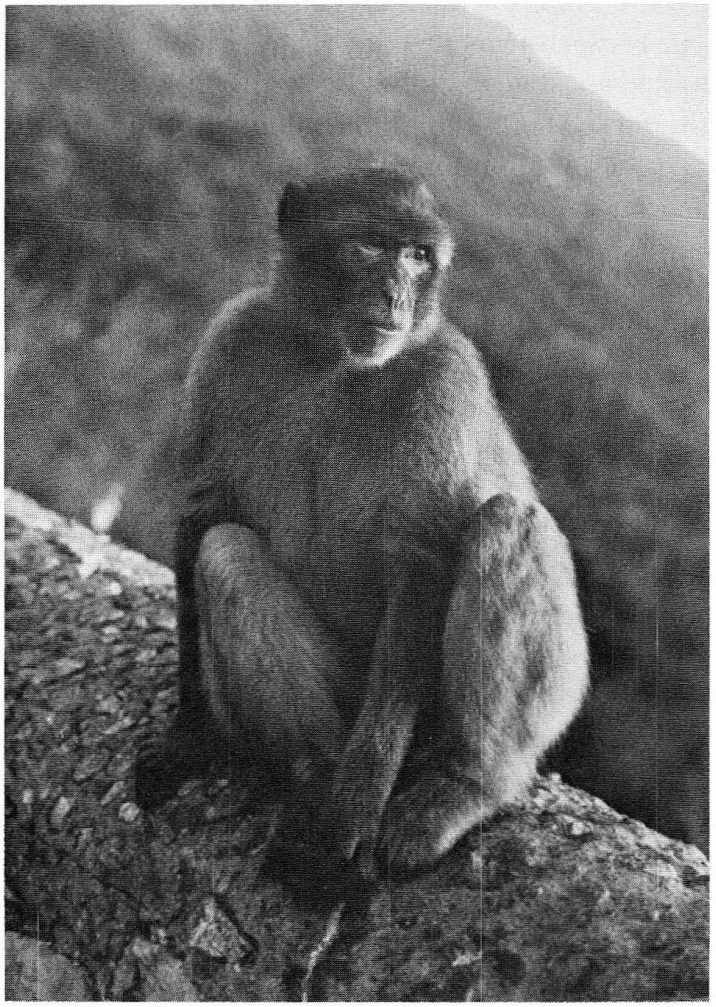

## DEDICATION

This work is dedicated to our friends, the Barbary Apes, who for centuries have observed the Strait of Gibraltar from their home on the Rock, and to our other stern critics and colleagues.

## 1. INTRODUCTION

The exchange of water of different density between two reservoirs is a fluid dynamical problem of long-standing interest, with many applications in natural and artificial environments. These include such diverse examples as the exchange of water of different density through a lock and the exchange of air between two adjoining rooms with a communicating door. In 1755 WAITZ described an experiment in which two lighted candles are used to indicate the direction of air flow between a warm and cold room; he proposed that the resulting air motion illustrated the essential hydraulic processes governing exchange in the Strait of Gibraltar (see DEACON, 1985). This model anticipates the hydraulically controlled exchange mechanism elaborated in ARMI and FARMER (1986) and FARMER and ARMI (1986), which forms a theoretical basis for the observations described in this paper.

The flow through the Strait of Gibraltar is an important, but by no means unique, oceanographic example of a controlled exchange. Its importance lies in the influence the exchange rate has on the salinity of the Mediterranean (c.f. BRYDEN and STOMMEL, 1984), and consequently also of the Mediterranean outflow, whose distinctive signature is apparent over large portions of the North Atlantic. However, the exchange through the Strait does differ in a fundamental way from Waitz's experimental model in that it is modulated and even reversed by the tide. In this paper we analyze the results of an experiment designed to study these hydraulic processes. Our work was a part of the Gibraltar Experiment (KINDER and BRYDEN, 1987) and is based on measurements obtained on the RV OCEANUS in April 1986, together with a pilot study carried out on the RV LYNCH during October 1985.

Following a series of earlier studies in the Strait (see DEFANT, 1961), a very extensive investigation of the physical oceanography, involving several ships, was carried out in the 1960s under the aegis of the NATO subcommittee of Oceanographic Research. Much of this work has been summarized by LACOMBE and RICHEZ (1982). This important set of data provided a basis for the preliminary hydraulic interpretation of flow through the Strait presented by ARMI and FARMER (1985) and provided a historical overview and motivation for the experiment described here. Moreover, a comprehensive atlas of hydrography and currents has recently appeared (LACOMBE and RICHEZ, 1984).

Much of the current interest in the oceanography of the Strait of Gibraltar has focused on the net exchange of water between the Atlantic and Mediterranean. However, these studies (c.f. BORMANS et al., 1986; BRYDEN and STOMMEL, 1984) did not focus on the details of the flow within the Strait, especially temporal fluctuations dominated by tidal forcing and spatial variability associated with the major topographic features.

The goal of the present study, however, is the development of a firm experimental basis for describing the relevant processes directly influencing the exchange over the full range of space and time scales. The exchange mechanism is inherently nonlinear; in fact, through much of the Strait the nonlinear terms in the equation of motion are dominant and the flow is well-approximated by the theory of internal hydraulics. This theory provides the framework for an interpretation of our data.

We begin with a discussion of the experimental techniques and our observational approach (Chapter 2). We review in Chapter 3 the essential concepts of two-layer hydraulic control. In Chapter 4 the observations are placed in the perspective of the overall exchange problem, and a detailed discussion of each section of the Strait follows in Chapters 5-9. Following discussion of seasonal measurements (Chapter 10), rotation effects (Chapter 11) and travelling bores (Chapter 12), the subject of mixing and frictional effects is addressed in Chapter 13. In the conclusion (Chapter 14) we summarize all of the preceding discussions, and readers may find it helpful to refer ahead to this chapter for additional perspective on the geographically distinct discussions of the preceding chapters.

## 2. EXPERIMENTAL APPROACH

The main experimental program, carried out during April 1986, included an extensive set of profile measurements using both expendable profilers and acoustic methods with the ship travelling rapidly, so as to acquire a picture of the dynamically important variables along the track. In addition, time series observations were obtained from the ship at certain key locations so as to determine the detailed structure of the tidal response. Complementing these measurements were data acquired simultaneously from moored recording instruments at four locations in the Strait. The combination of moored and ship-board data was considered essential to the proper description of the spatially and temporally variable flow.

It was central to our experimental approach that data be analyzed during the cruise, so that modifications to the plan could be implemented as appropriate. Data from all ship-board measurements were available for use during the cruise. A three-day break in the middle of the cruise was required for other components of the Gibraltar Experiment; however, this break proved fortunate in that it allowed us to evaluate the initial results and further plan the concluding section. Although the break in data collection over the neap tide does bias our results towards stronger tidal flows, it allowed a longer measurement period for the recording instruments which continued to operate throughout the fortnightly cycle.

Figure 2.1 includes a chart of the experimental area showing the principal ship tracks used during April 1986, together with mooring locations. These tracks consist of runs of various lengths along the axis of the Strait, which we subsequently refer to as 'runs', and tracks across the Strait, which we call 'transects'. ( Fig. 2.1 is based on Defense Mapping Agency (1980) Chart No. 52041; reference may also be made to a comprehensive chart published by Instituto Geográfico Nacional y SECEG, 1988.)

Figure 2.2 provides a detailed time-space history of each of the various components of the observational program. The vertical axis in this figure indicates the physical location of the measurements and is referenced to the adjoining chart. The time axis shows the time at which various ship tracks (runs, transects and time series) occurred, and the duration of moorings. Throughout this paper, times are given in UT. Numbered boxes, located in space and time corresponding to the observations, refer to the respective figures used subsequently. Time series measurements are indicated with stars. At the bottom of the figure we show tidal height predictions for Tarifa, provided to us by the Canadian Hydrographic Service using data from the International Hydrographic Bureau Data Bank.

The paths of the longitudinal runs represent a compromise between the need to obtain profiles along the east-west axis of the Strait, passing over the primary topographic features, and the navigational requirements of ship traffic separation. Positioning was achieved using radar ranging together with visual bearings where appropriate. For navigational simplicity the tracks were chosen, so far as possible, to be straight; ship positions were kept to within 0.3 nautical miles of the tracks, with deviations occasionally necessitated by traffic conditions.

An initial cruise, making use of limited access to available ship time during October 1985, allowed the acquisition of a preliminary data set. While these data lack the range of measurement approaches and the systematic sampling that was possible during the April 1986 cruise, they nevertheless provide valuable insight on the extent to which our April data is representative of conditions at other times.

*Moored instruments*

The moorings included a total of 13 Aanderaa current meters fitted with thermistors, conductivity sensors and, on some instruments, pressure sensors (see Figure 2.3). The moorings also included 10 thermistor chains. Although data from the thermistor chains have not been explicitly incorporated in any of the figures in this paper, the temperature data were used to provide supporting evidence for our interpretations. It was recognized that the strong currents in the Strait of Gibraltar required special care in mooring design and the use of substantial buoyancy and corresponding anchors, and of heavy mooring wire with extensive corrosion protection. As expected on the basis of our preliminary mooring modelling (c.f. BELL, 1979), large vertical excursions of the instruments were unavoidable. Thus pressure measurements were essential and were included on all moorings. The Aanderaa design with its gimballed mounting is particularly suitable for moorings subject to significant inclinations in strong currents. The moorings were installed at the start of the April 1986 cruise and recovered at the end (see Figure 2.2). Prior to deployment, all thermistors and conductivity sensors were calibrated; the measurement accuracy and resolution for these and other instruments used in the experiment is shown in Table I. With only two minor exceptions (the conductivity sensors on the 195 m current meter at Camarinal Sill and the 130 m current meter in Tarifa Narrows), all instruments yielded results consistent with independent hydrographic measurements. For the two instruments that deviated in this comparison, a conductivity bias has been corrected in the resulting data.

*Expendable and CTD profile measurements*

Two types of expendable profilers were used while the ship was underway: expendable bathythermographs (XBT), to provide temperature profiles, and expendable sound velocimeters (XSV), to provide sound speed profiles which could be used in conjunction with the temperature profiles to generate salinity and density profiles. When both XBT and XSV were used together, they were deployed simultaneously from opposite sides of the ship's fantail. Nevertheless, discrepancies in the designed drop speed, spatial variability in the salinity-temperature structure and other factors produce unavoidable differences in the sampled volume, which leads to spikes in the computed salinity and density profile. These, however, do not detract from the value of

simultaneous XBT/XSV profiles for identifying the depth of the pycnocline. Following analysis of the computed salinity profiles, it was determined that spiking could be minimized by using an XSV drop rate of 0.985 that of the manufacturer's specified value. More XBTs were available than XSVs, and we therefore used simultaneous drops more frequently at the western end of the Strait, where the ambiguity in use of temperature profiles to locate the pycnocline is more pronounced. An example of XBT, XSV and inferred salinity and density profiles, together with a nearly simultaneous CTD profile, is shown in Figure 2.4. The offsets in computed salinity and density that are apparent in this figure are due primarily to errors in the XBT temperatures. They are removed in subsequent figures under the assumption of horizontal uniformity in the deep (>300 m) water properties.

Conductivity-temperature-depth (CTD) profiles were obtained at the ends of most of the along-strait runs and also during time series stations. For time series measurement the instrument was profiled continuously. With surface currents often reaching 2.5 m $s^{-1}$ it was necessary to operate the CTD from the vessel's stern and to use 100 kg additional ballast. A CTD mounted acoustic pinger and a towed hydrophone were used to control the depth of each profile to within a few meters of the bottom.

The CTD that we used was unique in having an extra sensor head and redundant conductivity, temperature (platinum resistance thermometer) and pressure sensors. This allowed us to monitor continuously the pairs of sensors with respect to each other. No relative changes were found for any of the sensors. Occasional surface and bottom salinity and temperature bottle samples were taken to supplement the calibration data acquired before and after the cruise.

*Acoustic measurements*

Two acoustic instruments were used from the ship: an acoustic Doppler current profiler and a high-frequency echo-sounder. The echo-sounder is used as a flow visualization device to provide graphic images of the internal structure of the flow. Sound is scattered by zooplankton, small fish, bubbles and temperature microstructure. To the extent that these are distributed coherently with the density structure of the flow, the echo-sounder images can be used to visualize the dynamics. Some care is necessary in the interpretation, since the acoustic targets, especially the phototaxic zooplankton, have individual behavioural patterns. For example, a cloud of plankton may occur somewhat above or beneath the pycnocline; however, the pycnocline itself usually appears as a recognizable feature. The utility of acoustic imaging is greatly enhanced by simultaneous temperature or density profiles. The acoustic image then serves as a guide to the interpolation and interpretation of data obtained with expendable profilers while the ship is underway, or with CTD profiles when a time series is being collected at one location. The echo-sounder output was recorded using Pulse Code Modulation and a video cassette recorder. This allowed recordings to be replayed later with optimum facsimile adjustments.

Velocity profiles were obtained with a ship-mounted acoustic Doppler current profiler. In order to avoid cross-talk between the Doppler profiler and echo-sounder, both instruments had a common trigger. While Doppler profiling systems are becoming quite widely used for oceanographic measurements, there are a number of subtleties associated with their calibration (see for example, HANSEN, 1985) and with the optimum processing of their output (see ZEDEL

and CHURCH, 1987). However, in this study we have used the Doppler data without special corrections and have accepted the manufacturer's calibrations (see Table I). This necessarily leaves some uncertainty as to the expected errors in velocity profile measurement. However, our observations were consistent with moored current meter data collected simultaneously. The Doppler profiler has the facility for acquiring bottom track velocity over a limited depth range, and where this has been obtained it has been incorporated in the profiles with figures marked 'abs' for 'absolute' or bottom referenced data, and 'rel' for 'relative' or unreferenced data.

As an example of the application of these various observational techniques, Figure 2.5a,b shows the structure of flow over Camarinal Sill during a strong outflow. The overlay of Figure 2.5a shows XBT profiles; the overlay of Figure 2.5b shows Doppler velocity and moored current meter data. The ship is travelling from east to west in this example, thus determining the orientation of the image. Two scattering interfaces can be seen. The uppermost corresponds to the primary pycnocline, but a small temperature step is co-located with the lower interface. The scattering strength is not necessarily directly related to the size of the temperature step, since the targets are primarily biological. The acoustic image shows that the interface deepens rapidly and irregularly as the water moves west over the sill, before returning to subcritical flow via an internal hydraulic jump. The interface deepens from 25 m to 200 m as the water moves from upstream to downstream conditions. This asymmetry in the interface is a key indication of the hydraulic conditions of the flow; in this particular case the transition is from subcritical upstream of the crest, to supercritical downstream of the crest and then back to subcritical following the internal hydraulic jump in Tangier Basin. These hydraulic conditions are also identified on the overlay of Figure 2.5a. The temperature structure in the XBT profiles is referenced to the location of the drop both by the solid circles at 13.5°C and by the solid triangles below. This reference temperature was chosen so as to delineate the interface, and provides a reasonable representation of the pycnocline location for April (see LACOMBE and RICHEZ, 1982). As is apparent from the figures, a 0.2°C instrumental error would result in a pycnocline depth error of order 5 m. The deflection of the interface is also apparent in the temperature profiles which serve to reinforce the interpretation of the acoustic image. The moored current meter data are shown on the overlay of Figure 2.5b at the depth of measurement, corrected for mooring response to the current on the basis of the pressure measurements.

In this area strong echoes from the sea-floor allowed satisfactory correction to the Doppler profiles for ship motion, yielding absolute velocities. In this figure, as in others having Doppler velocities, only the along-strait component is shown. In general, cross-strait components are relatively small, although cross flows do occasionally occur near the sill at certain depths. The simultaneous moored current meter data are consistent with Doppler velocity profiles.

This image also provides an example of the rich variety of biological and physical phenomena contributing to the backscatter, and indeed, of the adaptation of the biology to the physical processes. Except very close to the surface, where scatter from bubbles dominates and is closely associated with the surface slicks that can be seen from ships and in satellite images (see photograph from shuttle on cover), most of the backscatter is from fish or zooplankton. The large, dark patch in the echo-sounding, downstream of the hydraulic jump, is almost certainly a dense school of fish. The traces of individual fish passing through the acoustic beam can be seen upstream of the fish school. Coherent movements of large numbers of fish following the same patterns on each cycle of the tide are a common feature over sills (FARMER and SMITH, 1980),

and in Gibraltar are certainly known and were exploited by the fishermen during our cruise. Intensive fishing west of the sill sometimes impeded our ability to take measurements. Dolphins also frequent the sill and their distinctive sonar signatures are readily detected as a series of pulses on the echo-sounder trace (see Figure 2.5a overlay).

The detailed acoustic image in Figure 2.5a,b was obtained by moving the vessel quite slowly over the sill. Images acquired when the ship was travelling fast, as required for a rapid sequence of 'snapshots' through the tidal cycle, are less clear although still useful as a visual guide to the flow structure.

## 3. ESSENTIAL CONCEPTS OF TWO-LAYER HYDRAULIC EXCHANGE FLOWS

Hydraulic control is a fundamental concept of fluid dynamics. For a single layer flowing through a constriction, for example over a sill or through a contraction, the height of the upstream reservoir, together with the control, uniquely establishes the flow. The control condition is usually expressed in terms of the Froude number $F^2 = u^2/gy$, with the critical condition

$$F^2 = 1. \tag{1}$$

Here, u is the speed and y is the fluid depth (see, for example, HENDERSON, 1966).

For two layers, such as occur in the Strait of Gibraltar, it is convenient to use a composite Froude number,

$$G^2 = F_1^2 + F_2^2 \tag{2}$$

where the subscripts 1 and 2 refer to the upper and lower layer respectively, and where

$$F_i^2 = u_i^2 / g' y_i \tag{3}$$

and $g' = (\Delta\rho/\rho)g$ is the reduced gravity based on the density difference between the two layers. The internal control condition is

$$G^2 = 1. \tag{4}$$

In what follows we outline some of the key ideas of two-layer exchange flows. A detailed discussion of two-layer hydraulics is contained in ARMI (1986).

We are interested here in the case of an exchange flow through a constriction, in which the water in each layer moves in opposite directions between the two reservoirs. We initially identify the essential concepts of the quasi-steady theory, although we caution the reader that the primary papers (ARMI and FARMER, 1986 and FARMER and ARMI, 1986) should be consulted for a more complete discussion. A single control, satisfying (4), together with a reservoir condition, namely the interface depth on the subcritical side of the control, fully defines the exchange flow. This will be true even if the flow rate is different in the two layers, provided that the difference is known; such a differential flow rate represents the barotropic forcing. The position of the interface in the upstream reservoir determines the exchange rate in conjunction with the control.

When two controls are linked by a subcritical flow, the exchange rate is fully defined without reference to reservoir conditions. The addition of the second control replaces the requirement for specifying the upstream reservoir interface heights. This important concept, which plays a central role in our discussion of the Strait of Gibraltar, is referred to as a maximal exchange. The point that should be noted here is that a maximal exchange is an exchange that is completely determined by the processes occurring within a control region bounded by the two controls, together with the density difference between the exchanging water masses and the barotropic forcing.

A hydraulic control represents a transition between subcritical and supercritical flow. For a maximal exchange the two controls are joined by a subcritical flow; the flow just outside the control region, on both sides, must therefore be supercritical. When a maximal flow occurs, the exchange rate is greatest. A submaximal exchange, such as occurs with only a single control and the influence of an upstream reservoir condition, can never result in an exchange rate that exceeds the maximal exchange, and will generally produce smaller exchange rates.

A maximal exchange is sketched in Figure 3.1. In this example the two controls are located at a contraction and a sill and, as required, are connected by a subcritical flow. Supercritical flow ($G^2 > 1$) occurs both to the left of the sill control and to the right of the control at the contraction. Interfacial disturbances in the reservoirs cannot propagate through these two supercritical flows and into the control region. It is this feature that serves to isolate the control region from the reservoir conditions and allows the unique determination of the maximal exchange rate.

The concept of maximal exchange is not limited to an ideal frictionless flow. Friction may, and often will, be a significant component of the exchange dynamics within the control region. The presence of frictional effects will reduce the maximal exchange below that for the inviscid case and increase the complexity of the calculation of flow rates, but does not prevent the existence of the maximal exchange. ASSAF and HECHT (1974) have treated the case of a long strait within which a frictionally balanced flow is bounded by controls at both ends; the supercritical flow at each end isolates the flow in the strait from the reservoir conditions and therefore ensures maximal exchange. Provided that these supercritical flows occur, the exchange will always be maximal. It will subsequently be shown (Chapter 13) that friction has a small or negligible effect on the subcritical section of the Strait of Gibraltar, so that the flow is appropriately analyzed in terms of inviscid internal hydraulics.

In just the same way as frictional effects can occur within the control region, so also can time dependent effects occur without violating the essential concept that the details of the control region remain isolated from the reservoirs, and in fact such time dependence is a key element of the flow in the Strait of Gibraltar. As before, the essential requirement is that the control region be bounded by supercritical flows, although the complexity will again be greatly increased. Finally, mixing between the layers may occur within the control region, and thus modify the relative density difference that drives the flow; again, the determining requirement for maximal exchange is the presence of supercritical flow on either side of the control region.

These considerations serve to emphasize the primary observational step in a hydraulic study of a strait. If it can be shown that supercritical flow bounds the strait at both ends, then it has been demonstrated that the exchange is maximal (ARMI and FARMER, 1987). The details, however, may be very complicated, and the calculation of the resulting exchange rate will

require a thorough understanding of processes within the control region. Nevertheless, the existence of maximal exchange also results in an important simplification in that calculations of the exchange require no knowledge of processes occurring within the two reservoirs. ARMI and FARMER (1986, 1987) and FARMER and ARMI (1986) have analyzed the inviscid, quasi-steady case for a range of topographic conditions and barotropic forcing. The reader is referred to these papers for a full discussion of the maximal exchange problem.

The exchange through the Strait of Gibraltar can be interpreted in terms of the concepts outlined above. Figure 3.2 shows a sketch of a hypothetical steady state interface height through the Strait and the key topographic features that can determine the location of controls. The Mediterranean Sea is the source of dense, high salinity water ($\rho_2$), the Atlantic is the source of low salinity water ($\rho_1$). This two-layer representation implicitly incorporates in the deeper layer the various water types that are known to flow out through the Strait. For example, Mediterranean deep water is known to pass west through the Strait (KINDER and PARILLA, 1987). These Mediterranean water types have very similar densities, and we subsequently refer simply to Atlantic and Mediterranean water. There is a deep (~800 m), narrow section (Tarifa Narrows) to the east, a broader, relatively shallow (~280 m) sill (Camarinal) just west of the contraction, and a second sill (Spartel) further west. To the east we expect the Alboran Sea to be subcritical ($G^2 < 1$). The dense water flows slowly west through the narrow section and accelerates over Camarinal Sill, which acts as a control ($G^2 = 1$). In this steady state representation, we have sketched the Atlantic water flowing east above the denser layer. In contrast to the deeper flow, it accelerates through the narrow section in a progressively thinner layer. At some point within the contraction, the surface layer accelerates to the point at which a second control can occur, to the east of which the flow will become supercritical ($G^2 > 1$). Still further east, as the Atlantic water flows into the Alboran Sea (the western portion of the Mediterranean Sea), there is a transition back to subcritical flow. If this situation occurs, we see that the essential requirements of a maximal exchange are met. There is a supercritical flow just west of Camarinal Sill, and a supercritical flow in the eastern portion of the narrow section of the Strait. These supercritical flows are connected by a subcritical flow ($G^2 < 1$) lying between the two controls.

How would the second sill, at Spartel, influence this exchange? In the steady state representation of Figure 3.2, the supercritical flow to the west of Camarinal Sill is matched to conditions in Tangier Basin by a hydraulic jump. If, however, the interface in Tangier Basin were to rise, the position of the jump would move east, towards Camarinal Sill. If the interface becomes high enough, that is, if, in the inviscid case, it rises to the same depth as the interface east of Camarinal Sill, the jump will travel over the sill and this local control is lost. This condition is called a flooding of the control.

The Mediterranean water flows out of Tangier Basin over Spartel Sill, which also acts as a control, before running down the sloping sea-floor into the Atlantic as a supercritical flow. If the steady state representation in the figure actually occurred, nothing that happened in Tangier Basin, or over Spartel Sill, would influence the maximal exchange. In fact, the supercritical flow on the western flank of Camarinal Sill would isolate the exchange control region from these processes, just as the supercritical flow in the eastern part of the Strait would isolate the exchange control region from processes occurring in the Alboran Sea.

Despite the simplifications of a steady state representation, the basic hydraulic concepts outlined above and sketched in Figure 3.2 provided a useful starting point both for planning our experimental work in the Strait and for analyzing the results. Clearly, the key issues to be resolved turn on the existence and behaviour of the two controls that bound the subcritical flow in the central part of the Strait. As will subsequently be shown, the controls are strongly time dependent and, in fact, the control at Camarinal Sill is periodically lost, so that the exchange control region can extend west to Spartel Sill. This greatly complicates the interpretation, but, as will become apparent from the experimental results, the basic conceptual framework presented above remains valid and self-consistent.

*Calculation of Froude Numbers*

The Strait of Gibraltar is strongly stratified, having two well-defined water masses separated by a relatively sharp pycnocline. It is therefore well-approximated by a two-layer representation. Nevertheless, the density profiles, and especially the velocity profiles, do not always exhibit a simple step-like structure, and it is necessary to devise an operational definition of a Froude number for practical application to the large numbers of profiles.

Our operational definition uses $2\sigma_\theta$ units of density as the pycnocline step. If there is a nearby current meter within the layer of interest, we use the observed current speed. For example, the density profile at about 37W in Figure 4.1 has a step at 350 m in water 390 m deep. A nearby current meter within the lower layer showed a velocity of 1.53 m $s^{-1}$. For the lower-layer thickness of 40 m, this yields an internal Froude number (equation 3) of $F_2^2 \simeq 3$, which is indicated at the top of the figure above the profile. For the upper layer, a similar calculation yields $F_1^2 \simeq 0.01$, since the velocity is weak and the layer depth is large.

When a Doppler profile is available, the velocity of each layer is taken from the portions of the Doppler profile which are nearly uniform. The position of the interface is taken as before. For example, the profile in the Tangier Basin at 16W in Figure 4.1 has a representative upper-layer velocity of 0.4 m $s^{-1}$ and an interface depth of 175 m, yielding a Froude number of 0.05. The original calculations were made from profiles plotted at five times the scale of these figures.

The computation of the Froude number in the eastern part of the Strait is not as straightforward. Some of the velocity profiles are sheared over some depth, and the density profiles are almost exponential. Moreover, the vertical profiles of velocity and density structure vary across the Strait. A formal definition of the composite Froude number in this environment would require detailed information on both the vertical and transverse horizontal density and velocity field. The operational definition that we used for obtaining the upper-layer Froude number in the eastern part of the Strait was to take the interface at $28.0\sigma_\theta$ (c.f. Figure 8.6) and velocity at the mid-depth of the respective layer. For our April data a density difference of $2\sigma_\theta$ was the appropriate value and used throughout. At other times of the year a slightly different value may be appropriate.

## 4. OBSERVATIONAL OVERVIEW

The observational program focused both on long runs down the axis of the Strait, time series, short runs and transects over specific topographic features of particular relevance to the hydraulics. The controls identified in our analysis of historical data include Spartel Sill, Camarinal Sill and Tarifa Narrows. These controls are most usefully put into perspective by referring to Figure 4.1, which shows an echo-sounding together with XBT, density and velocity profiles.

At the western end of the Strait, the Mediterranean water flows out over Spartel Sill before running down the Atlantic slope. Spartel Sill is broad. As will subsequently be shown, the flow over the western portion of the sill is supercritical, and thus controls the outflow from Tangier basin. West of the sill, the sea floor slopes down to the Atlantic without major obstructions (HEEZEN and JOHNSON, 1969, and KENYON and BALDERSON, 1973, give detailed topographic information on this area). Tangier Basin separates Spartel Sill from Camarinal Sill; it has an irregular floor up to ~600 m in depth. The flow in Tangier Basin is always subcritical and, as will be shown later, plays an important role as an internal reservoir in determining the tidal response and exchange rate of the Strait.

Camarinal Sill has historically been regarded as the control location for models of flow through the Strait of Gibraltar (BRYDEN and STOMMEL, 1984, HOGG, 1985). Its deepest point is ≃ 280 m, which is approximately 40 m less than Spartel Sill. Our observations show, however, that although this sill has an important influence on the hydraulic exchange, control is not always maintained throughout the tidal cycle at this location, especially during spring tides. Between Camarinal Sill and Tarifa, the Strait deepens and narrows; the flow in this area is always subcritical. Within Tarifa Narrows the interface between Atlantic and Mediterranean water becomes shallower to the east and the surface layer travels faster, passing smoothly through the critical condition. At the eastern end of Tarifa Narrows the effect of rotation becomes important and the Atlantic inflow can separate from the north shore before entering the Alboran Sea.

It was apparent both from the historical observations and our theoretical analysis that it was essential to understand the tidal response if we were to develop an adequate explanation of exchange processes in the Strait. Our experiment was therefore designed to extend over a full spring-neap cycle, as indicated in Figure 2.2.

Our mooring locations were chosen partly so as to ensure that we detected the Mediterranean outflow at some point where it was supercritical in the western part of the Strait. Two locations (Spartel West and Spartel East) were used, since there was some uncertainty as to the precise location of the Spartel control; the final location of the moorings was determined at sea.

A mooring was placed in Tarifa Narrows in an attempt to measure fluctuations in the surface layer. It was recognized that the depth of water (>800 m) and the strong surface flow (2.5 m $s^{-1}$) would cause problems in maintaining the correct instrument depth; nevertheless this record, obtained concurrently with our ship-board observations, proved very useful.

Camarinal Sill was also instrumented with the shallowest current meter at a nominal depth of 75 m. Here also, the strong currents produced substantial vertical displacement of the instruments. Where appropriate we have used the measured pressures to interpolate our observations and correct for the effect of the mooring motion.

## 5. CONTROL OF THE INTERNAL RESERVIOR: SPARTEL

Figure 5.1 shows the results of a transect across the western exit of the Strait, Spartel West, bounding the deep Mediterranean outflow both to the north and south. The acoustic image clearly illustrates the inclined interface rising from ~300 m in the south to ~200 m in the north. This inclination is a consequence of rotation. The overlay confirms the interpretation of the acoustic image. The outflow has a maximum observed speed of 0.8 m $s^{-1}$; however, the Doppler measurement fails to provide useful data near the sea floor, both because of side lobe interference of the sloping acoustic beams and because of range limitations. As shown below, the speed 25 m above the sea floor recorded nearby at the Spartel West mooring is 1.25 m $s^{-1}$. Recorded current meter values at the two shallower depths are consistent with the Doppler data.

Acoustic images made during a run (see Figure 4.1) show several lines of increased backscatter sloping downwards to the west. These lines are associated with steps in the temperature and density profiles. In Tangier Basin the slope of the interface is approximately 1:1000. Over Spartel Sill deeper interfaces, which are less clearly resolved in Figure 4.1 though clearly evident in the temperature profiles, show a much greater slope, of order 1:40. It is the deeper interfaces that separate the outflowing Mediterranean water from the Atlantic inflow. The Mediterranean water is confined to a relatively thin (~100 m) layer which runs at approximately 1.5 m $s^{-1}$ down the western slope. At Spartel Sill the flow is often, but not always, controlled and is dominated by the deeper layer.

A prominent temperature minimum appears just above the outflow (Figures 4.1 and 5.1) and evidently represents cooler water, selectively withdrawn from the Atlantic. This anomalous feature is smeared out in the sheared flow, especially over Camarinal Sill and further east, but is often detectable throughout the western part of the Strait.

Time series measurements of currents, temperature and salinity show the way in which tidal modulations are reduced as the Mediterranean outflow travels down the slope of Spartel West . Figure 5.2, from the Spartel West mooring, includes one current meter at 395 m (25 m above the sea-floor), deep within the outflow. The current runs steadily west at about 1.4 m $s^{-1}$, with a tidal variation of less than 20%. At 335 m the current meter lies just within the outflow, implying a total lower-layer thickness of approximately 100 m; vertical excursions of the sheared, interfacial boundary produce a large tidal modulation of the current at this depth. Both of the shallower current meters lie within the Atlantic inflow at all times. The pressure sensor for the shallowest current meter indicates a maximum vertical motion of about 5 m. This mooring was only slightly affected by fluctuations in the tidal current.

The overlay to Figure 5.2 shows corresponding salinities recorded by each instrument. At the deepest location (395 m) there is a marked change in character and in average value of the salinity time series between the first few days of the mooring (7-14 April) and the remainder.

The variability diminishes during the neap tide. There is also a modest, but quite detectable, increase in velocity during this period of neap tide. Similar, though weaker, effects appear at the shallower instrument (335 m).

Figure 5.3 shows data from the mooring at Spartel Sill, which is located at position 20W (see Figure 2.1) on a steep slope. Here, tidal modulation of the current is stronger, but it is clear that both of the deeper instruments lie within the Mediterranean outflow. The vertical excursions of the upper instrument reach a maximum of 70 m during spring tides and 10 m on neap. The overlay also shows the pressure readings from the middle instrument; these mimic those of the uppermost current meter, for which the pressure readings are shown with the velocities. These vertical excursions, however, cannot explain the fact that the 290 m instrument detects a current speed greater than that observed at 350 m during the strong spring tides. The mooring was located in an area downstream of the sill crest where it appears that there was partial separation of the flow from the steep crest of Spartel Sill, augmented by the upstream effect of Spartel West, the crest of which is actually shallower than our deepest instrument at this mooring. The 230 m instrument lies close to the average level of the interface, implying a lower-layer thickness of ~150 m, which may be compared with the 100 m thickness 17 miles downstream, at the Spartel West mooring.

## 6. THE INTERNAL RESERVIOR: TANGIER BASIN

The Tangier Basin, lying between Spartel and Camarinal Sills, has an important influence on the exchange processes in the strait. This basin acts as a reservoir or catch-basin for Mediterranean water; the interface level varies with the tide and can be high enough to flood the control at Camarinal Sill and even reverse the outflow of the deeper layer.

A transect between Cape Spartel and Cape Trafalgar passes 4 miles east of the Spartel Sill mooring (shown in Figure 6.1). At this location the outflow is locally divided by a shallow area referred to as The Ridge (LACOMBE and RICHEZ, 1982). The interface is inclined between 200 m and 100 m, with lower-layer speeds of 0.6-0.8 m $s^{-1}$. While it is tempting to carry out a geostrophic calculation for data such as Figure 6.1, there are difficulties associated with the resulting interpretation, which are discussed in Chapter 11.

The way in which the interface in Tangier Basin rises and falls, as the basin successively fills and drains with Mediterranean water on each tide, is in part illustrated with the time series obtained at station 14.5W in Tangier Basin (Figure 6.2). The isopycnals between (27.0 and 29.0) are calculated from CTD profiles obtained at approximately 10 minute intervals. The overlay includes the corresponding Doppler profiles.

In order to obtain an overall view of the response of Tangier Basin to transports over the sills, we carried out a sequence of runs back and forth between Camarinal and Spartel. Only two of these runs are shown here (Figure 6.3a,b), corresponding to a spring tide during which flow reversal took place over Camarinal Sill. The important point to note here is that the vertical excursion of the pycnocline in Figure 6.1 corresponds not to an internal wave, but rather to the filling and draining of Mediterranean water in Tangier Basin. As an aid to comparison of interface displacements in these two figures, a horizontal line has been drawn at 150 m; this is approximately the mid-depth about which the interface moves through the tidal cycle.

The run in Figure 6.3a shows Tangier Basin filled with Mediterranean water and with the interface at 120 m. A complex multiple control can be seen in the Spartel area (see especially the acoustic image). At Camarinal Sill the Mediterranean water nearly reaches the surface and is flowing into the basin at 1.2–1.5 m $s^{-1}$. Finestructure in the XBT profile just west of the sill suggests active mixing down to 250 m.

Seven hours later, the last run in the sequence, Figure 6.3b shows the interface in Tangier Basin at 220 m, the deepest recorded during this series. In comparison to all previous runs, the outflow over Spartel Sill is weak and restricted to the deepest measurement. Flow over Camarinal Sill is dominated by the eastward flow of Atlantic water. Only the deepest Camarinal instrument lies in Mediterranean water and the flow into Tangier Basin is weak. This image is typical of the end of the draining cycle.

This combination of time series measurements at a single location (Figure 6.2) and sequential runs (two examples of which are shown in Figure 6.3) demonstrate the response of Tangier Basin to the tidal forcing. As will be discussed, the basin acts as an internal reservoir that periodically floods the control at Camarinal Sill, thus playing a key role in the hydraulic mechanisms that govern exchange of water through the Strait of Gibraltar.

## 7. CAMARINAL SILL

Historically Camarinal Sill, which is the shallowest passage between the Mediterranean and the Atlantic, has been regarded as the location of primary importance in controlling the exchange. Travelling west from the Alboran Sea, the bottom rises abruptly from 800 m in the narrowest section of the Strait, to less than 300 m over the sill. A feature of the topography, that bears on the subsequent hydraulic discussion, is that the channel width is significantly greater at the sill than it is further east at Tarifa. Figure 2.1 shows the location of the sill and Figure 2.3 the mooring in this part of the Strait.

Camarinal Sill is a topographically complex structure; although the overall influence on the flow can be modelled by a two-dimensional obstacle, the interfacial displacements are closely coupled through the internal hydraulic response to the local depth of the sea floor, which is highly variable over small scales. Measurements taken at a fixed location, specifically a mooring, can provide a useful time series which can be interpreted in terms of the tidal forcing. Similarly, a run over the sill along the axis of the Strait yields a usefully interpretable view of the baroclinic response providing that it is referenced to the local depth. On the other hand, some care is required in the interpretation of repeated measurements from a ship at the same location. A related problem arises in transect observations across the sill. The crest of the sill does not follow a straight line, so that the measurement of the interface depth will be sensitive to the course steered by the ship. Nevertheless, Figure 7.1 is included to show the general features. During this transect the flow was to the west throughout the water column, with the interface at a depth of approximately 80 m.

A time series was obtained at Station 7W over the crest of Camarinal Sill (Figure 7.2). The prominent feature of this time series is the rise and fall of the interface in response to barotropic forcing. This response is consistent with the prediction based on our hydraulic model (see Chapter 3), and is further discussed in Chapter 14. The Doppler velocity profiles show that at this location the portion of the profile that is sheared corresponds with the pycnocline.

Figure 7.3 displays an expanded plot of currents during the period of measurements shown in Figure 7.2. Note that the current recorded by the deepest instrument (255 m) is an outflow throughout the period of the time series measurements which are here indicated by a horizontal bar in the figure, with the speed dropping almost to zero during inflow. Moreover, the Atlantic water does not penetrate to the lower instruments. During inflow, therefore, control is lost at the sill, since the lower layer is essentially motionless.

Figure 7.4 shows a sequence of runs across Camarinal Sill, together with XBT and moored current meter data, obtained at different phases of the tide on 8 through 9 April. The times at which the vessel passed over the sill crest are indicated in the expanded current time series shown in Figure 7.5. In Figure 7.4a, both layers move west under the influence of a tidal outflow. Although the current meters in these figures (7.4a-h) only record the flow in the deeper layer, the simultaneous westward flow of the upper layer during this phase of a strong tide can be seen in Figures 2.5b and 7. The interface plunges down over the western face of the sill, but is subject to irregularities and a convergence of the isotherms. The temperature profiles clearly illustrate the return to subcritical flow downstream of the sill in the Tangier Basin.

Two hours later (Figure 7.4b) the current has slackened somewhat, but the whole water column continues to move west over the crest. Strong mixing persists and the interface deepens to the west of the sill.

In Figure 7.4c the surface layer has switched to an eastward flow; the Mediterranean water continues to move west into Tangier Basin, but at a much reduced speed. While the temperature structure in the vicinity of the sill remains disturbed, the large lee wave or jump apparent in Figure 7.4a, b is no longer present.

In Figure 7.4d the entire water column is moving east over the sill crest. This is representative of reverse flow; the interface depth in Tangier Basin is high enough to permit Mediterranean water to drain out at both its eastern and western ends. At the eastern end of Tangier Basin, Camarinal Sill now controls the Mediterranean water as it flows out of Tangier Basin back to the Mediterranean Sea. The interface first rises and then drops rapidly on the downstream (i.e. east) side of the sill. In this case, the upper layer is accelerated across the sill and moves faster than the deep layer. This may be an example of a rather special type of control, referred to as an approach control and described by FARMER and DENTON (1985), in which the critical condition occurs upstream of the sill crest; flow over the crest is supercritical and the upper layer dominates the dynamics. This type of control is identified by the symmetry in the interface on either side of the sill crest, but only in the immediate vicinity of the crest .

Figure 7.4e shows conditions shortly before the end of the period of reverse flow of the lower layer. The surface layer deepens symmetrically over the sill crest implying subcritical flow.

When the tide changes to an outflow, the surface layer initially remains almost motionless (Figure 7.4f). The Mediterranean water travels west and the interface dips down on the lee of the sill before jumping back up to match the Tangier Basin interface height. Thus, the sill controls the lower layer and the surface flow is essentially passive.

In Figure 7.4g, a strong outflow forces both layers west over the sill, and as expected, the interface plunges deeper on the downstream side. However, in this case, it can be shown that the flow is supercritical upstream (to the east) of the crest, as was also the case for flow in the opposite direction in Figure 7.4d, and therefore may also be an example of an approach control.

The final run (Figure 7.4h) was carried out during a strong westward flow. A deflection of the interface, from 50 m to over 200 m, is apparent in the XBT data. Just upstream of the sill, (at ~ 6W), interfacial waves appear in the image. Since the flow is undoubtedly controlled at the sill crest, these may be transcritical waves, probably similar to those described by FARMER and SMITH (1980, Figure 13).

An expanded version of the current measurements during spring tides is shown in Figure 7.5, for which, during the inflowing tide, the entire water column moves east. The inflow occurs for a shorter period at greater depths than for the Atlantic water. Triangles along the time axis correspond to runs across the sill discussed earlier (Figure 7.4a-h). The overlay shows the way in which Atlantic water penetrates to different depths.

Finally, the full record from the Camarinal Sill mooring is shown in Figure 7.6. This figure serves to illustrate the way in which the various different flow regimes occur at different stages of the spring-neap cycle. The deepest instrument (255 m) tracks the movement of Mediterranean water across the sill; the salinity record at this depth shows that the Atlantic water penetrates to this depth only briefly during strong tidal inflows. An important result of this record is that it demonstrates the way in which Mediterranean water reverses during the spring inflows, but not during the neap inflow. Some care is required in the interpretation of shallower instruments because of the large vertical excursions of the mooring, but it is also clear that at this neap tidal period there are times when the shallowest instrument shows inflow throughout the tidal cycle.

## 8. THE CONTRACTION: TARIFA NARROWS

It is a striking feature of our acoustic images and XBT runs along the Strait that through the narrow section the interfaces characterizing the stratification slope up towards the east. This asymmetry of the interface with respect to the channel width is a clue to the hydraulic status of the flow in this part of the strait. Although the channel width is greater both to the east and west of Tarifa, the interface monotonically slopes up towards the east throughout this section (c.f. Figure 4.1). As discussed in Chapter 3, an asymmetric interface running through the contraction is consistent with the presence of an internal hydraulic control. In the inviscid case this control will be located at the narrowest section; frictional effects will shift the control slightly to the east (see, for example, CHOW, 1959, BORMANS et al., 1986). The hydraulic transition from subcritical to supercritical can easily be seen in a series of transects at different points along the strait, each obtained at approximately the same tidal phase.

The strait becomes narrower to the east of Camarinal Sill. In this relatively deep (~600 m) section the surface flow accelerates towards the east, but the composite Froude number is less than one. The subcritical flow in this portion of the strait provides the hydraulic connection between the two controls at Camarinal Sill and Tarifa Narrows. Since the flow is subcritical, adjustments in interfacial depth can propagate in either direction. Figure 8.1a is a transect at 3W. The interface depth lies between 90 and 180 m, and the surface layer flows east at 0.8 to 1.4 m $s^{-1}$, yielding a subcritical surface Froude number of $F_1^2 = 0.3$ to 0.8.

The next section, shown in 8.1b, is across 5E (the Cires transect), and lies just to the west of the narrowest part of the strait. By this point, the Atlantic flow is beginning to respond to rotation effects and the interface slopes noticeably down to the south. At the center of the channel the interface depth lies between 50 and 70 m, and the surface layer speed is 0.8 m $s^{-1}$ to 1.4 m $s^{-1}$, yielding a surface Froude number range of 0.5 to 1.6. Evidently this flow is close to critical.

Figure 8.1c illustrates the hydraulic conditions at the exit. The Atlantic water here moves in a fast (1.0–1.6 m $s^{-1}$), shallow (30–60 m at mid-channel) stream, with significant inclination. A surface Froude number based on the mid-channel properties ranges from 1 to 3: the flow is definitely supercritical through this transect. The surface layer thickness was also measured at other tidal phases, and at times was found to be significantly thinner. For example, Figure 8.2 shows the transect at high tide; the corresponding Froude number in this case is even higher (>2).

Further insight on the nature of hydraulic conditions in the eastern part of the strait, can be gained from analysis of the current meter mooring at station 9E (Figure 8.3). The shallower instrument (70 m nominal depth) is nearly always beneath the pycnocline, as indicated by the corresponding salinity measurements. However, the current is primarily directed towards the east. These observations illustrate the effects of momentum transfer between the thin, rapidly moving Atlantic surface flow and the deeper Mediterranean water. In effect, the supercritical surface layer is coupled to the deeper layer down to a depth of 100 – 150 m. This coupling is further discussed in Chapter 13.

There are substantial temporal variations in the flow speed and depth dependent density structure as a function of tidal phase, as predicted by theory. These may be seen from two types of time series. A rapid sequence of transects was obtained over a period of 5 hours at station 5E in order to verify that time series measurements in the middle of the channel are representative of the temporal variability. These observations (Figure 8.4a-f) show that the transverse tilt of the isopycnals and isotachs remains relatively steady for the limited period of our observations; there are no obvious signs of transverse oscillations, although there is aliasing of the XBT data when the undular bore travels through. It is interesting to note that there is little evidence of transverse oscillations in the data of LACOMBE and RICHEZ (1984) at this location (their Figure 31), in contrast to the Gibraltar section (their Figure 33). Numerous other transects, not illustrated here, show little evidence of transverse oscillations and support the usefulness of hydraulic interpretations based on mid-channel observations alone at this location.

A sixteen hour time series at station 3E (Figure 8.5) provides a detailed description of the velocity and density field, including the passage of two sets of internal bores. As each bore passes, the interface deepens from 25 m to 75 m. This bore is the far-field manifestation of flooding of the control at Camarinal Sill, and will be discussed further in Chapters 12 and 14. The Doppler profiles could not be bottom tracked here, and we had no deep current meter in the vicinity. However, the deep pycnocline and weak shear ensure that the flow is subcritical at this location throughout the tide. The Doppler profiles indicate that the sheared portion of the profile is generally coincident with the pycnocline.

At station 7E (Figure 8.6), just east of the narrowest part of the strait, the interface is generally shallower than at station 3E (Figure 8.5), and the amplitude of the internal bores is noticeably less, although the internal tidal amplitude for both of these time series is similar. On

the basis of consistency in the internal response detected at the Tarifa Narrows mooring (see Figure 8.3), we suspect that the differences between time series at 7E and 3E are a consequence of variation along the channel rather than temporal variability. The Froude number in this portion of the Strait is dominated by the surface layer. Since the channel is deep (~800 m), Doppler velocity profiles could not be referenced to the sea floor with the instrument fitted to RV OCEANUS. This precludes meaningful calculations, based solely on the Doppler profiles, of Froude numbers in this part of the Strait. An independent reference measurement is available, however, from the current meter mooring at Station 9E, two miles to the east. The deeper of the two current meters was invariably in the unsheared portion of the water column beneath the pycnocline (the instrument depth and observed velocity is recorded in Figure 8.6), and therefore yielded a time series that allows correction of the Doppler profiles and a useful estimate of the Froude number; we have plotted the corrected Froude number values directly on the figure.

It should be understood that although the concept of internal hydraulic control is precise, the calculation of Froude numbers from real density and velocity profiles necessarily includes an element of approximation. Strictly speaking, criticality can be defined for a continuously stratified and sheared flow, but such a definition would be too complex for application in the present case. Our operational definition is presented in Chapter 3.

At the start of the time series the flow is supercritical. Following Low Water between 2000 h and 2100 h, the Froude number drops precipitously, and then climbs steadily back to critical conditions over the course of the next 4 hours; thereafter it becomes supercritical, before dropping again at the following Low Water.

By station 13E (Figure 8.7) the surface layer is thinner and the surface layer velocity greater. The flow here is continuously supercritical. The Froude number reaches its highest values during periods when the isopycnals spread and deepen (for example 1800–2100 h). While the flow at 13E is discussed in greater detail in Chapter 13, we emphasize here the key observation that it is controlled upstream of this part of the Strait. A second time series at the same location during spring tides yielded essentially the same results.

The hydraulic conditions discussed in detail in the preceding chapters are graphically summarized in the along-strait run (Figure 8.8). The acoustic image and temperature structure clearly illustrate the way in which the interface gets progressively shallower between the control at Camarinal Sill and the control in Tarifa Narrows.

## 9. THE DENSE WATER RESERVOIR: ALBORAN SEA

East of the Gibraltar-Ceuta section, the Atlantic water runs into the Alboran Sea as a shallow surface jet. The surface layer separates from the north shore of the strait near the western shore of the Bay of Gibraltar and from the south shore of Ceuta. Once separated, the northern boundary of the jet is visible as a surface slick, which also appears as a small but identifiable feature in the acoustic images; its position varies somewhat with the tide, but generally runs east-west. North of this boundary lies relatively unmixed Mediterranean water. The thickness of the surface layer increases towards the south, consistent with its behaviour between Gibraltar and Ceuta (c.f. Figure 8.2).

Figure 9.1 includes an acoustic image and related data that illustrate the overall distribution of density and velocity along the section across the jet, together with a southern boundary adjoining the African coast. The center of the jet is an extension of the line of the flow seen in Figure 8.1c. The acoustic image in Figure 9.1 provides a graphic indication of the presence of the jet, with its inclined interface. Traces of internal waves are also visible in the acoustic image near the edge of the jet; these spread almost radially out of the Strait towards the east as our section cut south across them. They are consistent with other observations obtained at the same tidal phase and shown in the shuttle photograph of sun glitter (cover photo) and further discussed by FARMER and ARMI (1986).

South of the jet lies a relatively thick (100 m) layer of almost stationary Atlantic water. Neglecting the contribution of possible weak flows at depth, calculations of the surface layer Froude number in the jet, based on our operational definition, cover the range 0.5 to 0.8,. We saw no evidence of a sudden transition from supercritical to subcritical flow, nor should we expect one; the jet spreads and decays under the influence of friction.

The density and velocity structure of the Atlantic water jet that flows into the Alboran Sea is sketched in the cartoon (Figure 11.2), which is based on Figures 8.1b, 8.1c and 9.1. This figure emphasizes the relatively confined structure of the flow and the close relationship that exists between the velocity and density fields. The separation of the Atlantic water from the north shore of the Strait is discussed in Chapter 11.

It is interesting to contrast the very energetic transition from supercritical to subcritical flow, via an internal hydraulic jump, that occurs downstream of Camarinal Sill, with the quite gentle transition from supercritical to subcritical in the eastern part of the Strait. The reason for this contrast is related to the response of the flow to changes in depth and in breadth.

This response is described by the differential solution for the interface. It is most easily seen for a single layer (ARMI, 1986, eqn. A7a, b),

$$\frac{1}{y}\frac{\partial y}{\partial x} = \left[\frac{1}{1-F^2}\right]\frac{1}{b}\frac{db}{dx} - \left[\frac{1}{1-F^2}\right]\frac{1}{y}\frac{dh}{dx} \qquad (5)$$

Similar equations for the two-layer case are also given in ARMI (1986). Over Camarinal Sill the relative change in bottom height, normalized by the layer depth, $(1/y)\,(dh/dx)$, is about $10^{-3}\ m^{-1}$. In the eastern part of the Strait the relative change in breadth $(1/b)\,(db/dx)$ is much less, of order $5 \times 10^{-5}\ m^{-1}$. Moreover, as discussed in Chapter 11, the fact that the flow separates effectively isolates the outflowing jet from changes in breadth, so that acceleration of the surface layer is much weaker, and the transition back to subcritical flow is a quite gentle process.

An additional factor influencing this transition is friction (c.f. HENDERSON, 1966). Downstream of Camarinal Sill friction is not dominant, because the term $(1/y)\,(dh/dx)$ is much greater than any realistic frictional term, whereas in the eastern strait the term $(1/b)\,(db/dx)$ is of the same order, although somewhat larger than the frictional term $C_d/h$ ($C_d = 10^{-3}$, $h = 50$–$100$ m). The friction between layers within the contraction has the effect of displacing the control downstream to the point at which $(1/b)\,(db/dx)$ and the frictional term are in balance (Pratt, 1986). Downstream of the control, the effect of friction will be to

diminish the importance of the change in channel width; if, as happens in the Strait of Gibraltar, separation occurs, then friction will be the dominant term in the energy balance. The effect of friction within the supercritical flow will always be to return the flow to the critical condition.

## 10. SEASONAL MEASUREMENTS

Our primary cruise in the Strait of Gibraltar was aboard RV OCEANUS in April 1986; an important question is therefore the degree to which the hydraulic conditions we observed are representative of other times of year. Some limited ship time was available on the RV LYNCH cruise during October 1985, and this provided some data on the hydrographic and hydraulic conditions at that time. A series of runs was made down portions of the Strait, and acoustic images, XBT profiles and a few XCPs (expendable current profiles) were obtained. Two of these runs are discussed here and their positions and timing are shown in Figure 2.2.

Figures 10.1 and 10.2 show the results from two runs throughout the length of the Strait. Several other runs were made but are not shown here. The acoustic images and XBT data show the general inclination of the interface along the Strait, as well as other features such as the interaction of the flow with Camarinal Sill. The sill interactions, both at Camarinal and at Spartel, observed in October, are essentially identical to those observed the following April, including the generation and propagation of internal bores (see also WESSON and GREGG, 1988a). The temperature reference of 13.5°C, indicated by a solid circle on each profile, is substantially deeper than the pycnocline at this time of year. We have also added a '+' symbol at 15°C on each profile. At this time of year the interface spans the temperature range between 13.5° C and 15° C. (see LACOMBE and RICHEZ, 1982, Figure 8). The two runs shown here are also of interest because they include current profile measurements. In Figure 10.1, a current profile over Spartel Sill shows the presence of a deep outflow, consistent with that measured by Doppler and moored current meters in April. The Froude number at this location is approximately 1.8. High velocities in the deep layer were also observed by BØYUM in June (BØYUM, 1967).

Moving east, the XCP profile in Tangier Basin shows a modest flow at mid-depth (150-250 m). This flow is subcritical, but there is clear evidence in the acoustic image of hydraulic interaction with the nearby bottom irregularity. Over Camarinal Sill the flow is almost uniform. The XCP does not yield an absolute measure of velocity, but the tidal phase (approaching HW) is consistent with a strong westward flow; the acoustic image confirms this expectation. The easternmost XCP was obtained at approximately Station 12E (Gibraltar-Ceuta). The Froude number here, assuming no net flow at depth and using the XBT profiles as a guide to the interface depth, is approximately 0.7. This would be consistent with control at Tarifa Narrows with an adjustment further east, although hydraulic control at Tarifa Narrows is not specifically demonstrated by these observations.

Figure 10.2 is similar, although obtained during a falling tide. The XCPs at Spartel and in Tangier Basin have the same interpretation as before. The flow over Camarinal Sill is to the east, and the XCP and accompanying XBTs just east of the sill show the thick eastward-moving surface layer with finestructure typical of mixing.

Further east the surface layer becomes thinner. In Tarifa Narrows the interface has risen to approximately 75 m. Using a tidally adjusted estimate of deep water flow calculated from our deepest instrument in the narrows during April, we find a negligible correction to the relative velocity profile, which then yields a Froude number of 0.8, similar to that observed at this tidal phase (HW + 4 h) at this location six months later (Figure 8.6).

WESSON and GREGG (1988a) report a significantly deeper interface in the eastern part of the Strait during October 1985, compared to conditions in May 1986. They have extensive data in the Gibraltar-Cueta section. However, this location is considerably further east than the expected location of the control. It is not clear whether the reservoir conditions represented by this deeper interface have flooded the control at Tarifa Narrows. Moreover, as reported by WESSON and GREGG (1988b), no comparison can be made in the Tarifa Narrows since they obtained virtually no profiles in October at this location.

In ARMI and FARMER (1985), we drew attention to the existence of critical conditions in May ($F_1^2$ ranging from 0.7 to 2.1) in the Gibraltar- Ceuta section and in June in the Cires section ($F_1^2$ up to 4). A further indirect indication of controlled flow in the eastern part of the Strait is derived from a photograph from space which is shown here on the cover, and discussed in detail in FARMER and ARMI (1986). Nevertheless, taken together, these disparate observations, spanning four different months, are still insufficient to demonstrate the continuous existence of a control in the narrows.

There is a need for extended monitoring to resolve questions of seasonal variation in the Strait. The complicated time dependence in the Strait serves to emphasize the difficulty of interpreting tidally averaged data acquired over Camarinal Sill, or indeed in any of the more energetic portions of the flow. The hydraulic response to tidal effects is inherently nonlinear. Moreover, measurements in an active area such as Camarinal Sill are too complicated to explain without simultaneous runs and sections of the type used in this study. Such intensive measurements are scarcely possible over a long period.

These considerations show that if seasonal and interannual changes in the exchange are of interest, they should not be monitored in an active area of the Strait, but rather at its western end. The Mediterranean outflow over Spartel West is steady with only minor tidal variations (see Figure 5.2). An array of four or five current meter moorings across the outflow (see Figure 5.1) would provide a reasonably accurate measurement of the discharge and interface position. An integral measurement technique, in particular the analysis of motionally induced voltages across submarine cables, might be useful for long term measurement, provided that it could be properly calibrated.

The maximal exchange solution has been demonstrated for the period of our observations in April. There is as yet insufficient evidence to demonstrate conclusively the existence or otherwise of a second control at the eastern end of the Strait in October 1985. In the companion papers describing hydraulic exchange theory (ARMI and FARMER, 1986, and FARMER and ARMI, 1986) both maximal and submaximal exchange flows are discussed. BORMANS, GARRETT and THOMPSON (1986) have discussed the application of the submaximal portion of this theory to the Strait using extensive historical data, and consider that the exchange may be submaximal at certain times. More recently, GARRETT, THOMPSON and AKERLEY (1989) have carried out a very careful analysis of 13 months of tidal data obtained during the MEDALPEX study, Sept. 1981 through Sept. 1982. These observations are unique among the

historical tide gauge data in that they were collected simultaneously on both sides and along the axis of the Strait (Gibraltar, Ceuta and Tarifa). By comparing fluctuations in sea surface slopes along the strait, with cross-strait slopes, they found the results consistent with a maximal exchange flow throughout the observation period.

In view of the interest and importance of the hydraulic conditions in determining seasonal adjustments in the exchange, it is clearly desirable to obtain suitable measurements near the expected locations of the eastern control. In considering various options for monitoring hydraulic conditions in the eastern strait, it appears that there is no straightforward alternative to the detailed measurement of velocity and density. Thus, recording Doppler data obtained from moorings, though certainly interesting, is insufficient to define the Froude number without an accompanying thermistor/conductivity chain to identify the location of the pycnocline. Similarly, CTD time series without simultaneous velocity measurements are of limited use.

Robust surface moorings, located on the traffic separation line, could be instrumented in such a way as to monitor the internal hydraulic conditions in the eastern part of the Strait. In particular, such a measurement program should focus on whether or not the eastern control, which occurs in the narrows, is flooded by deeper interface conditions in the eastern part of the Strait, and hence, whether or not the exchange is maximal or submaximal at the different times of the year. Such moorings would have to include salinity sensors at close intervals (~10 m) through the expected range of the pycnocline, together with velocity data (for example recording current meters or a recording Doppler profiler). Data from such moorings over an extended period could provide a basis for determining whether or not the maximal exchange conditions that we observed in April persist throughout the year. Additionally, there are a number of techniques which could be used to infer the existence of a control in the eastern part of the strait. These include accurate tidal measurements for comparison of fluctuations in along strait and cross-strait slopes, observations of surface temperature and salinity from the Algeciras-Ceuta ferry for identification of separation of the Atlantic inflow, radar measurements of the surface signature of the separated water and finally acoustic propagation measurements to probe the internal structure and flow in the strait.

## 11. TRANSVERSE ISOPYCNAL SLOPES AND SURFACE SLICKS

The influence of rotation on stratified shear flow in a channel is a well established fact, resulting in isopycnal slopes which are directly related to the flow speeds and density gradients. The determining scale in these rotating flows is the internal Rossby radius of deformation.

The isopycnal slopes are clearly observed in Figure 5.1 for the Mediterranean outflow at Spartel West. Transport estimates are commonly made for flows of this type under the assumption of geostrophic balance. However, there are serious difficulties in this approach when the data are only available as simple sections across the channel. The interface slopes down to the west as the Mediterranean water runs down towards the Atlantic. The slope induced by rotation is normal to this flow. Rough estimates based on our observations show that these two interfacial slopes, along and across the direction of flow, are comparable. Thus, an estimate of transport based on a transect across the flow will be subject to significant error unless great care is taken to ensure that the transect is truly normal to the flow. Satisfaction of this requirement is

probably unrealistic for the complex topography of the Strait of Gibraltar. For example, if we apply a geostrophic balance to the observed slope in Figure 5.1, which is certainly not truly normal to the isobaths (see Figure 2.1), we arrive at an estimate of approximately 2 Sverdrups ($10^6\,m^3s^{-1}$). This is higher than traditional estimates (c.f. LACOMBE and RICHEZ, 1982), but we can expect a bias toward larger values given the relative angle of our transect. It might be possible to make approximate transport estimates based on the acoustic Doppler profiled sections, although in our case these profiles unfortunately do not extend to the sea-floor, owing to range limitations and sidelobe interference (see Chapter 2).

We note here that in this section of the Strait (Figure 5.1) the Atlantic water has essentially no transverse shear; this observation is relevant to our subsequent discussion of the advection of vorticity through the Strait. The Doppler profiles do not extend throughout the Mediterranean outflow, so that our isotach distribution is inadequate at this location for measuring transverse variability in the velocity structure near the bottom. However, transverse variability of the Atlantic layer will be examined in the eastern part of the Strait. In Tangier Basin (Figure 6.1), the isopycnal slopes are smaller than at Spartel West, consistent with the reduced velocity in this subcritical section.

Camarinal Sill is a very complex environment that is not ideally suited to either cross-section calculations or synoptic measurements. Significant isopycnal slopes across this sill were detected for only two out of a total of 14 hours of continuous measurement reported by LACOMBE and RICHEZ (1984).

In the subcritical flow just east of Camarinal Sill (Figure 8.1a) the interface is deeper on the south side of the Strait than on the north. The inclination is not uniform, but is concentrated near the two boundaries. As the Atlantic layer accelerates through the Narrows, the interface becomes progressively more inclined. In Figure 8.1b, at Cires, the inclination is relatively uniform, but the surface layer velocity distribution has a significant transverse gradient. Figure 8.1b shows a noticeable transverse shear in the surface layer flow. This shear is of order $-f$, which is consistent with conservation of potential vorticity advected through the Strait with a decreasing surface layer thickness (compare Figures 8.1a and 8.1b).

By the time the Atlantic water reaches the Gibraltar-Ceuta section, the inclination of the interface is well developed. The surface layer velocity field shows no signs of transverse gradients (Figure 8.1c); this is presumably a consequence of cross-channel mixing within the homogeneous surface layer. The interface on the north shore is shallow (~35 m) but at this time, on a rising tide, does not intersect the surface.

In contrast, the Gibraltar-Ceuta section obtained at high water (Figure 8.2), shows the interface reaching the surface close to Gibraltar. This phenomenon is associated with a surface slick running parallel with the axis of the Strait and out into the Alboran Sea, which appears in Figure 9.1 and is discussed in Chapter 9. This slick was frequently observed from the ship.

Moving surface patterns appear on radar images obtained from Gibraltar. Figure 11.1 is an example of one such radar image (provided courtesy of Gary Watson, University of Southampton) obtained ~ 9 h 40 min after High Water. Numerous other radar images have been analyzed by Watson, who has shown that these slicks generally occur during spring tides at about the same tidal phase and move towards the north shore. The image in Figure 11.1 is inserted into a chart drawn to scale, which also includes the location of the slick observed on 13 April at the same tidal phase, and shown in Figure 9.1. A continuation of the slick in the radar

image passes near the observed location of the slick seen on 13 April, although it should be stated that we have no direct confirmation of the oceanographic structure of the radar slicks.

Figure 11.2 is a cartoon showing a perspective view of the surface jet with isotachs taken from Figures 8.1b, c and Figure 9.1, collected on different days, and also showing the presumed location of the surface slick. The photograph taken from the shuttle (see cover photo) clearly shows an area of low reflectance just south of Gibraltar. This may also be a manifestation of the interface inclination, resulting in a separation of the inflowing Atlantic water.

Our observations indicate that the northern edge of the jet running into the Alboran Sea is relatively straight, whereas the southern boundary tends to expand somewhat to the south, consistent with the expected influence of rotation. Our measurements show no obvious way in which this jet could be influenced by a reservoir condition in the Alboran Sea. We emphasize that flooding of the control at Tarifa, a necessary precondition for submaximal exchange, requires a subcritical connection between the flow just east of Camarinal Sill and the stratified flow in the Alboran Sea.

Integration of the surface layer flow in Figures 8.2 and 9.1 yields estimates of an eastward transport of approximately $10^6$ $m^3$ $s^{-1}$, consistent with previous estimates (LACOMBE and RICHEZ, 1982).

## 12. INTERNAL UNDULAR BORES

A prominent oceanographic feature of the Strait of Gibraltar is the presence of internal undular bores, which have a surface manifestation easily observed from ships, aircraft and from space (see cover photo). These bores have been the subject of numerous theoretical and some experimental studies, references to which may be found, for example, in ARMI and FARMER (1985), FARMER and ARMI (1986), LACOMBE and RICHEZ (1982), WESSON and GREGG (1988a). Our purpose here is to provide evidence of their generation mechanism and of their propagation characteristics as they travel down the Strait.

The bores occur as a direct consequence of the rapidly changing hydraulic conditions over Camarinal Sill. The generation of internal bores by tidal forcing over topographic features has been widely discussed in the literature (see for example, FARMER and FREELAND, 1983). In the Strait of Gibraltar a large stationary internal bore forms downstream of Camarinal Sill during tidal outflow (see for example, Figure 2.5). The bore in this figure extends over a distance of 3 km, which for a flow speed of ~1 m $s^{-1}$ implies a time scale of an hour for adjustment of the bore to changes in the tidal current. However, the change in tidal current over this period is sufficiently rapid that it prevents a smooth adjustment within the bore. While the details of the release of this energy from the sill may change between spring and neap tides, the process that we have observed includes the successive degeneration of the stationary bore into a sequence of large amplitude internal waves which climb eastward over the sill crest and propagate down the Strait. These large internal disturbances may themselves develop into multiple waves, and the evolution of the whole series of interfacial distortions into an internal undular bore will follow the pattern for nonlinear dispersive features that has been so widely discussed elsewhere. The distinguishing feature of the bore in the Strait of Gibraltar is that it

travels through a rapidly changing field of stratification and shear, as the surface layer becomes thinner and accelerates towards the east. Superimposed on this changing structure is the time varying tidal current, including a flow reversal during spring tides.

The large stationary bore, one tidal period prior to that shown in Figure 2.5, was tracked as it collapsed into smaller waves and travelled east. The first sign of this process is shown in Figure 12.1a, one hour before High Water. At this time the lower-layer Froude number over the sill crest is about 0.2. A large amplitude (~100 m) internal wave is just about to pass over the sill crest. Its signature on the 75 m Camarinal Sill current meter (Figure 12.2) is a sharp decrease in both salinity and temperature. The waves are of order 1 km long and have a period of ~1000 s. This feature is identified by the first vertical line drawn on the time series one hour before High Water. This characteristic signature can be used to track the release of the first part of the bore at other times. The internal wave is not only of large amplitude, but the interfacial slopes are steep (of order 1:4). Waves of this aspect ratio may not be stable; in general, our observations show maximum isopycnal slopes of order 1:8 further down the Strait.

The flow has reversed in the next image (Figure 12:1b), which shows at least two internal waves of small amplitude and slope travelling across the sill.

By three hours after High Water (Figure 12.1c) the flow continues strongly toward the east, except for a temporary change in direction at the 210 m current meter, due to a perturbation caused by the lee wave. This lee wave structure is the internal response to a strong eastward flow over the sill, which in due course is released to form an internal wave train propagating towards the west.

The time series current-salinity-temperature observations during the above period, shown in Figure 12.2, illustrate fluctuating salinity at the shallower instrument during the subcritical portion of the tidal cycle. This signal penetrates to the deeper instruments only during the strongest tides.

Time series observations of the internal bore as it travels east, show that it always arrives at about the same time, relative to High Water, for any particular location. Figure 12.3 (a and b) show two successive passages of the waves through Station 3E. The full time series from which these data were extracted is shown in Figure 8.5. At this station, the bore is characterized by two or three large internal waves followed by a less orderly interfacial disturbance, with strong indication of finestructure in the CTD profiles. Profiles in this and subsequent figures which clearly indicate mixing are annotated with an 'M' in the depth range of interest. The bores shown in this figure are separated by 11.5 hours. The tidal phase at which a bore is released at the sill is not always the same, but varies by as much as one hour, due to the diurnal inequality in the tide. This variation in release time results in a corresponding variation in arrival time at locations along the Strait, as shown in this example.

In Figures 12.4 and 12.5, the bore is shown at the eastern end of the Strait (Station 13E), at neap and spring tides, respectively. The wave amplitude is larger during the spring tide.

The bores shown in Figures 12.3 to 12.5 are all of the first internal mode. We have also observed mode 2 disturbances. An example is shown in Figure 12.6; the same phenomenon was observed on three other occasions. The disturbance occurs as a spreading of the isopycnals accompanied by mixing. (In this image, the echo from the CTD can be seen as an arc following passage of the bore. The thinning of the backscatter cloud in the vicinity of the profiler is

consistent with evasive behaviour of biota, which has been shown by FARMER, CRAWFORD and OSBORN (1987), to result in identifiable contributions to microstructure records.)

The release and propagation of the bore is summarized in Figure 12.7, along with the maximum tidal height at Tarifa. The time intervals in this figure are 12.5 hours apart and coincide with time of high tide. Above this sequence is shown the time of bore release at Camarinal Sill, determined as discussed in reference to Figures 7.3, 12.1 and time series measurements at 7E (not shown), and also the time of its arrival at the Tarifa Narrows mooring determined from the data shown in Figure 8.3. During spring tides the bore is consistently released on every tide, but during this particular neap tide we did not observe any bores, although other observers have detected bores during neap tides (LACOMBE and RICHEZ, 1982, Figure 21). During the transition period the bore is released on alternate tides.

The propagation of the bore is presented in Figure 12.8. Here we have used observations of the bore's passage through various stations to construct an x-t diagram of its journey along the Strait. Data are used for both mode 1 and mode 2 bores, each referenced to the time of observed release at Camarinal Sill. At the top of Figure 12.8 the approximate interface depth is sketched, along with representative values of the surface layer velocity and the inferred linear wave speed calculated for a mode 1 wave in the absence of shear. The sum of these two values is given as a 'theoretical speed of bore' and is consistent with the speed deduced from the observations.

The eastward travelling bores discussed above have a counterpart in a much smaller amplitude feature that travels to the west. This is the weak undular bore released from the sill close to Low Water at the end of the inflowing (eastward) tide and shown in Figure 12.1c prior to release. It is unlikely to have such a strong surface manifestation as the eastward travelling bore, not only because it is weaker, but also because of the greater surface layer depth. Figure 12.9 shows an example of this westward travelling bore in Tangier Basin.

## 13. MIXING, FRICTION AND ASSOCIATED ENERGETICS

The topographically influenced flow in the Strait of Gibraltar, and the consequent presence of internal hydraulic controls, are associated with strong shears that can lead to turbulence and mixing. As one layer is accelerated relative to another, the Richardson number at the interface can drop to low values, allowing instabilities to develop (ARMI, 1986, Figure 6). These, in turn, produce turbulent mixing between the layers and the consequent modification of interfacial shear and density structure, subsequently permitting the resumption of a stable flow. Mixing induced in this way is expected to be especially prevalent in the supercritical region downstream of these controls within the Strait.

While mixing certainly takes place just outside the Strait, for example in the supercritical Mediterranean outflow west of Spartel Sill, the features of primary interest here are the internal hydraulic jump downstream of Camarinal Sill, the subcritical flow east of the sill, the travelling internal bore and the supercritical jet east of Tarifa Narrows.

Evidence of mixing can be inferred from finestructure, such as steps and inversions in the density and XBT profiles, and from shear flow instabilities visualized in the acoustic images. For example, in Figure 2.5a finestructure appears in the XBT profiles within the hydraulic jump,

although there is little evidence of finestructure through the control point and in the early portion of the supercritical flow just downstream of the sill crest.

We can estimate the energy loss near Camarinal Sill from the observed change in interface height, Δh, between the subcritical flow upstream and downstream of the sill. To first order we neglect the kinetic energy, since the Froude numbers in the deep reservoirs some distance on either side of the control region are small. Specifically, we consider the change in interface height between stations 4W and 11W. This avoids the complication of calculating the energy loss across the internal hydraulic jump, which would require accurate breadth averaged velocity and density profiles at close intervals in a very energetic portion of the flow. Then, the potential energy loss, ΔE, is $(\Delta\rho/\rho)g\ \Delta h$ , and the rate of energy loss is ΔE • U. This energy loss occurs over a limited distance, mainly through the internal hydraulic jump, including the strongly sheared and entraining flow just upstream of the jump. Denoting this distance L, the rate at which energy is lost per unit mass is then E • U/L. During the quasi-steady conditions that predominate through much of the tidal cycle, this energy loss must be largely dissipated. A small fraction is transformed into potential energy through mixing, and at the end of the ebb tide energy is also radiated away in the form of the travelling bore.

We estimate the energy dissipation downstream of the sill for a strong outflow. Figure 2.5a,b shows that $\Delta h$ is approximately 70 m between stations 5W (upstream of the sill ) and 11W (downstream of the jump), and U is approximately 1 m $s^{-1}$ in the vicinity of the jump. For $\Delta\rho/\rho$ $2 \times 10^{-3}$ and a jump length of ~3 km, E • U/L = $0.5 \times 10^{-3}$ $Wkg^{-1}$. Dissipation estimates based on micro-structure profiles in the vicinity of the jump are consistent with this calculation (see Figure 5a, b in WESSON and GREGG, 1988a).

A detailed view of instabilities just downstream of the sill control is shown in Figure 13.1, which is an expansion of a section of Figure 7.2 together with its acoustic image. This time series corresponds to a period of strong outflow over the sill: the flow is highly sheared and the interface is rising. The record begins with a quite sharp interface and few signs of turbulence in the density profiles. After 1120 *h* finestructure appears in the density profiles and the acoustic image shows signs of instability. The presence of the instabilities is closely related to the Froude number, which exceeds one between 1130 *h* and 1300 *h* . They are initially quite indistinct, but they become clearer as the sheared interface gets shallower and starts to incorporate biological scatterers in the upper 75 m. The instabilities are most clearly identified at the base of the relatively well-mixed surface layer. They do not penetrate into the more strongly stratified portion of the flow. In this sense they more closely resemble the asymmetrical shear instabilities described by HOLMBOE (1962), and reproduced in laboratory experiments by KOOP and BROWAND (1979), than the symmetrical Kelvin-Helmholtz type. Since the pioneering flow visualization experiments of BROWN and ROSHKO (1974), similar coherent structures have come to be recognized as an almost ubiquitous feature of high Reynolds number free shear layers.

In Figure 13.1b, Richardson number profiles are shown overlaying the same image. These show relatively stable water in the lower layer, but marginal stability, or clearly unstable conditions, in the upper portion of the stratified region and at the base of the surface layer, in the vicinity of the visible instabilities.

The organized structures appearing in Figure 13.1 do not indicate an instability of the interface to long wave disturbances. FARMER and ARMI (1986) showed that the interface over

a sill crest for an exchange flow is always stable for moderate barotropic forcing. The flow is unstable for strongly forced flow from the less dense reservoir, in which case the surface layer separates from the sill, and instabilities in such cases have been observed (see for example, Figure 8 in FARMER and SMITH 1980). However, this condition is prevented from occurring in Gibraltar Strait by flooding of the control from Tangier Basin and the formation of a reverse flow with an interface height above sill depth (Figure 7.4c, d, e). The evolving structures in Figure 13.1 are instead the result of local instability of the weakly stratified shear flow at the base of the surface layer.

In the subcritical flow connecting the two controls at Camarinal Sill and Tarifa Narrows the dissipation is very much less than in an active area such as the hydraulic jump. Friction between the layers in the subcritical region has the effect of slightly decreasing the acceleration of the surface layer and increasing the slope of the interface. We can calculate the size of this effect from dissipation measurements in this part of the Strait given by WESSON and GREGG (1988a). For this part of the Strait, they found dissipation values, $\varepsilon$, of $10^{-7}$ to $5 \times 10^{-6}$ Wkg$^{-1}$ (J. Wesson, personal communication). For a length L $\simeq$ 20 km between Camarinal Sill and Tarifa Narrows and a surface layer flow speed, U, of 0.5 m s$^{-1}$, $\Delta h = \varepsilon / g' U$ = 0.2 to 10 m. This small frictional contribution to the interfacial slope may be compared with the observed change in interface height between Camarinal Sill and Tarifa Narrows of 50 –100 m (c.f. Figure 4.1). However, it should be emphasized that this calculation does not include sidewall friction, the effects of which are not easily estimated from available data.

Energy is also dissipated in the travelling bore. Some density profiles obtained within the bore (c.f. Figures 12.3a, b, and 12.4; note especially profiles marked 'M') show finestructure indicative of turbulence and mixing. The acoustic images provide further and more direct evidence of turbulence. Despite these examples of turbulence, the travelling bore is probably of minor significance as a mechanism for energy dissipation within the Strait. WESSON and GREGG (1988a, Fig. 7) show dissipation of order $2 \times 10^{-5}$ Wkg$^{-1}$ over a depth of ~100 m and lasting 2000 s. They state that dissipation rates have returned to background values [$10^{-6}$ Wkg$^{-1}$] after 2 hours. Since this dissipation occurs once every 12.5 *h* on stronger tides, the tidally averaged contribution is of order $10^{-6}$ Wkg$^{-1}$. Thus the tidally averaged contribution of dissipation from the bore will be comparable to the background level of dissipation in the absence of the bore which, on the basis of these observations, we have already shown to be small. The dissipation ($2 \times 10^{-5}$ Wkg$^{-1}$) of the undular bore can also be compared with the previously calculated dissipation of the hydraulic jump of $0.5 \times 10^{-3}$ Wkg$^{-1}$. This serves to emphasize the relatively minor role played by the internal bore, which is simply a transient manifestation of loss of control at Camarinal Sill. Its primary contribution is periodically to move the location of the eastern control in Tarifa Narrows, as discussed in Chapter 12.

Turbulence and mixing may also be expected in the supercritical jet in the eastern part of the Strait. Finestructure occurs in some of the CTD profiles and the flow is strongly sheared. The time series at 13E (Figure 8.7) shows a deepening of the sheared flow and of isopycnals greater than 27.0 during strong inflow. This condition follows passage of the bore through this location, but it is not a consequence of the bore. For example, the same effect occurs between 1800 *h* and 2200 *h* on 12 April when no bore was detected at Camarinal Sill (see Figure 12.7). Profiles of the Richardson number for this time series are shown in Figure 13.2. Smaller values (closer to

1/4) are persistent in the deepening sheared flow, both following passage of the bore (0900 *h* – 1100 *h* ), and also from 2000 *h* to 2200 *h* , providing additional evidence of turbulence.

Individual CTD density profiles for the latter period are shown on an expanded time scale in Figure 13.3. The profiles show clear evidence of unstable density structure which must be associated with overturns. It should be noted that the lowering rate of the CTD is about 1.3 m $s^{-1}$ which is comparable to the surface layer flow speed. Therefore the CTD descends at an angle of 45° or steeper with respect to the advected instabilities. The observed density instabilities are therefore real, and not an artifact of advection of horizontal gradients past a slowly descending instrument.

Turbulence serves to couple the layers and provides a frictional limit on the speed reached by the supercritical surface flow into the Mediterranean as the Strait expands. However, we consider that this effect is predominantly a consequence of the supercritical condition. In subcritical flow ($G^2 < 1$), the interfacial Richardson number adjusts such that it is significantly greater than 1/4, implying a stable flow with a relatively confined interface. When the flow moves from subcritical to supercritical, the bulk shear between the layers increases; in order for the flow to remain stable the thickness of the sheared zone must also increase. This transition will be a spatially distributed process, the location and extent of which will vary with the tide; it was not studied in great detail in our field program.

The adjustment from supercritical to subcritical flow will always be associated with an energy loss that can be represented by a large coefficient of friction. But the necessary inclusion of frictional effects in the supercritical zone does not invalidate the concept of the two controls and the inviscid hydraulic model between the controls, which governs the maximal exchange. The adjustment to subcritical flow at the eastern end of the Strait, necessarily associated with strong frictional coupling between the layers (c.f. WILKINSON and WOOD, 1971), was a component of FARMER and ARMI's (1986) theoretical model. These frictional effects in the adjustment region undoubtedly influence the circulation at the eastern end of the Strait, but since they are a result of supercritical flow they cannot directly affect the internal hydraulic constraints that control the exchange. The mixing that does occur represents the first step in the process of mixing between the Atlantic inflow and Mediterranean water. Ultimately of course, the mixing, as well as other water mass transformation processes such as evaporation and river discharge, must continue until the Atlantic water is finally transformed into Mediterranean water and is flushed out through the Strait.

The surface wind stress can also contribute to mixing and interfacial slope. This effect, however, is also minor. Consider for example, the extreme case of a wind speed of $W \simeq 20$ m $s^{-1}$. For a surface layer thickness $h \simeq 100$ m and typical drag coefficient $C_d \simeq 2 \times 10^{-3}$, the interface slope required to balance the wind is $C_d(\rho_a/\rho_w)W^2/g'h = 4 \times 10^{-4}$. This slope is very small compared to the observed slope and comparable to the calculated contribution due to interfacial friction discussed earlier. More typical wind speeds would be balanced by much smaller interface slopes, and in general the contribution to turbulent dissipation by the shear stress at the base of the mixed layer will far exceed that associated with wind stress. A similar estimate for frictional effects along the sea-floor shows that bottom stress is negligible. These calculations serve to demonstrate the validity of the inviscid assumption in the central part of the Strait bounded by the two controls, and thereby support a description of the exchange in terms of an inviscid internal hydraulic model.

# 14. CONCLUSION

A primary goal of our study was the identification of key features of the internal hydraulics that govern the exchange through the Strait of Gibraltar. As discussed in Chapter 3, maximal exchange is the important limiting solution. A definitive test for maximal exchange, subject to the various complications of time dependence, is the demonstration that an exchange control region exists, bounded at both ends by supercritical flow.

Our observations in April 1986 of flow speed and interface height at Spartel West (Figures 5.1 and 5.2) show that the Strait was always bound at its western end by a supercritical flow. Similarly, the time series measurements at the eastern end of the Strait (Figures 8.7 and 8.8) showed a consistently supercritical flow. The combination of these two supercritical flows, bounding a subcritical flow within the Strait, demonstrates that the exchange was maximal during the period of these observations. The October observations are less complete and, although indicating a generally deeper interface in the eastern part of the strait, do not include the temporal and spatial measurements of the density and velocity fields required to determine unambiguously the presence or otherwise of a control at Tarifa Narrows.

Between these bounding supercritical states lies a complicated, time dependent flow field. It is important to understand that although this time dependent behaviour will modify the exchange rate corresponding to the maximal solution, it need not violate the condition itself (see for example, ARMI and FARMER, 1987). In the theory of two-layer exchange flows over sills and through contractions, which guided our experimental design and data analysis, it was clearly recognized that the quasi-steady assumption was only approximate (FARMER and ARMI, 1986, page 75). The observations described in the foregoing chapters provide a detailed description of the time dependent behaviour at various locations along the Strait, which will now be integrated into an overall hydraulic analysis including all of the processes influencing the maximal exchange.

The essential elements of the time dependent response in the Strait are summarized in Figure 14.1a for spring tides. This diagram should be contrasted with the cartoon of the hypothetical quasi-steady response shown in Figure 3.2. The figure shows four synopses of our data set at different stages of the tide. These synopses are not quite equally spaced in time, but correspond to the data sets that most readily provide a comprehensive summary of conditions throughout the Strait. We identify the internal hydraulic processes for each synopsis; the detailed discussion of these processes at each location is given in the previous chapters.

The first synopsis shows conditions one hour before High Water. Over Spartel West the flow is controlled; the Mediterranean water flows out at a steady rate of $\sim 1.6$ m s$^{-1}$. Between Spartel West and Spartel the flow is subcritical, but it is also controlled at Spartel Sill and matched to the west with a hydraulic jump. In Tangier Basin the interface is rising at this time because of the strong westward flow over Camarinal Sill. A small interfacial disturbance travels westward along the Tangier Basin interface; it is the weak undular bore formed over Camarinal Sill near the previous Low Water when the deep water was flowing eastward (see Figure 12.9). Just west of Camarinal Sill there is a large hydraulic jump, matching the supercritical flow on the western flank of the sill with the subcritical flow in Tangier Basin. There is a strong westward flow throughout the water column at this time (1.4 m s$^{-1}$). East of Camarinal Sill the flow is

subcritical; the interface deepens slightly and remains deeper throughout the subcritical zone. In Tarifa Narrows the interface rises, the flow becomes critical and then supercritical. Still further east, the flow returns to subcritical in the Alboran Sea.

The second synopsis corresponds to conditions at High Water. As in the earlier case, the flow is controlled at Spartel West. However, the flow is subcritical over Spartel Sill and over Camarinal Sill. Thus, at this stage of the tide the western control is at Spartel West; there are no other sill controls in the Strait. This stage of the tide corresponds to the time at which the Tangier Basin reservoir is filled with Mediterranean water. The weak westward propagating bore identified in the previous synopsis has nearly reached Spartel Sill. East of Camarinal Sill, the large bore, formed during the relaxation of the westward flow over the sill, propagates east down the Strait towards Tarifa Narrows. The bore is travelling into subcritical flow, and leaves a subcritical flow in its wake. But further east, in Tarifa Narrows, the flow remains supercritical. At this time, then, the flow in the Strait has just two controls: one at Spartel West and one at Tarifa Narrows.

In the third synopsis, corresponding to one hour before Low Water, the control is recovered at Spartel Sill, and matched to the west with a hydraulic jump to subcritical flow between Spartel Sill and Spartel West. Tangier Basin has, by this point, drained of Mediterranean water, both to the east and to the west, and the interface is deep. Over Camarinal Sill there is a strong eastward flow of Atlantic water ($1.3\ m\ s^{-1}$) and a weak outflow in the deeper layer. This eastward flow is controlled at the sill, and a lee wave forms to the east. It is the relaxation of this flow that allows the lee wave to move back westward over the sill crest, forming the weak bore that travels across Tangier Basin. East of Camarinal Sill the interface slopes steeply upwards through the subcritical flow, towards the large bore, which by this time is moving into Tarifa Narrows. The interface just ahead of the bore is shallow (30 m) and the flow speed is relatively large ($0.7\ m\ s^{-1}$). The bore actually marks the transition between supercritical flow to the east and subcritical flow to the west; the control in Tarifa Narrows at this time is therefore a moving control.

Finally, the conditions at Low Water are shown. The flow is controlled at both Spartel West and Spartel Sill. In Tangier Basin the interface is rising, as Mediterranean water pours westward over Camarinal Sill. This flow is controlled at the sill crest and a large hydraulic jump forms just west of the sill, matching the subcritical conditions in Tangier Basin. At this stage of the tide the Atlantic flow is reversed over Camarinal Sill, as the large pool of Atlantic water in the subcritical portion between Camarinal Sill and Tarifa Narrows (see previous synopsis) spreads out both to the east and west. The flow passes through a control in Tarifa Narrows, becoming supercritical in the eastern part of the Strait. This supercritical portion is characterized by some mixing and associated finestructure in the density profiles.

It is interesting to note that despite the underlying asymmetry of maximal exchange through the combination of a contraction and sill discussed by FARMER and ARMI (1986), the time dependent response has a certain similarity on either side of the sill. As noted earlier (Chapter 6), Tangier Basin acts as a reservoir internal to the control region, that periodically fills and drains on each tidal cycle. As the Tangier Basin drains, the interface drops below the changing interface level east of Camarinal Sill and the control is re-established. Except on the weakest tides it floods the control for approximately one half of the tidal cycle. East of Camarinal Sill, between the sill and the contraction, there is another fluctuating reservoir of water. In this case it is the

Atlantic water that fills or drains from this section of the Strait. Just as Tangier Basin can drain from both ends on a falling tide, so does the pool of Atlantic water east of Camarinal drain from both ends (i.e. west over Camarinal Sill and east through Tarifa Narrows) on a rising tide.

Similarly, the bores are released from the sill at opposite tidal phases; the large bore travelling to the east is released near High Water, the small westward travelling bore at Low Water. These bores convey information, in the hydraulic sense, that control has been lost over Camarinal Sill at the end of each respective half-tidal cycle. The large bore becomes significant to the Tarifa control as it moves into the narrows. As the bore enters a supercritical flow and leaves a subcritical flow in its wake, the control point moves east with the bore. This continues until the bore is sufficiently weak, that the flow is supercritical both ahead and behind it. This happens, for example, at Station 13E (see Figures 8.7, 8.8).

In the eastern part of the Strait then, the bore has the effect of moving the control point further east during each falling tide. After it has passed, supercritical flow will again re-establish itself in the central or western part of Tarifa Narrows. In the western part of the Strait, the sill controls change in a more abrupt pattern, with control being lost at Camarinal Sill and Spartel Sill close to High Water. It is important to understand that these movements in the control position, together with the associated changes in internal reservoir interface heights, occur wholly between the supercritical flows bounding the Strait. The volume flux in each layer will be a fluctuating function of tidal phase, and the horizontal extent of the controlled region is modified as the controls change position. But, since all of these effects lie within the bounding supercritical flows that we observed during our April cruise, they do not violate the fundamental requirement for maximal exchange during the period of our observations.

In Figure 14.1b we show the corresponding diagram for the neap tide. We had substantially less data from this period; nevertheless, it is possible to put together a synopsis of the tidal variation in the Strait. The data from Figure 4.1 and the four moorings provide the basis for our compilation. In the first synopsis, one hour before High Water, the outflowing deeper layer is almost unchanged from the spring tide over Spartel West, and similar though slightly weaker over Spartel Sill. Over Camarinal the outflow remains quite strong ($1.2\ m\ s^{-1}$), even though the tidal component is weak. Hydraulic control occurs over Camarinal Sill. There is no westward travelling bore in Tangier Basin, because, as shown below, there is no reverse flow over Camarinal Sill during the falling tide.

At High Tide (second synopsis) the Mediterranean outflow over Camarinal Sill is slightly stronger than at springs ($1.1\ m\ s^{-1}$ vs $0.7\ m\ s^{-1}$). A smaller bore is shown travelling east from the sill (dotted line), although, as indicated in Chapter 12, our moorings did not detect bores on some of the weak tides.

The third synopsis, one hour before Low Water, differs most from the corresponding spring tide. Instead of a reverse flow over Camarinal Sill, the Mediterranean water continues to move west, at a speed of $0.7\ m\ s^{-1}$, while the Atlantic water moves east at $0.9\ m\ s^{-1}$.

Finally, at Low Water the control is re-established over Camarinal Sill, although, in contrast to the spring tide, a modest inflow of Atlantic water persists in the surface layer.

Although the tidal components are the dominant part of the barotropic forcing, and our time series observations extending over a single spring-neap tidal cycle have been analyzed as a tidal response, lower frequency components caused by meteorological events are also present. For example, Julio Candela (personal communication) has found tidally averaged variability at time

scales of several days to weeks in the surface layer flow and thickness just east of the exit. (At this substantial distance from the highly nonlinear flow near the sill, a tidal average appears to be a useful representation of low frequency fluctuations.) An atmospherically forced inflow, for example, would bias the hydraulic response to the tide so that the interface was consistently deeper than it otherwise would be, whereas for an atmospherically forced outflow it would be shallower. The tidally averaged data considered by Candela are consistent with this hydraulic interpretation.

This experimental study of the Strait of Gibraltar has revealed a complicated pattern of time dependent hydraulic fluctuations involving changing interfacial levels and moving control points at different stages of the tide. Despite these complications, the observations can be interpreted within the framework of the internal hydraulic theory developed by ARMI and FARMER (1986) and FARMER and ARMI (1986), subject to those various time dependent effects.

Although the maximal exchange solution defines the exchange based upon processes lying within the control volume, it is important to keep in mind that it is ultimately driven by the density difference between the water on either side of the Strait. The time constant associated with changing properties of the outflowing Mediterranean water is many years, but seasonal fluctuations undoubtedly occur in the inflowing Atlantic surface waters (BORMANS, GARRETT and THOMPSON, 1986). The resulting change in relative density difference will result in a seasonal fluctuation in the exchange rate.

Our study of exchange through the Strait of Gibraltar has been guided by the recognition that the flow is inherently nonlinear, and therefore most appropriately analyzed in terms of internal hydraulics. There are a number of intriguing complications that have appeared in the problem, including the existence of an internal reservoir, the time dependent response and its manifestation in a travelling bore, and possibly additional geometrical factors and frictional effects. Nonetheless, the basic concept of maximal exchange, which was developed from the original overmixing concept of STOMMEL and FARMER (1953), retains an elegant simplicity. If the maximal exchange requirements are met, as was the case in April 1986, the exchange is fully determined by the geometry of the Strait and time dependence of the barotropic component, together with the relative density difference of the two layers.

## ACKNOWLEDGEMENTS

This study of the Strait of Gibraltar was made possible through the skill and dedication of many people. We are especially grateful to Al Stickland and Reg Bigham for their successful deployment and recovery of our full complement of current meters and thermistor chains; to Ron Teichrob for organizing the technical aspects of our two cruises and the successful operation of our ship-board instrumentation; to Grace Kamitakahara-King and Sharon Yamasaki for organizing our data collection at sea and for extensive data processing; to Nancy Hulbirt for her painstaking organization of the processed data and its presentation in the figures; to Daniella Di Iorio for assistance in data analysis and Ben Huber for help both at sea and with data processing; to Netta Delacretaz and Dana Dahlbo for expert typing and secretarial assistance; to Brian Watt for photography and Guy Tapper for graphic assistance and poofreading; to our two scientific observers, Perfecto Villeneuva Guimerans and Driss Khomsi; to Don Moller for organizing ship support and arrangements; to Paul Howland, Mike Palmieri and the crews of OCEANUS and LYNCH for excellent assistance at sea; to Jim Hannon for his assistance with the expendable profiler program; to Mike Gregg for lending us his acoustic Doppler profiler and for his assistance in the deployment and processing of data from the expendable current profilers; to Harry Bryden and Tom Kinder for assistance with many organizational aspects of the Gibraltar Experiment; and to Claude Richez for arranging the provision of 200 XBTs from the French Navy. This work was supported by the US Office of Naval Research under their Straits Program as well as their Physical Oceanography Program, together with support from the Institute of Ocean Sciences, B.C.

We are much indebted to our referees and colleagues for providing us with many helpful comments, especially to Tom Kinder for a most careful and thorough review of the manuscript, to Chris Garrett and Myriam Bormans for many stimulating discussions and comments and to Claude Richez for her contributions in providing us with perspective on the earlier work in the Strait. We are also grateful to our editor, Bob Smith, for guiding this complex manuscript through to publication. Finally, we acknowledge our colleagues on the Rock of Gibraltar (see dedication) whose level of interest in our work provided us with insight on the true significance of the processes we were studying.

# REFERENCES


ARMI, L. (1986) The hydraulics of two flowing layers with different densities. *J. Fluid Mech.*, **163,** 27-58.

ARMI, L. and D. M. FARMER (1985) The internal hydraulics of the Strait of Gibraltar and associated sills and narrows. *Oceanologica Acta,* **8,** 37-46.

ARMI, L. and D.M. FARMER (1986) Maximal two-layer exchange through a contraction with barotropic net flow. *J. Fluid Mech.,* **164,** 27-51.

ARMI, L. and D. M. FARMER (1987) A generalization of the concept of maximal exchange in a strait. *J. Geophys. Res.,* **92,** 14679-14680.

ASSAF, G. and A. HECHT (1974) Sea straits: a dynamic model. *Deep-Sea Research,* **21**, 947-958.

BELL, W.H. (1979) A three-dimensional subsurface mooring model. *Pacific Marine Sciences Report* **79-20,** Institute of Ocean Sciences, Patricia Bay, British Columbia, 48pp.

BØYUM, G. (1967) Hydrology and currents in the area west of Gibraltar. Technical Report No. 36, NATO Subcom. Ocean Res. Mediterranean Outflow Project.

BORMANS, M., C. GARRETT and K.R. THOMPSON (1986) Seasonal variability of the surface inflow through the Strait of Gibraltar. *Oceanologica Acta,* **9,** 403-414.

BROWN, G. and A. ROSHKO (1974) On density effects and large structure in turbulent mixing layers. *J. Fluid Mech.,* **64,** 775-816.

BRYDEN, H.L. and H.M. STOMMEL (1984) Limiting processes that determine basic features of the circulation in the Mediterranean Sea. *Oceanologica Acta,* **7,** 289-296.

CHOW, V.T. (1959) *Open-channel hydraulics.* McGraw-Hill Book Co., New York, 680pp.

DEACON, M. (1985) An early theory of ocean circulation: J.S. Von Waitz and his explanation of the currents in the Strait of Gibraltar. *Progress in Oceanography,* **14,** 89-101.

DEFANT, A. (1961) *Physical Oceanography.* Pergamon Press, Oxford, Vol. I, 729pp.

Defense Mapping Agency, Chart 52041 (1980) *Strait of Gibraltar,* 41st Ed., August 9, 1980, Defense Mapping Agency Hydrographic/Topographic Center, Washington, D.C. 20315.

FARMER, D.M. and L. ARMI (1986) Maximal two-layer exchange over a sill and through the combination of a sill and contraction with barotropic flow. *J. Fluid Mech.,* **164,** 53-76.

FARMER, D.M., G.B. CRAWFORD and T.R. OSBORN (1987) Temperature and velocity miscrostructure caused by swimming fish. *Limnol. Oceanogr.,* **32(4),** 978-983.

FARMER, D.M. and R.A. DENTON (1985) Hydraulic control of flow over the sill in Observatory Inlet. *J. Geophys Res.,* **90,** 9051-9068.

FARMER, D.M and H.J. FREELAND (1983) The physical oceanography of fjords. *Progress in Oceanography,* **12,** 147-220.

FARMER, D.M. and J.D. SMITH (1980) Tidal interaction of stratified flow with a sill in Knight Inlet. *Deep-Sea Research,* **17**, 239-254.

GARRETT, C., K. THOMPSON and J. AKERLEY (1989) Low frequency fluctuations in the Strait of Gibraltar from MEDALPEX sea level data. Submitted to *J. Physical Oceanography* October, 1988.

HANSEN, D.S. (1985) Asymptotic performance of a pulse-to-pulse incoherent Doppler sonar in an oceanic environment. *IEEE Journal of Oceanographic Engineering,* **OE-10(2),** 144-158.

HEEZEN, B.D. and G.L. JOHNSON (1969) Mediterranean undercurrent and microphysiography west of Gibraltar. *Bull. Inst.. Oceanogr. Monaco* , **67,** No. 1382, Fig. 33, p. 95.

HENDERSON, F.M. (1966) *Open channel flow.* The Macmillan Company, New York, 522pp.

HOGG, N.G. (1985) Multilayer hydraulic control with application to the Alboran Sea circulation. *J. Phys. Oceanogr.*, **15**, 454-466.

HOLMBOE, J. (1962) On the behaviour of symmetric waves in stratified shear layers. *Geofys. Publ.*, **24,** 67.

Instituto Geográfico National y SECEG (1988) *Estrecho de Gibraltar*, Instituto Geográfico Nacional, General Ibañez de Ibero, 3-28071, Madrid, Spain.

KENYON, N.H. and R.H. BELDERSON (1973) Bed forms of the Mediterranean undercurrent observed with side-scan sonar. *Sedimentary Geology,* **9,** 77-99.

KINDER, T.H. and H.L. BRYDEN (1987) The 1985-1986 Gibraltar experiment: data collection and preliminary results. *EOS,* **68**, No. 40, 786.

KINDER, T.H. and G. PARRILLA (1987) Yes, some of the Mediterranean outflow does come from great depth. *J. Geophys. Res.*, **92,** 2901-2906.

KOOP, C.G. and F.K. BROWAND (1979) Instability and turbulence in a stratified fluid with shear. *J. Fluid Mech.*, **93**, 135-159.

LACOMBE, H. and C. RICHEZ (1982) The regime of the Strait of Gibraltar, In: *Hydrodynamics of semi-enclosed seas,* edited by J.C.J. Nihoul, *Elsevier Oceanogr., Ser.* **34,** 13-73.

LACOMBE, H. and C. RICHEZ (1984) Hydrography and currents in the Strait of Gibraltar. *Sea Straits Research Atlas SSR-3,* National Ocean Research and Development Activity, NSTL, Mississippi 39529.

PRATT, L.J. (1986) Hydraulic control of sill flow with bottom friction. *J. Phys. Oceanogr.*, **16,** 1970-1980.

STOMMEL, H. and H.G. FARMER (1953) Control of salinity in an estuary by a transition. *J. Marine Res.*, **12,** 13-20.

WAITZ, J.S. (1755) Undersokning om orsaken, hvarföre vattnet i Atlantiska hafvet altid strömar in uti medelhafvet, genom Sundet vid Gibraltar. *Kungliga Svenska Vetenskapsakademiens Handlingar,* **16,** 27-50.

WESSON, J.C. and M.C. GREGG (1988a) Turbulent dissipation in the Strait of Gibraltar and associated mixing. In: *Small-scale turbulence and mixing in the ocean,* Proceedings of the 19th International Liege Colloquium on Ocean Hydrodynamics, J.C. Nihoul and B.M. Jamart, editors, Elsevier, Amsterdam, 201-212.

WESSON, J.C. and M.C. GREGG (1988b) Dissipation measurements in the Gibraltar experiment. In: Taller Sobre La Oceanografia Fisica del Estrecho de Gibraltar - Workshop on Physical Oceanography in the Straits of Gibraltar, Madrid, 24-28 de Octubre 1988, Comunicaciones, No. 23.

WILKINSON, D.L. and I.R. WOOD (1971) A rapidly varied flow phenomenon in a two-layer flow. *J. Fluid Mech.*, **47**, 241-256.

ZEDEL, L.J. and J.A. CHURCH (1987) Real-time screening techniques for Doppler current profiler data. *Journal of Atmosphere & Ocean Technology,* **4,** 572-581.

# TABLE I: INSTRUMENTATION

**High-Frequency Echosounder**

Biosonics Model l0l and International Transducer Corporation narrow beam transducer

| | |
|---|---|
| frequency: | 120 KHz |
| pulse duration: | 1 ms |
| repetition rate: | 1 Hz |
| beam width: | 3° |

**Acoustic Doppler Current Profiler**

RD Instruments 150

(trigger combined with high-frequency echo sounder to avoid cross talk)

| | |
|---|---|
| frequency: | 150 KHz |
| pulse duration: | 5 ms |
| repetition rate: | 1 Hz |

**Recording Current Meter**

Aanderaa RCM 4

| | |
|---|---|
| direction: | 0.35 ° resolution, ± 5 ° accuracy (0.05–1ms$^{-1}$), ±7.5° accuracy (1–2ms$^{-1}$) |
| speed: | ± 0.01ms$^{-1}$ or ± 2 % (whichever is greater) |
| conductivity: | ± 0.1% of 33 mmho range |
| temperature: | ± 0.05% of 24°C range |
| pressure: | ± 1% of 350 dbar range |
| salinity: | ± 0.04 |

**CTD Profiler**

Neil Brown Instrument Systems Mark III B

(two-headed with redundant conductivity, temperature and pressure sensors)

| | |
|---|---|
| sample rate: | 25 Hz |
| temperature: | 1 m ° C resolution, 10 m ° C accuracy |
| salinity: | 0.001 PSU resolution, 0.010 PSU accuracy |
| pressure: | 0.1 dbar resolution, 3 dbar accuracy |
| bottom sensing: | 1 sec repetition rate, Benthos pinger at 12 KHz |

**Expendable Profilers**

Sippican XBT (Models T7 and Deep-Blue)

| | |
|---|---|
| depth: | ± 2% accuracy |
| fall rate used: | d= 6.472 t – 0.00216t $^2$ |
| temperature: | ± 0.2° C accuracy, 0.01° C resolution |

Sippican XSV-1 (recorded simultaneously with XBT using Sippican supplied software)

| | |
|---|---|
| depth: | ± 2% or 5 m (whichever is greater) accuracy |
| fall rate used: | d= 0.985 (5.3672t – 0.001476t $^2$ ) |
| sound velocity: | ± 0.25 ms$^{-1}$ accuracy |

Sippican XCP

| | |
|---|---|
| relative velocity: | ± 0.01 ms$^{-1}$ (rms) |

## LIST OF FIGURES

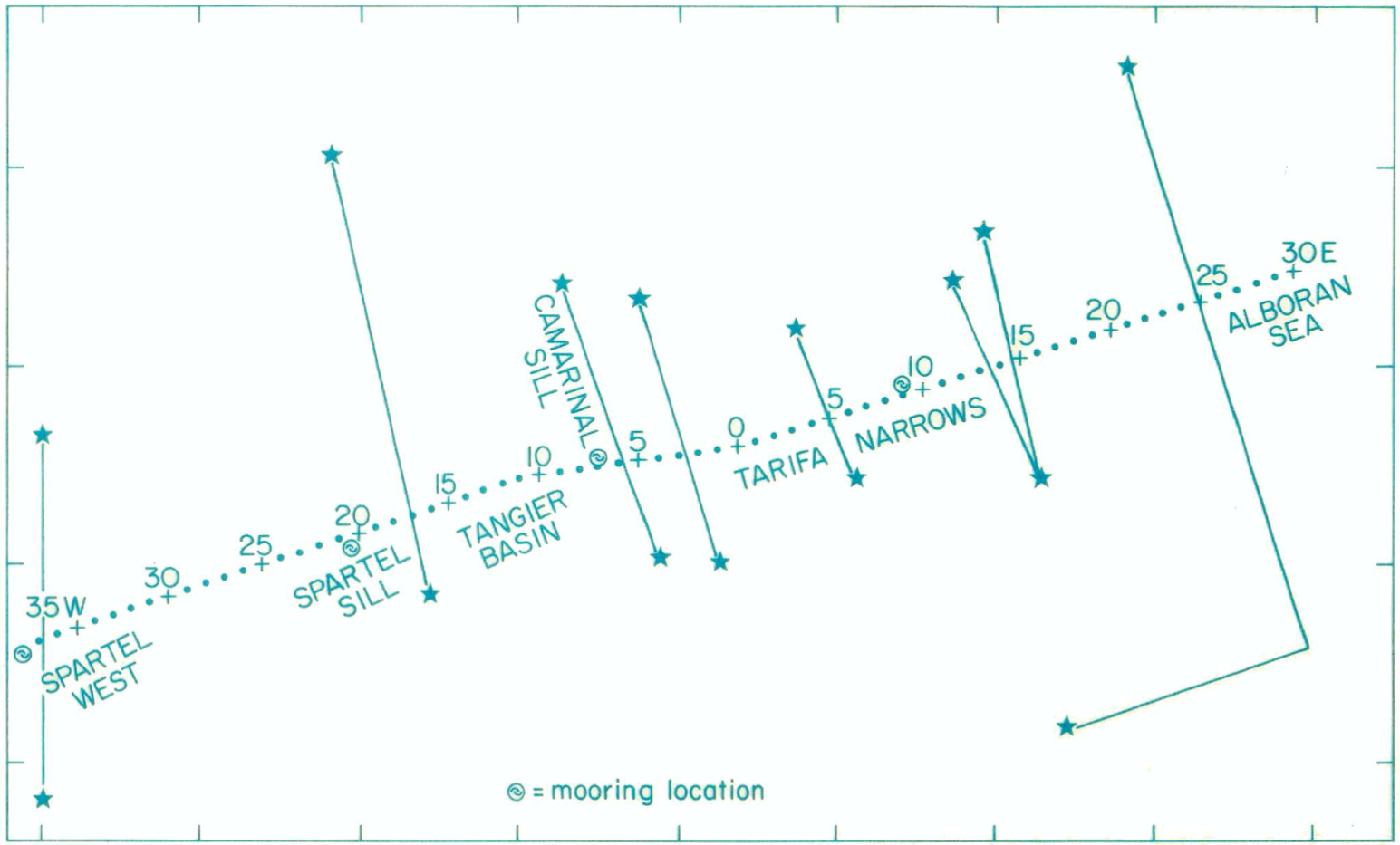
35W
30
25
20
15
10
5
0
5
10
15
20
25
30E
SPARTEL WEST
SPARTEL SILL
TANGIER BASIN
CAMARINAL SILL
TARIFA NARROWS
ALBORAN SEA
= mooring location

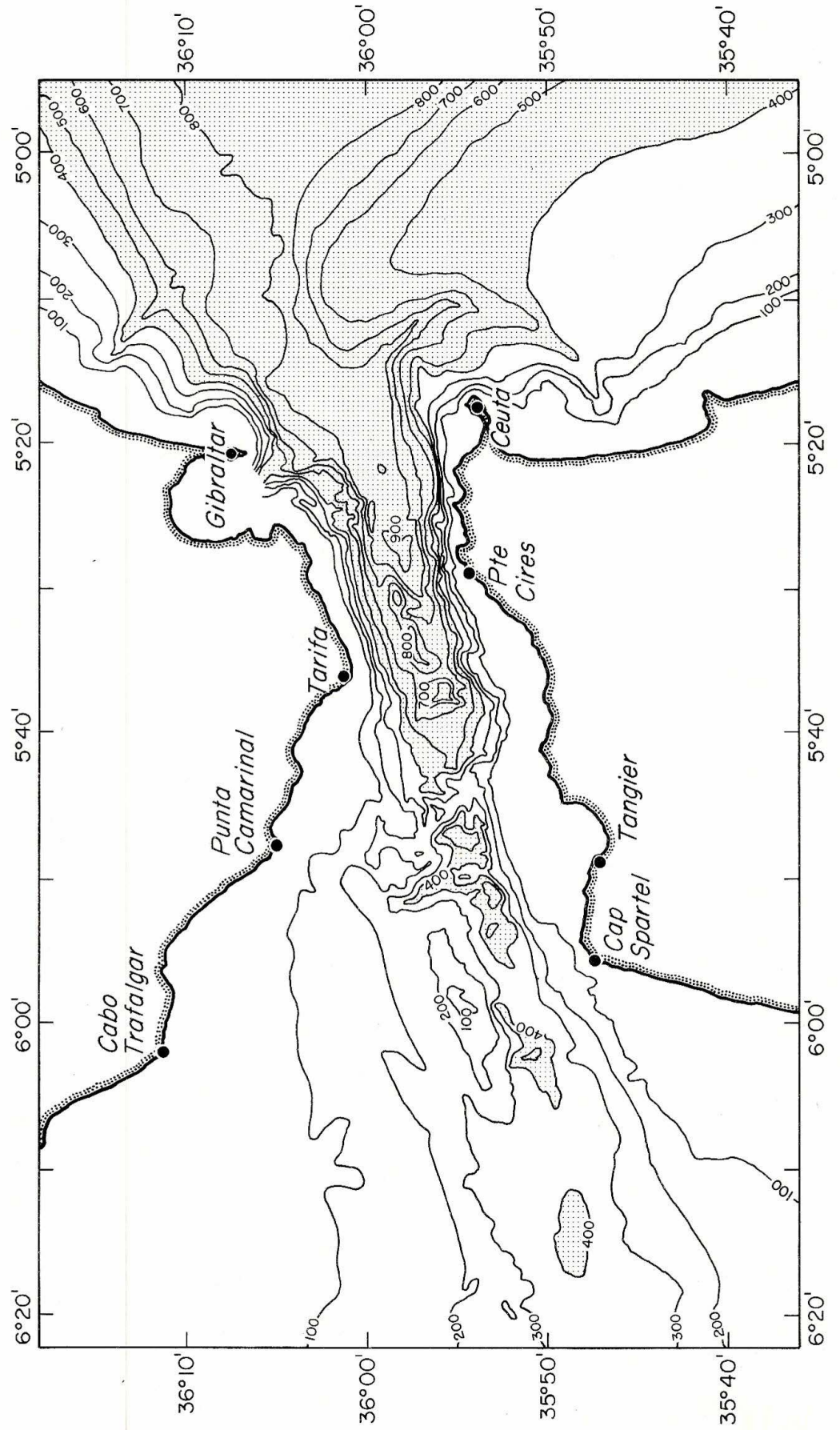


*Fig. 2.1.* Chart of the Strait of Gibraltar with depth contours in meters, based on Defense Mapping Agency (1980) chart No. 52041. Areas deeper than 400 m are shaded. *Overlay.* Location of essential topographic features, moorings, transects (solid lines between stars) and way-points (in nautical miles) for the runs.

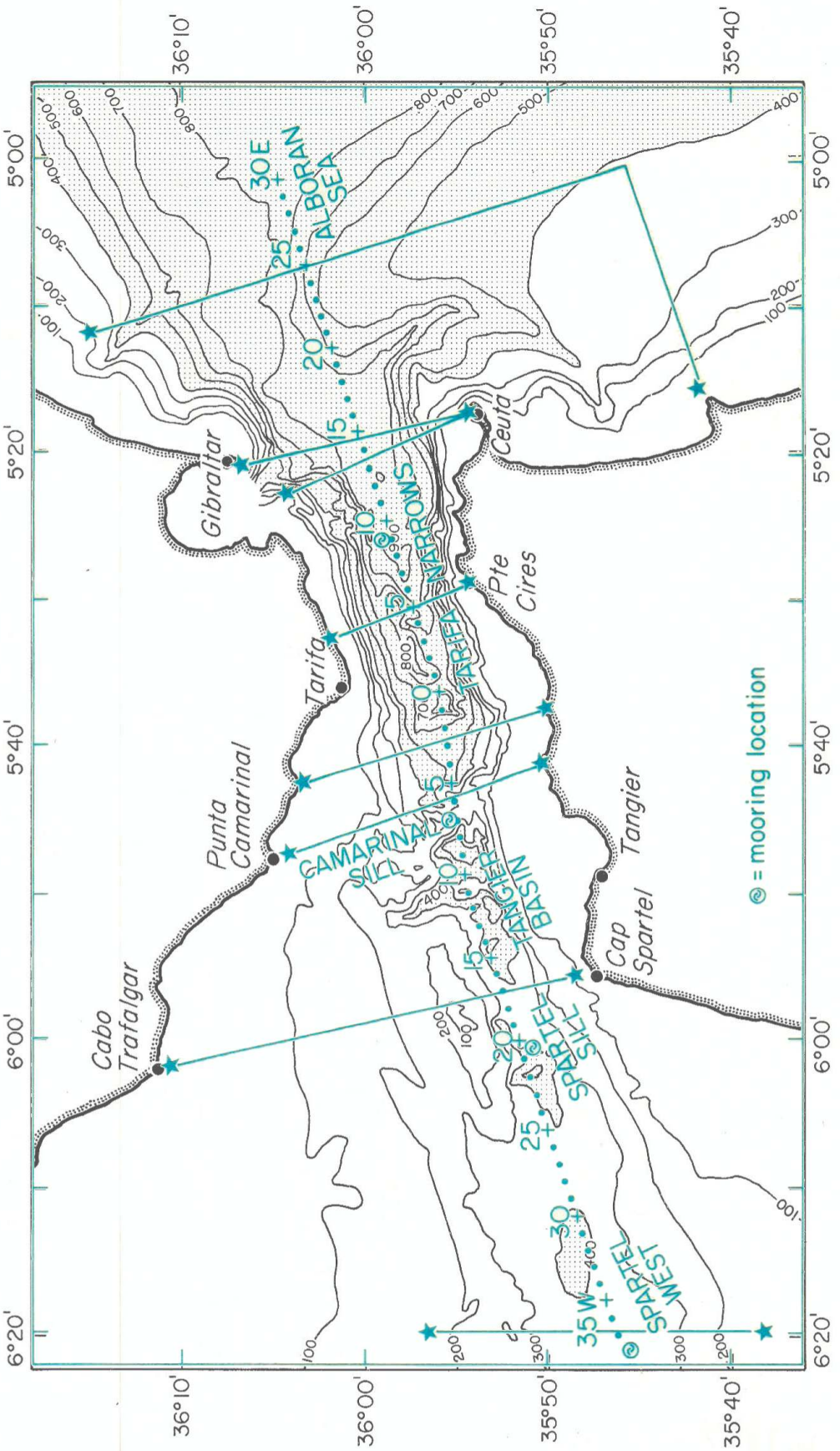


*Fig. 2.1.* Chart of the Strait of Gibraltar with depth contours in meters, based on Defense Mapping Agency (1980) chart No. 52041. Areas deeper than 400 m are shaded.
*Overlay.* Location of essential topographic features, moorings, transects (solid lines between stars) and way-points (in nautical miles) for the runs.

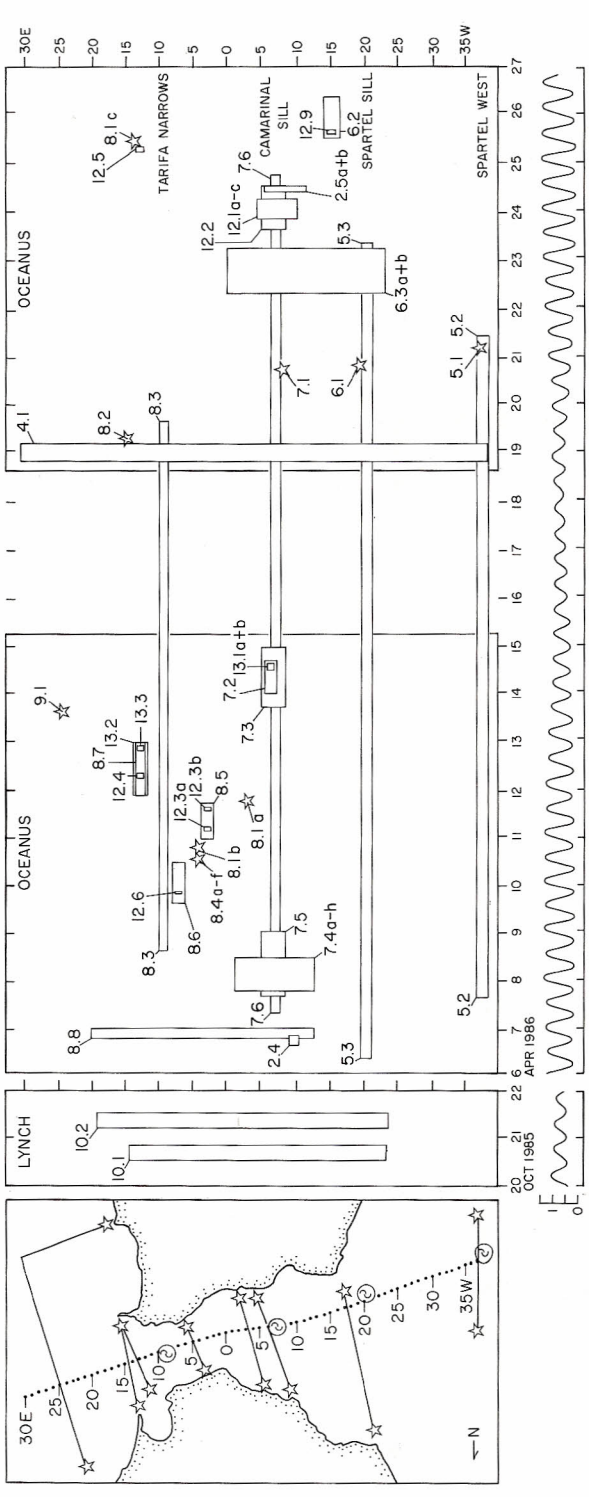


*Fig. 2.2.* A time-space history of the various components of the observational program. The vertical axis in this figure indicates the physical location of the measurements and is referenced to the adjoining chart. The time axis shows when the various ship tracks (runs, transects and time series) occurred, and the duration of moorings. Rectangles located at the corresponding positions and times of these measurements refer to the subsequent figures. The Tarifa tidal amplitude is shown beneath.

*Fig. 2.3.* Schematic diagrams showing mooring design for the recording current meters and thermistor chains at each of the four locations. The tension of the mooring line at the anchor, together with the anchor weight, is indicated at the bottom of each diagram.

*Fig. 2.4.* Profiles of temperature, sound speed, salinity and density derived from XBT/XSV expendable profilers, and also from a nearby simultaneous CTD profile. Offsets in calculated density values derived from the expendable profilers, readily apparent in this figure, are removed in subsequent figures. The CTD profile is that also shown at the western end of the run in Fig. 8.8.

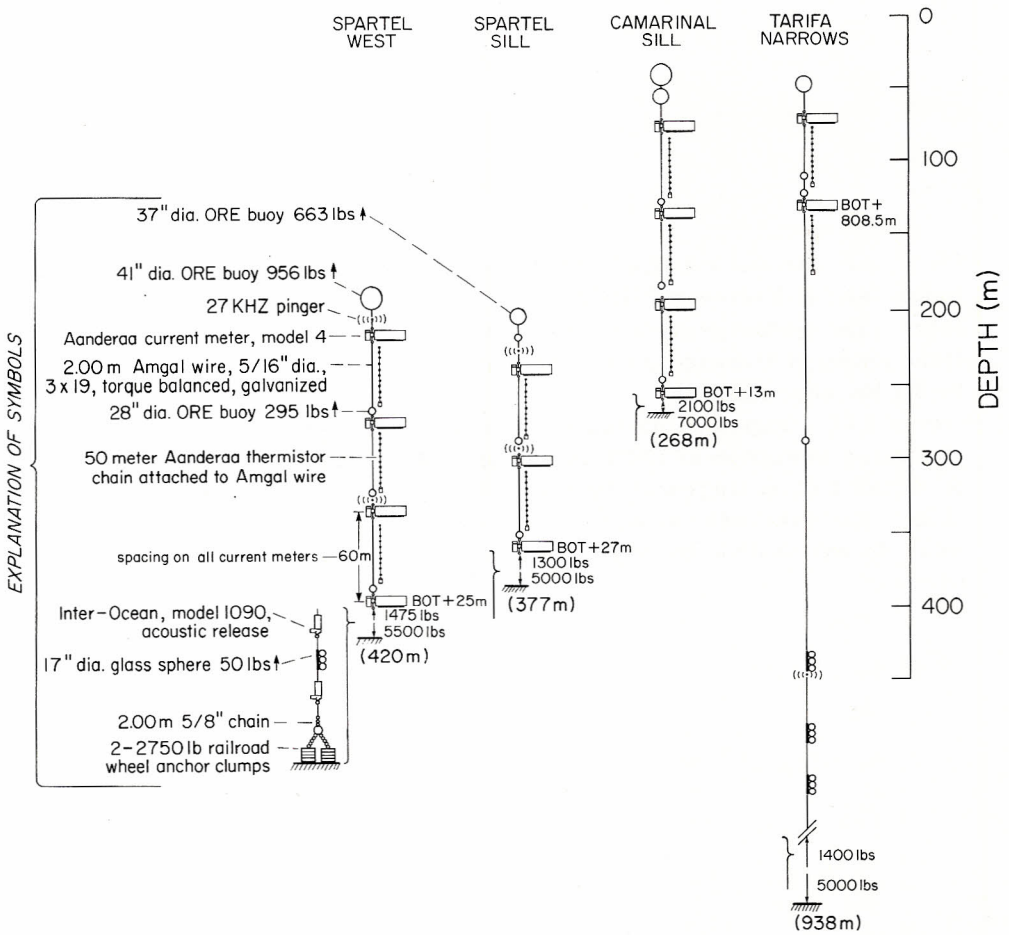
SPARTEL WEST
SPARTEL SILL
CAMARINAL SILL
TARIFA NARROWS
DEPTH (m)
0
100
200
300
400
EXPLANATION OF SYMBOLS
37" dia. ORE buoy 663 lbs
41" dia. ORE buoy 956 lbs
27 KHZ pinger
Aanderaa current meter, model 4
2.00 m Amgal wire, 5/16" dia., 3 x 19, torque balanced, galvanized
28" dia. ORE buoy 295 lbs
50 meter Aanderaa thermistor chain attached to Amgal wire
spacing on all current meters — 60m
Inter-Ocean, model 1090, acoustic release
17" dia. glass sphere 50 lbs
2.00 m 5/8" chain
2-2750 lb railroad wheel anchor clumps
BOT+25m
1475 lbs
5500 lbs
(420m)
BOT+27m
1300 lbs
5000 lbs
(377m)
BOT+13m
2100 lbs
7000 lbs
(268m)
BOT+ 808.5m
1400 lbs
5000 lbs
(938m)

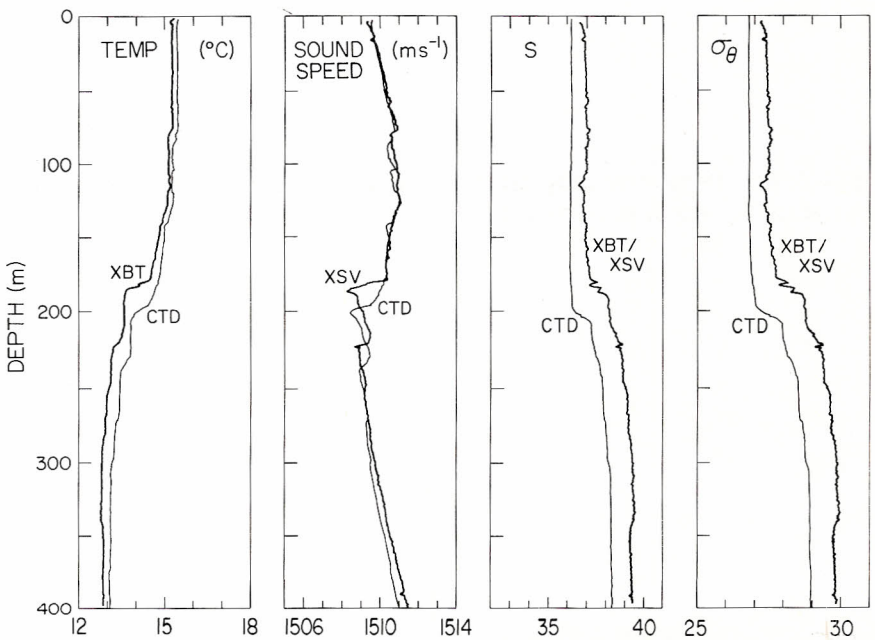
DEPTH (m)
0
100
200
300
400
TEMP (°C)
XBT
CTD
12
15
18
SOUND SPEED (ms⁻¹)
XSV
CTD
1506
1510
1514
S
XBT/ XSV
CTD
35
40
σθ
XBT/ XSV
CTD
25
30

*Fig. 2.5a,b.* Acoustic and profile measurements of flow over Camarinal Sill illustrating the various types of observational technique.

*Image.* The interface descends as water moves from east to west (left to right in this figure). Dense patches of backscatter are associated with schools of fish. Repetitive pulses are caused by dolphin sonar signals.

*Overlay 2.5a.* Temperature profiles based on XBTs obtained as the vessel moved over the sill. A reference temperature of 13.5°C is indicated with a solid circle on each profile, illustrating the distortion of the temperature field coincident with the pycnocline appearing in the acoustic image. The solid circle, as well as the triangle along the bottom, identify the position at which the measurement was taken. Open circles along the bottom are time and/or position references.

*Overlay 2.5b.* Doppler velocity profiles of East-West component of speed, together with speed and density data from the mooring.

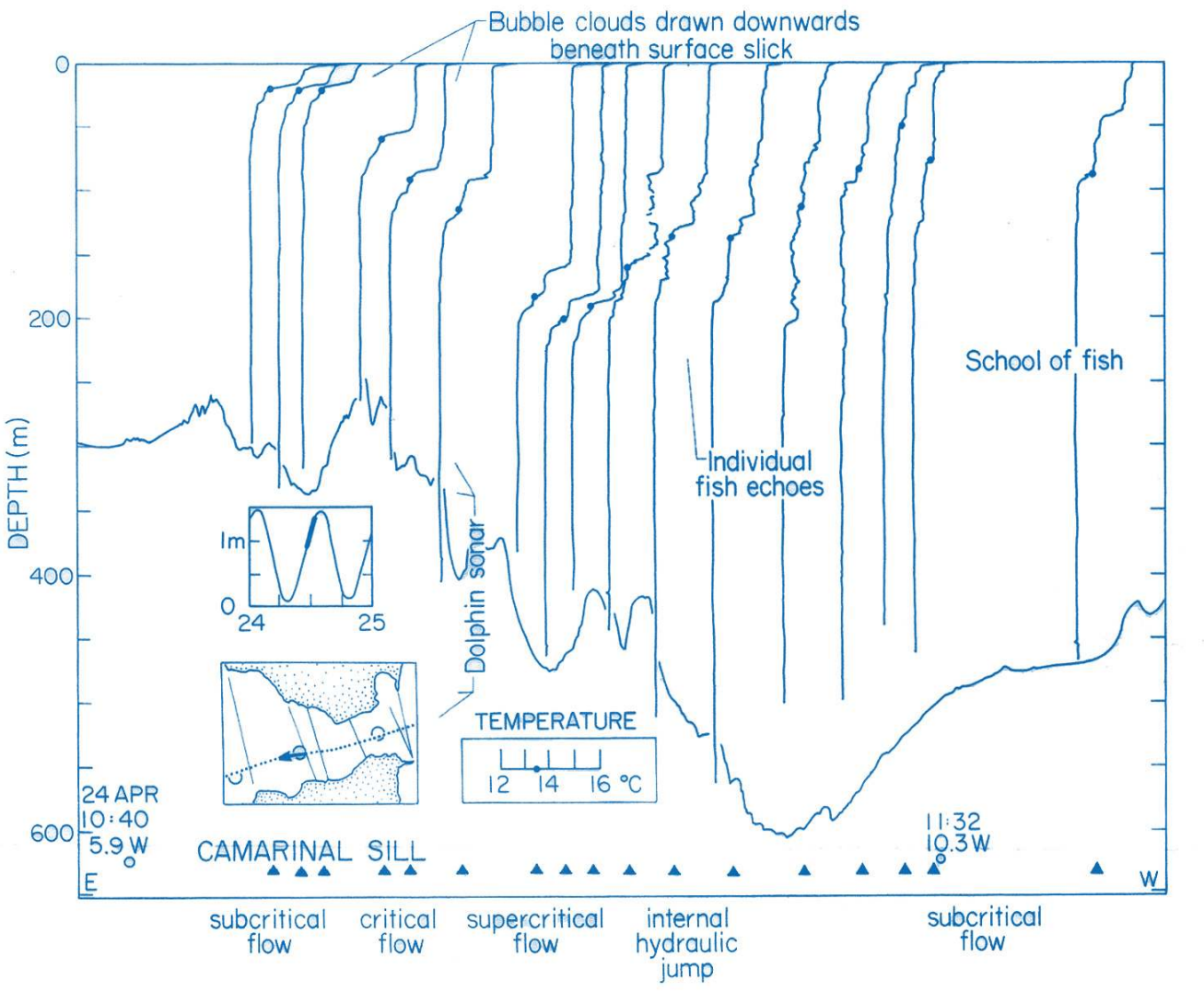
Bubble clouds drawn downwards beneath surface slick
School of fish
Individual fish echoes
Dolphin sonar
1m
0
24
25
TEMPERATURE
12 14 16 °C
24 APR
10:40
5.9 W
E
CAMARINAL SILL
11:32
10.3 W
W
DEPTH (m)
0
200
400
600
subcritical flow
critical flow
supercritical flow
internal hydraulic jump
subcritical flow

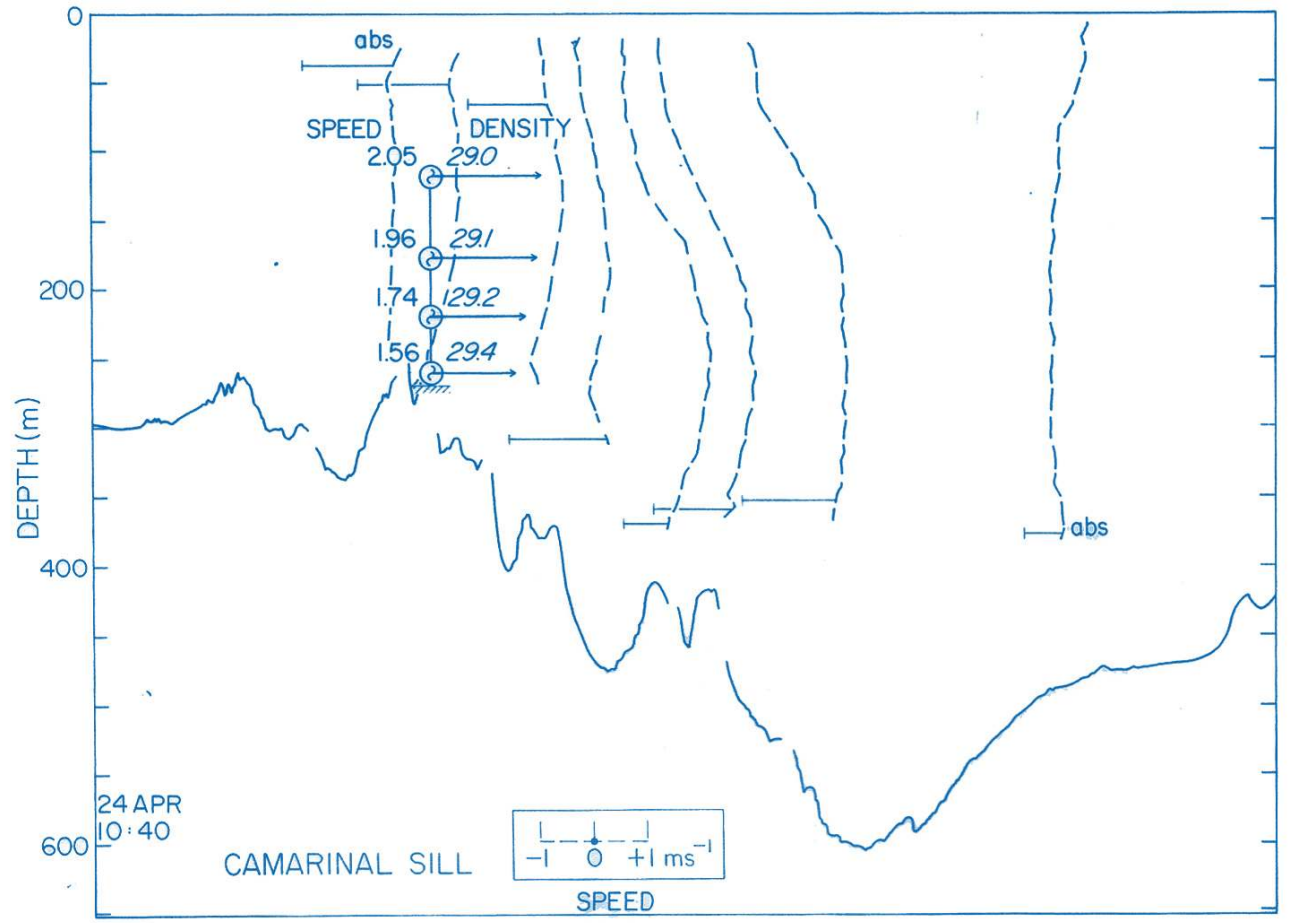
abs
SPEED
DENSITY
2.05
29.0
1.96
29.1
1.74
29.2
1.56
29.4
abs
24 APR
10:40
CAMARINAL SILL
−1 0 +1 ms⁻¹
SPEED
DEPTH (m)
0
200
400
600

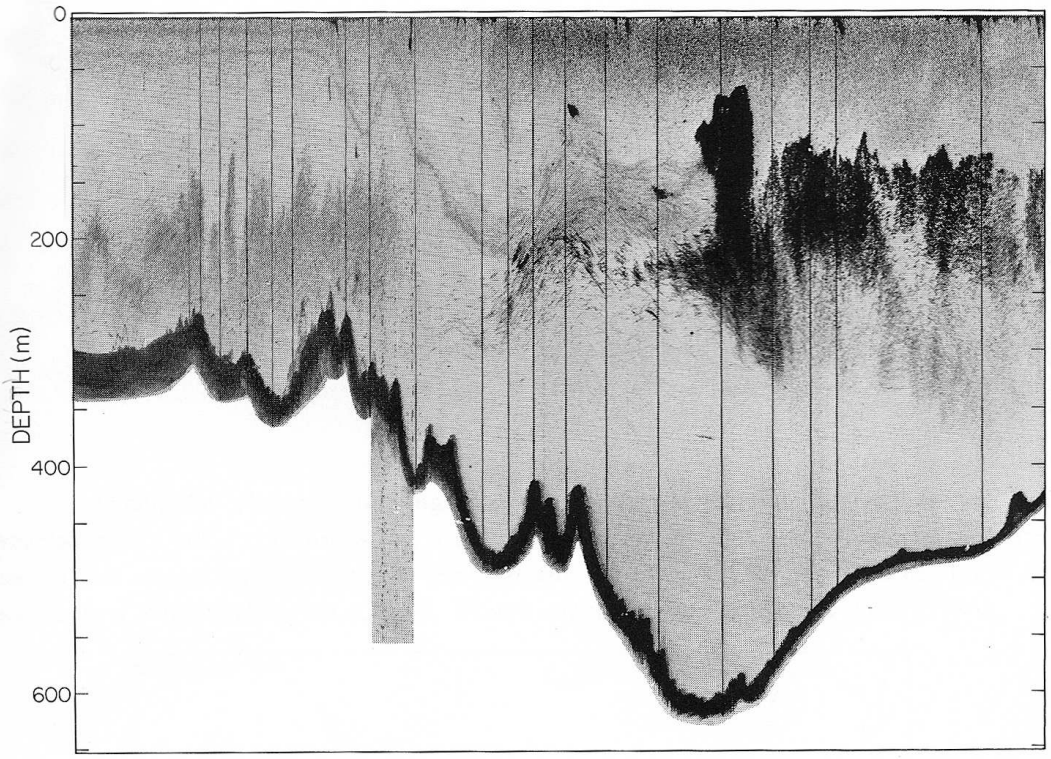
0
200
400
600
DEPTH (m)

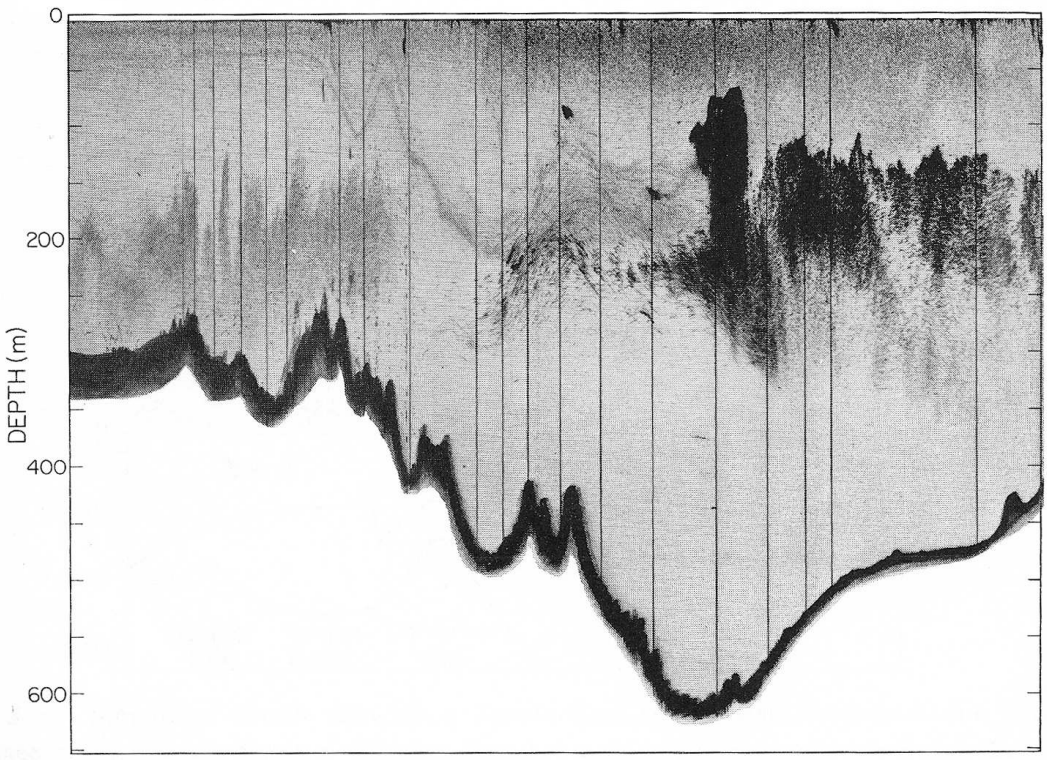
0
200
400
600
DEPTH (m)

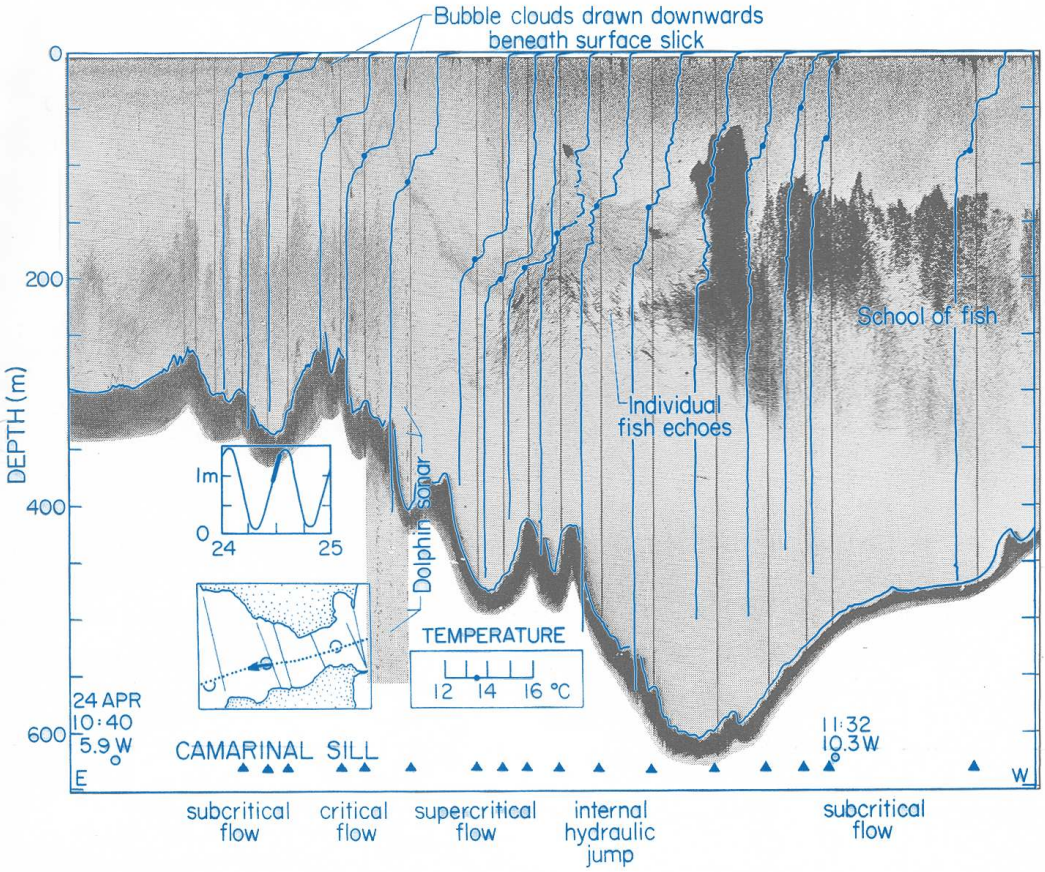
Bubble clouds drawn downwards
beneath surface slick
0
200
400
600
DEPTH (m)
School of fish
Individual
fish echoes
Dolphin sonar
1m
0
24
25
TEMPERATURE
12 14 16 °C
24 APR
10:40
5.9 W
CAMARINAL SILL
11:32
10.3 W
E
W
subcritical
flow
critical
flow
supercritical
flow
internal
hydraulic
jump
subcritical
flow

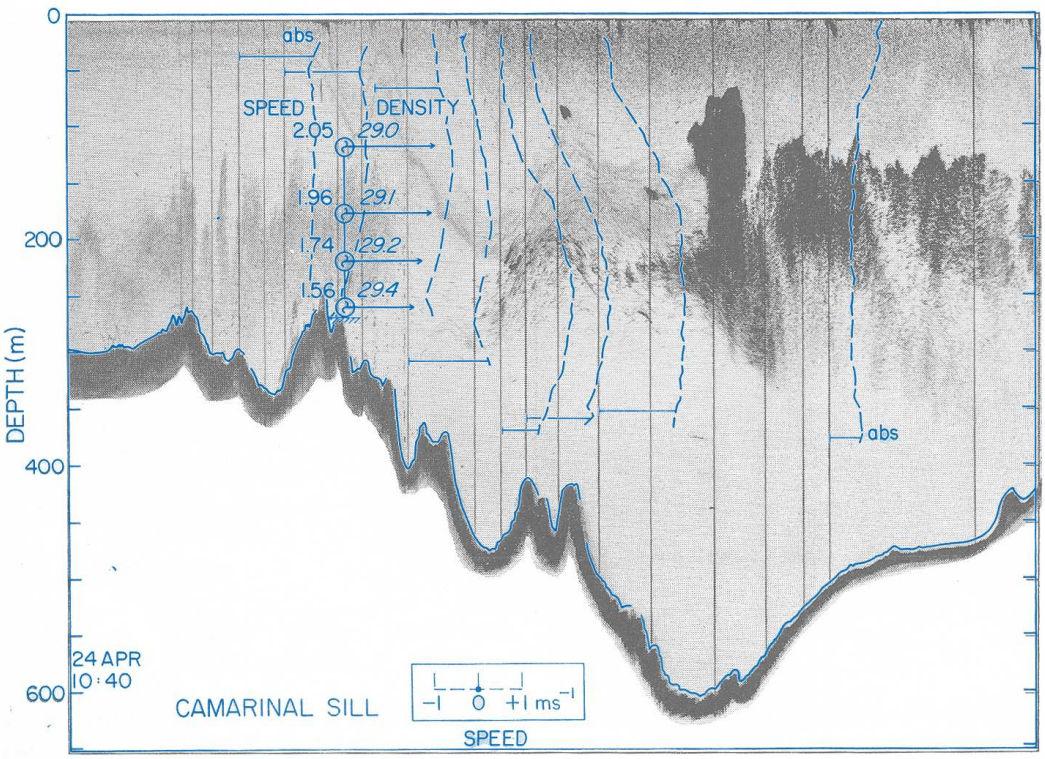
0
200
400
600
DEPTH (m)
abs
SPEED
DENSITY
2.05
29.0
1.96
29.1
1.74
29.2
1.56
29.4
abs
24 APR
10:40
CAMARINAL SILL
−1 0 +1 ms⁻¹
SPEED

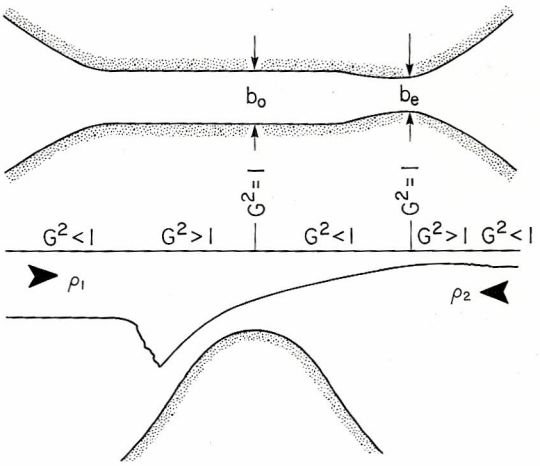


*Fig. 3.1.* Schematic diagram showing maximal exchange through a strait having both a contraction and a sill . Dense water from the reservoir on the right flows towards the left beneath a less dense layer flowing in the opposite direction. The two controls ($G^2= 1$) are connected by a subcritical region ($G^2<1$). Figure adapted from Farmer and Armi (1986).

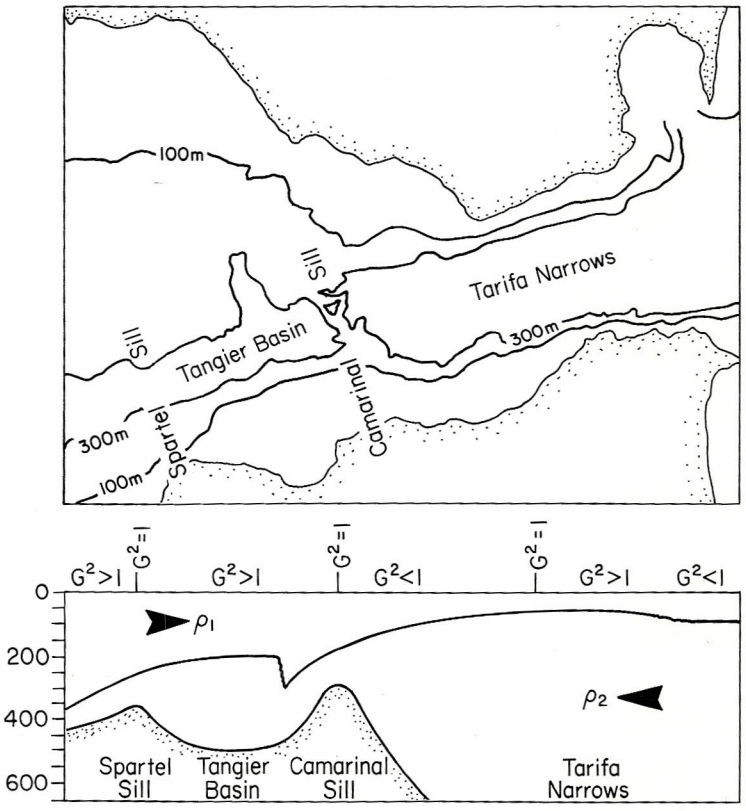


*Fig. 3.2.* Simplified sketch showing a hypothetical steady state respresentation of the interface position in the Strait of Gibraltar, together with major topographic features. Refer to Figures 14.1a,b for simplified sketches of the observed, time dependent interface position.

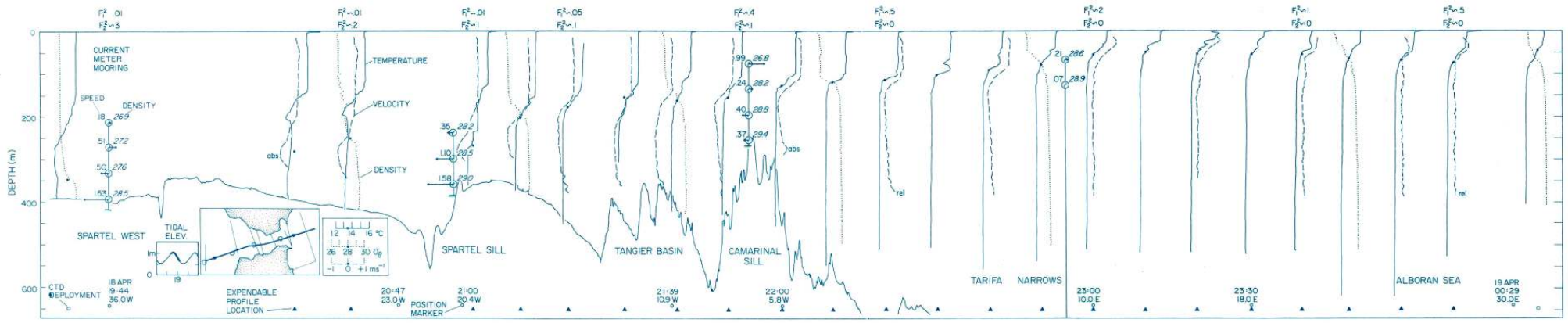
$F_1^2$ .01
$F_2^2$ ~3
$F_1^2$ ~.01
$F_2^2$ ~.2
$F_1^2$ ~.01
$F_2^2$ ~1
$F_1^2$ ~.05
$F_2^2$ ~.1
$F_1^2$ ~.4
$F_2^2$ ~1
$F_1^2$ ~.5
$F_2^2$ ~0
$F_1^2$ ~2
$F_2^2$ ~0
$F_1^2$ ~1
$F_2^2$ ~0
$F_1^2$ ~.5
$F_2^2$ ~0
DEPTH (m)
0
200
400
600
CURRENT METER MOORING
SPEED
DENSITY
18 26.9
51 27.2
50 27.6
153 28.5
TEMPERATURE
VELOCITY
DENSITY
abs
35 28.2
110 28.5
158 29.0
99 26.8
24 28.2
40 28.8
37 29.4
abs
rel
21 28.6
07 28.9
rel
SPARTEL WEST
TIDAL ELEV.
1m
0
19
12 14 16 °C
26 28 30 $\sigma_\theta$
−1 0 +1 ms⁻¹
SPARTEL SILL
TANGIER BASIN
CAMARINAL SILL
TARIFA NARROWS
ALBORAN SEA
CTD DEPLOYMENT
18 APR 19·44 36·0W
EXPENDABLE PROFILE LOCATION
20·47 23·0W
POSITION MARKER
21·00 20·4W
21·39 10·9W
22·00 5·8W
23·00 10·0E
23·30 18·0E
19 APR 00·29 30·0E

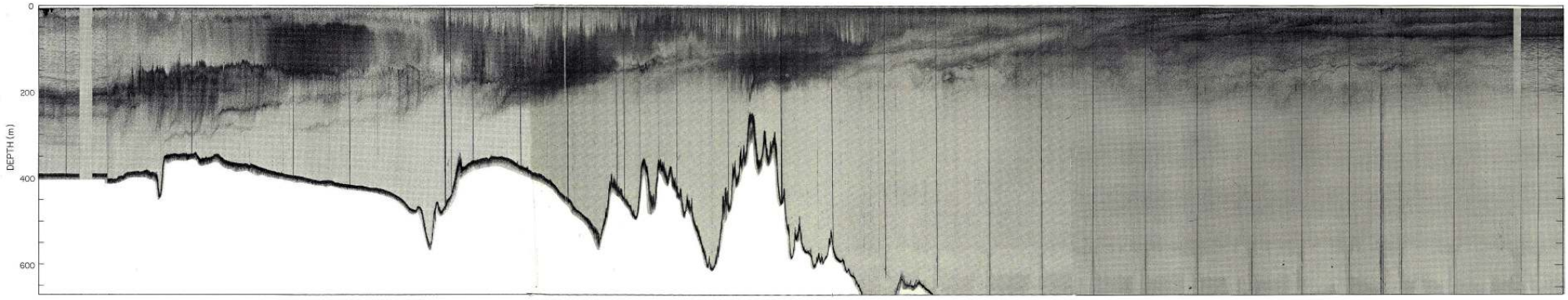


*Fig. 4.1.* Acoustic image of a run along the full length of the Strait illustrating the main hydraulic features.
*Overlay.* Termperature profiles (solid lines), density profiles (dotted lines) and velocity profiles (dashed lines). The solid circles on each profile are used both to identify specific values (i.e. 13.5°C, 28.0, 0ms$^{-1}$ respectively), and also to identify the time and position of the measurement. The tidal height during the course of the run is indicated as a thick line superimposed on the tidal time series. Horizontal arrows indicate the direction and strength of currents measured at the mooring sites . Density is also given where available. The current meter moorings were usually displaced to either side of the ship track; perfect correspondence of moored and Doppler profile data cannot be expected.

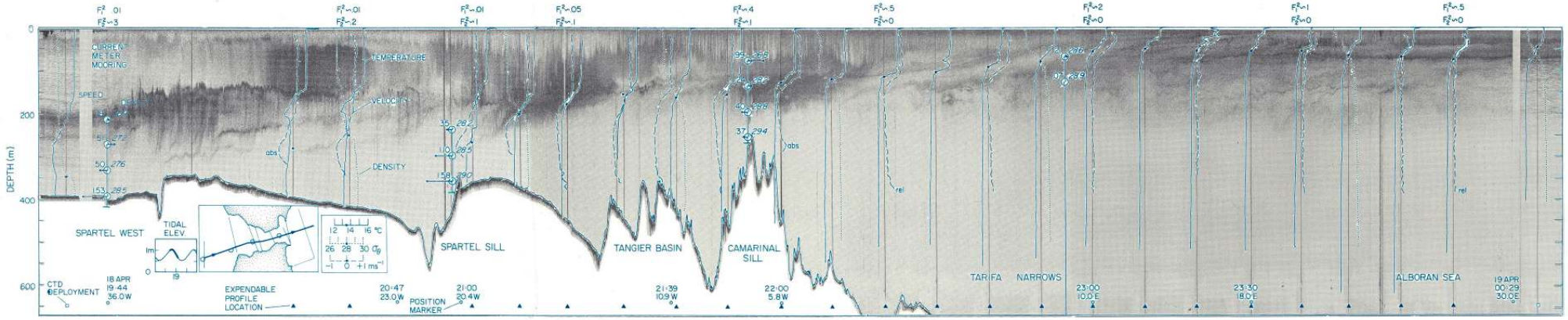


*Fig. 4.1.* Acoustic image of a run along the full length of the Strait illustrating the main hydraulic features.

*Overlay.* Termperature profiles (solid lines), density profiles (dotted lines) and velocity profiles (dashed lines). The solid circles on each profile are used both to identify specific values (i.e. 13.5°C, 28.0, 0ms$^{-1}$ respectively), and also to identify the time and position of the measurement. The tidal height during the course of the run is indicated as a thick line superimposed on the tidal time series. Horizontal arrows indicate the direction and strength of currents measured at the mooring sites . Density is also given where available. The current meter moorings were usually displaced to either side of the ship track; perfect correspondence of moored and Doppler profile data cannot be expected.

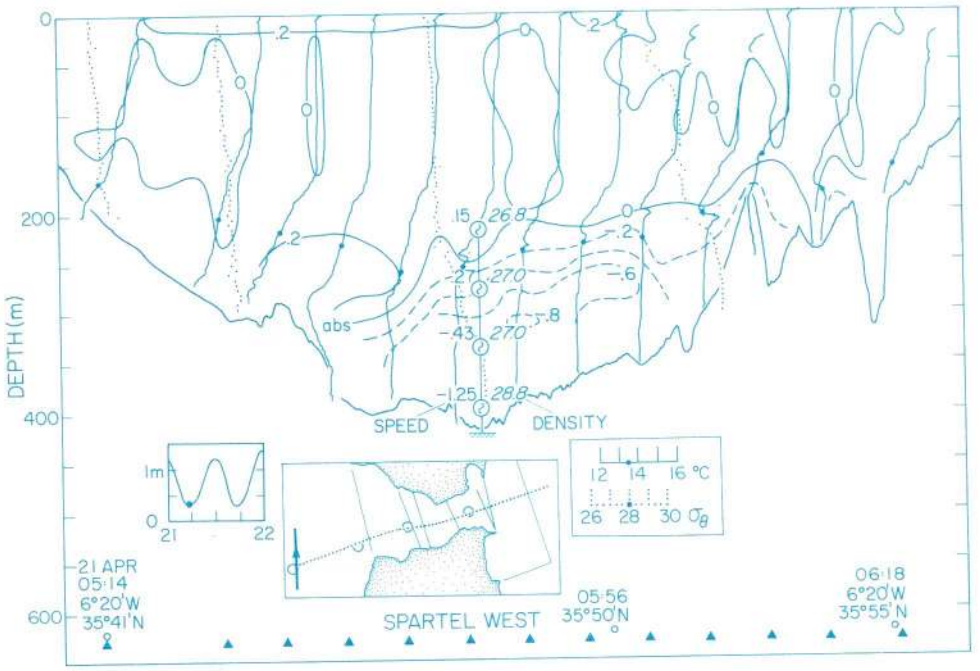
0
200
400
600
DEPTH (m)
.2
.2
.2
.15
26.8
27
27.0
-.43
27.0
-1.25
28.8
0
-.2
-.6
-.8
abs
SPEED
DENSITY
1m
0
21
22
12
14
16 °C
26
28
30 $\sigma_\theta$
21 APR
05:14
6°20'W
35°41'N
SPARTEL WEST
05:56
35°50'N
06:18
6°20'W
35°55'N

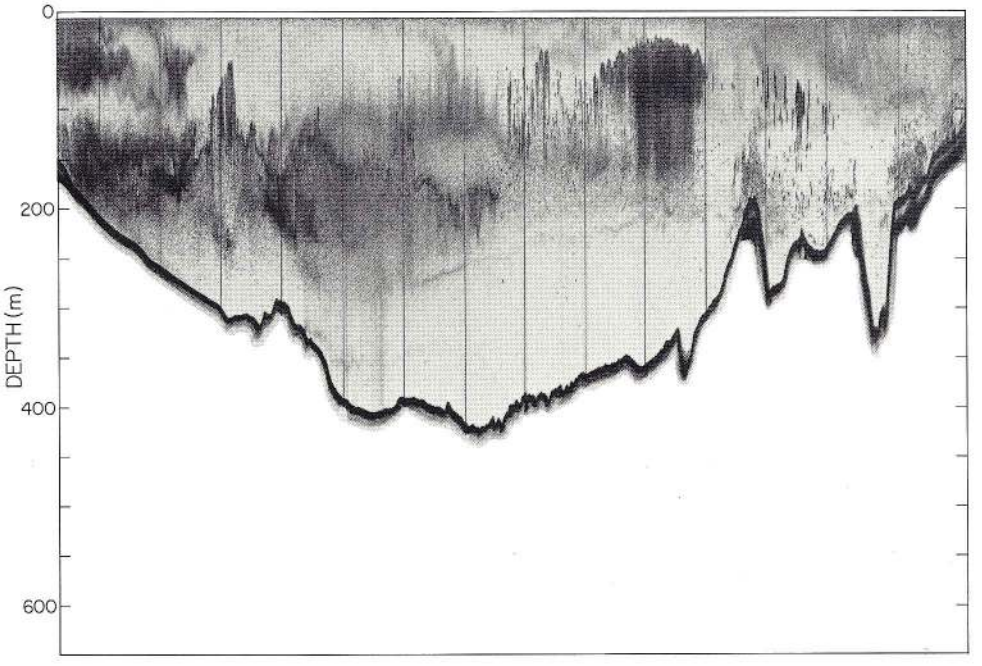


*Fig. 5.1.* A transect across Spartel West, showing the sloping interface separating the two layers.
*Overlay.* Temperature profiles (solid lines) and, less often, density profiles (dotted lines), together with contours of constant flow speed (along channel component) derived from Doppler data. Values on contours indicate flow speed in $ms^{-1}$.

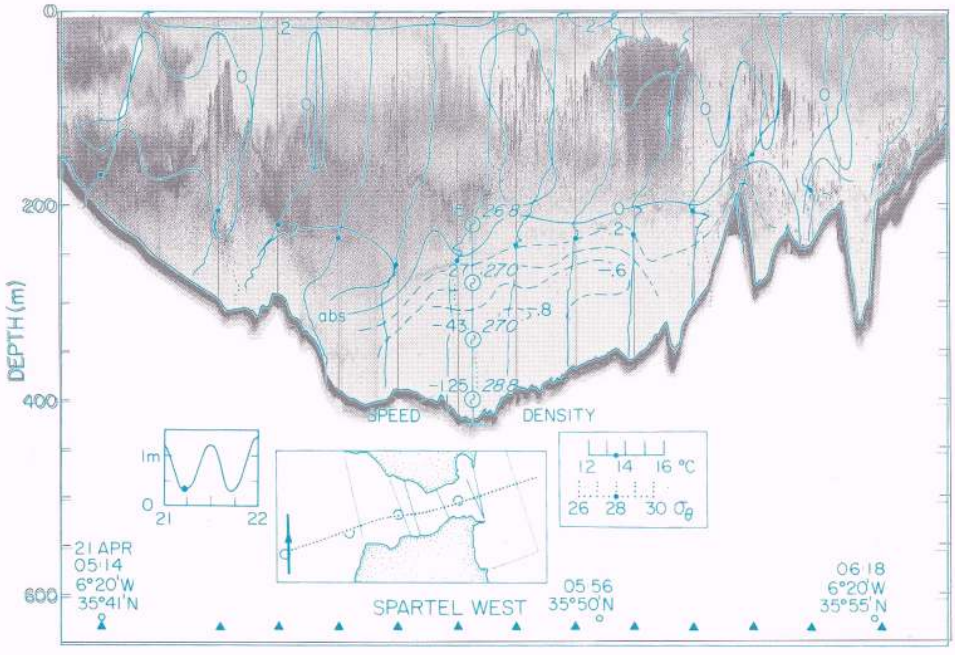


*Fig. 5.1.* A transect across Spartel West, showing the sloping interface separating the two layers.

*Overlay.* Temperature profiles (solid lines) and, less often, density profiles (dotted lines), together with contours of constant flow speed (along channel component) derived from Doppler data. Values on contours indicate flow speed in $ms^{-1}$.

SPARTEL WEST

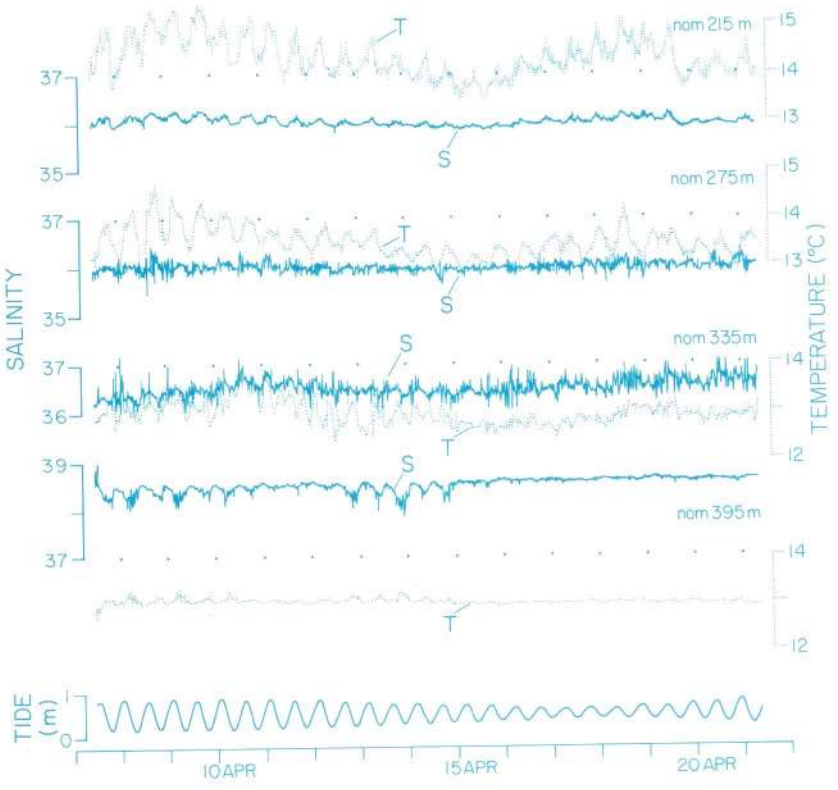

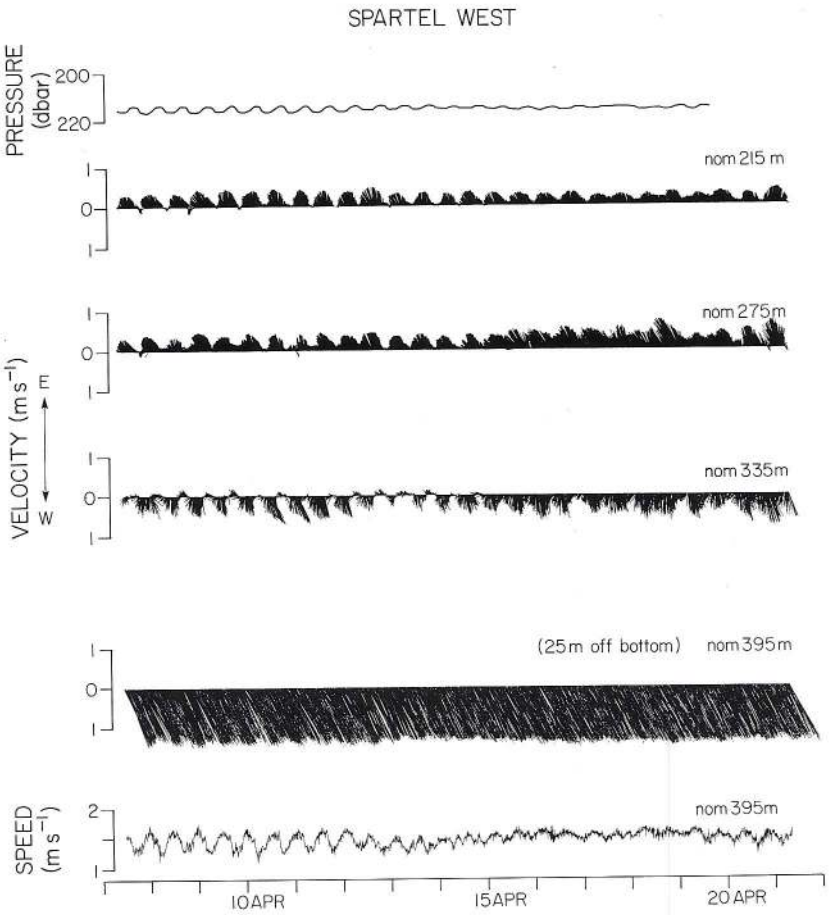


*Fig. 5.2.* Current vectors from four instruments over Spartel West, together with pressure at the uppermost and speed at the deepest current meter.
*Overlay.* Temperature (dotted line) and salinity (solid line) for each instrument, together with predicted tidal height.

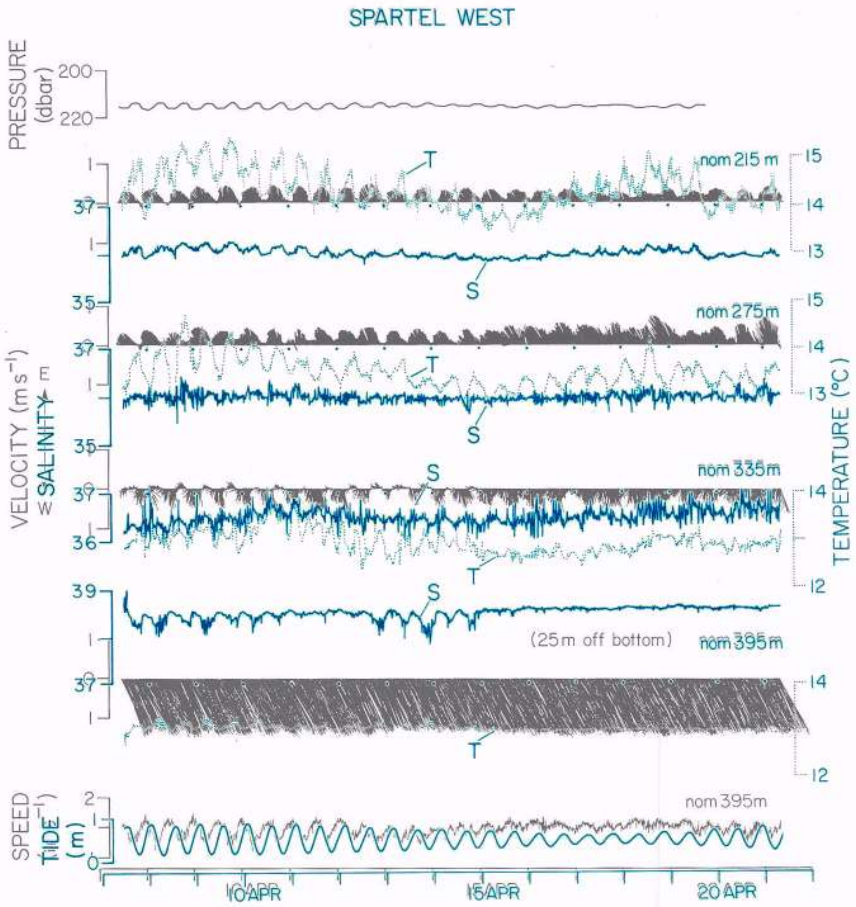


*Fig. 5.2.* Current vectors from four instruments over Spartel West, together with pressure at the uppermost and speed at the deepest current meter.
*Overlay.* Temperature (dotted line) and salinity (solid line) for each instrument, together with predicted tidal height.

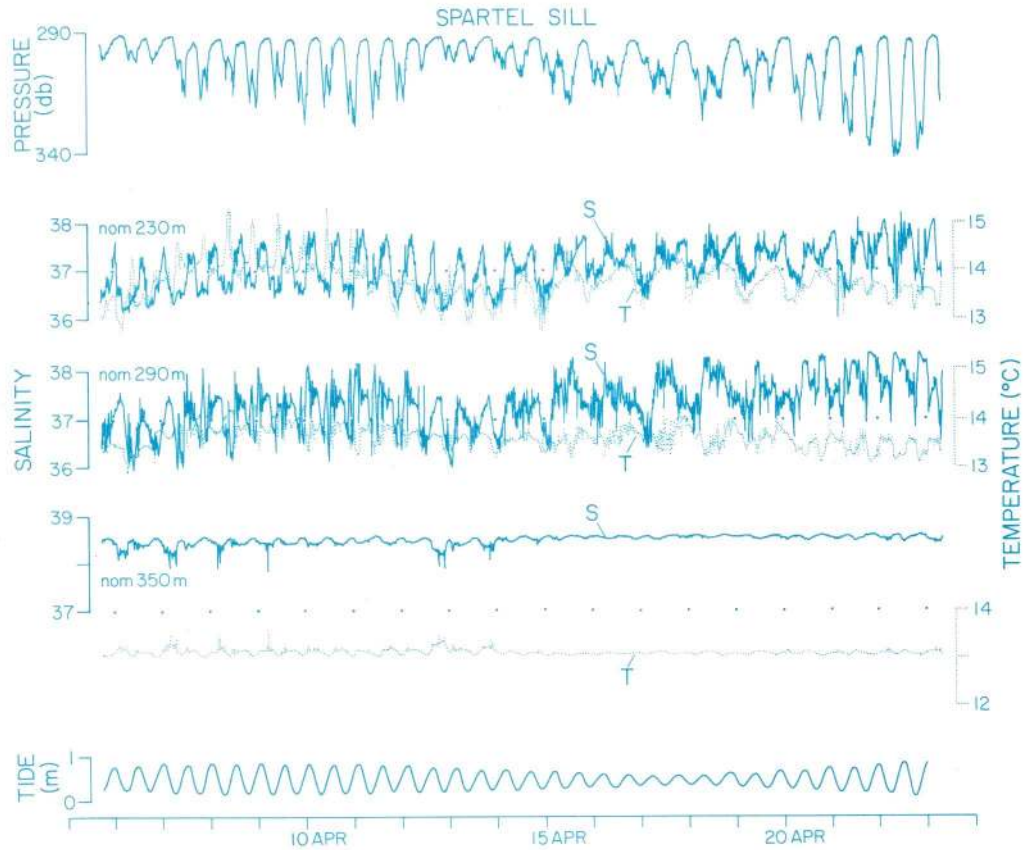
SPARTEL SILL
PRESSURE (db)
290
340
nom 230m
nom 290m
nom 350m
S
T
SALINITY
38
37
36
39
TEMPERATURE (°C)
15
14
13
12
TIDE (m)
1
0
10 APR
15 APR
20 APR

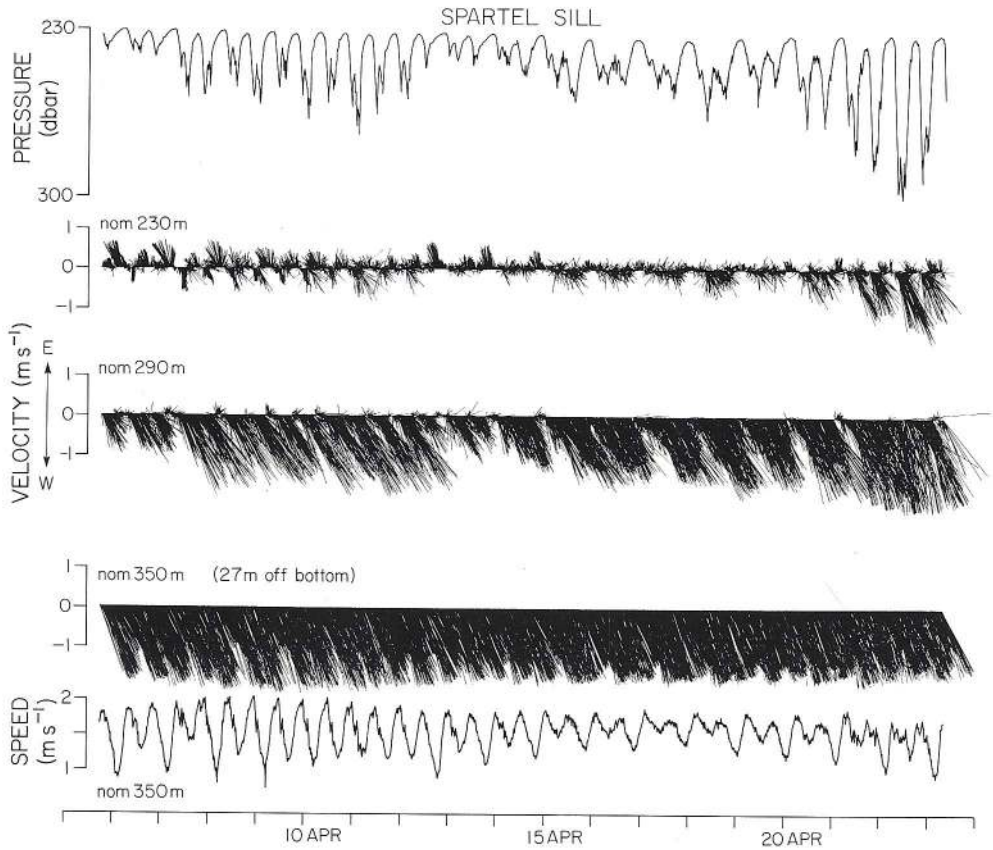


*Fig. 5.3.* Current vectors from three instruments over Spartel Sill, together with pressure at the uppermost and speed at the deepest current meter.
*Overlay.* Temperaure (dotted line) and salinity (solid line) for each instrument, together with predicted tidal height. The pressure time series at the middle instrument (nom. 290 m) is shown at top.

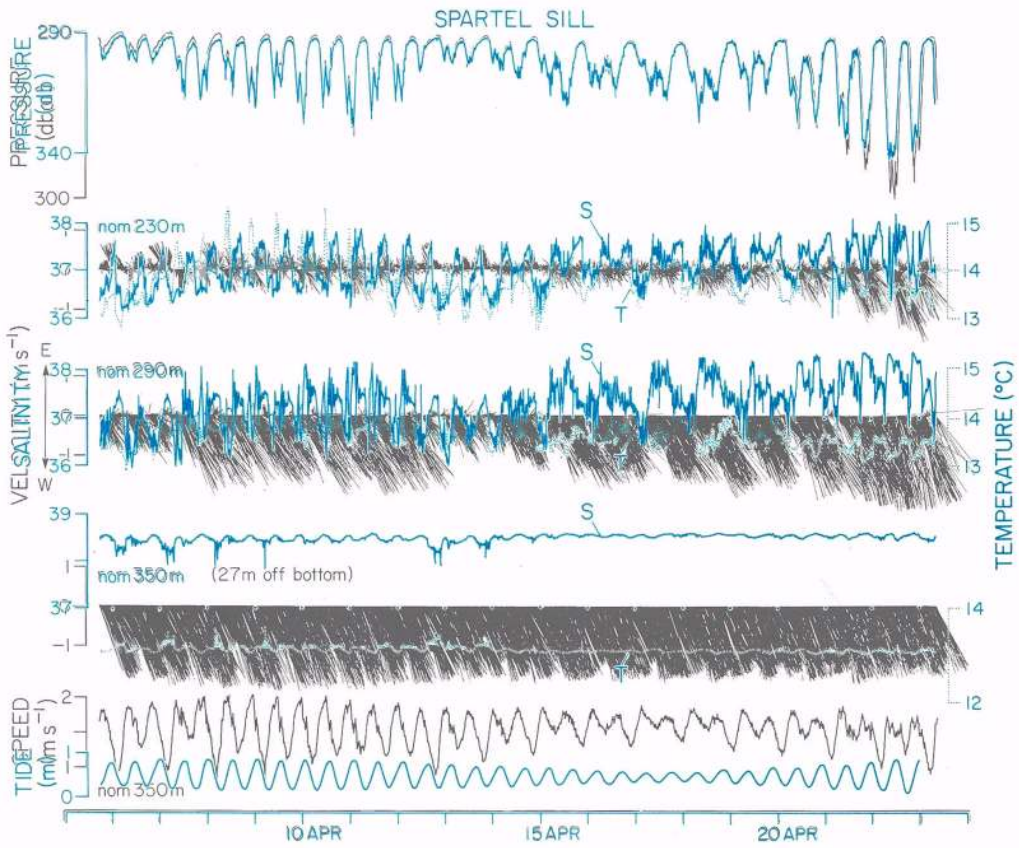


*Fig. 5.3.* Current vectors from three instruments over Spartel Sill, together with pressure at the uppermost and speed at the deepest current meter.

*Overlay.* Temperaure (dotted line) and salinity (solid line) for each instrument, together with predicted tidal height. The pressure time series at the middle instrument (nom. 290 m) is shown at top.

*Fig. 6.1.* Transect, looking west, across Tangier Basin, showing sloping interface. At this location the outflow is locally separated.
*Overlay.* Temperature (solid lines), density (dotted lines) and contours of along-channel component of flow (dashed lines). Values on contours indicate flow speed in $ms^{-1}$.

*Fig. 6.2.* Contours of constant density derived from time series of CTD profiles at Station 14.5W, showing large vertical excursions of the pycnocline. Isopycnals less than 27.0 have been excluded so as to simplify the figure.
*Overlay.* Doppler velocity profiles for the same period. Horizontal bar (1500-1700h) indicates period during which the small bore travels westward past the station, shown in detail in Fig. 12.9.

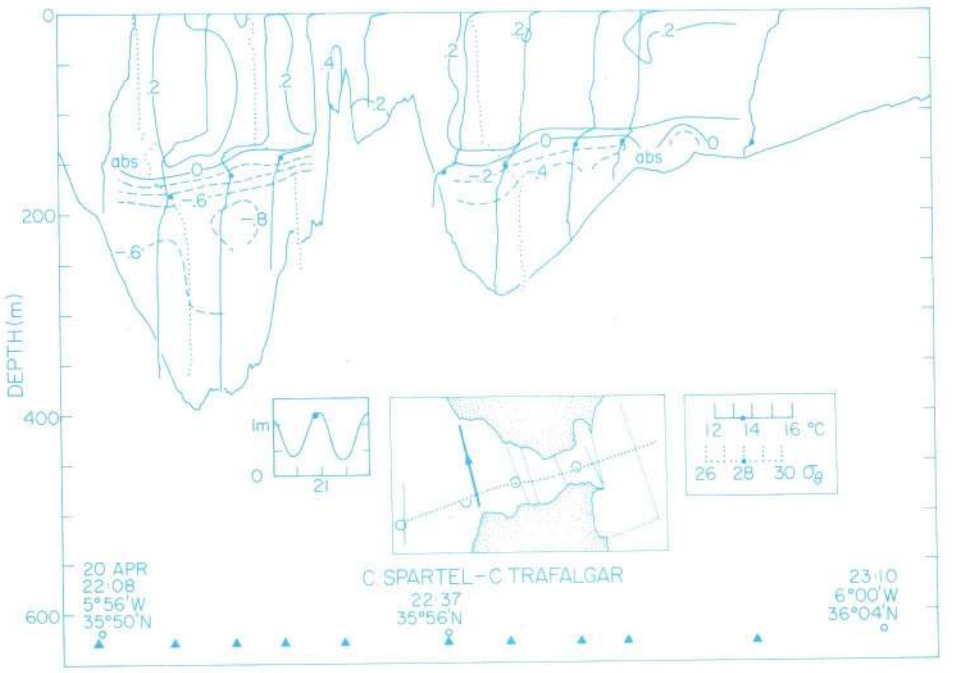
DEPTH (m)
0
200
400
600
abs
2
4
6
8
1m
0
21
12 14 16 °C
26 28 30 $\sigma_\theta$
20 APR
22:08
5°56'W
35°50'N
C. SPARTEL–C. TRAFALGAR
22:37
35°56'N
23:10
6°00'W
36°04'N

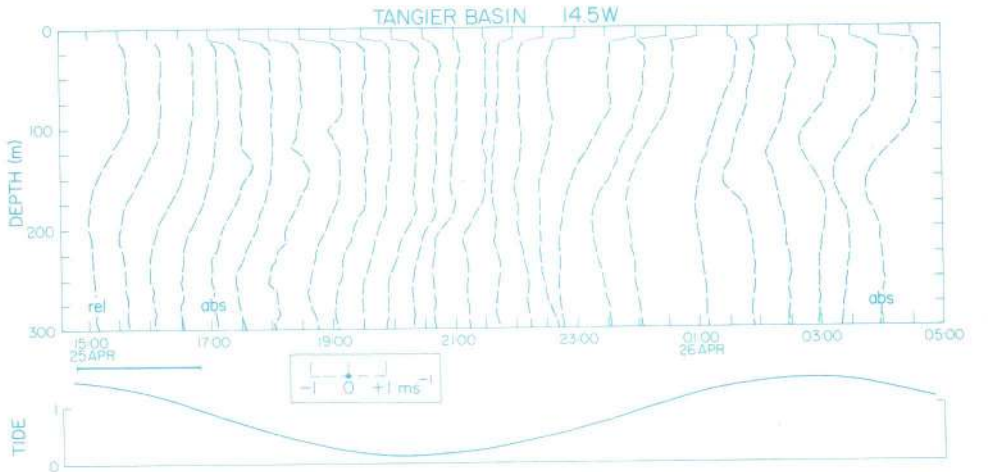
TANGIER BASIN 14.5W
DEPTH (m)
0
100
200
300
rel
abs
15:00
25 APR
17:00
19:00
21:00
23:00
01:00
26 APR
03:00
05:00
−1 0 +1 ms⁻¹
TIDE
1
0

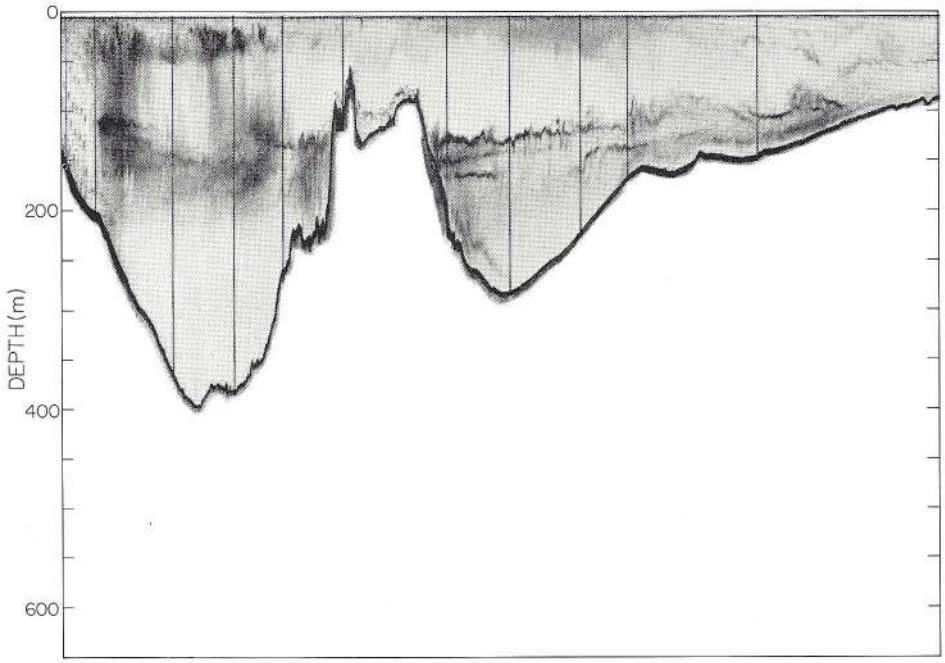
0
200
400
600
DEPTH (m)

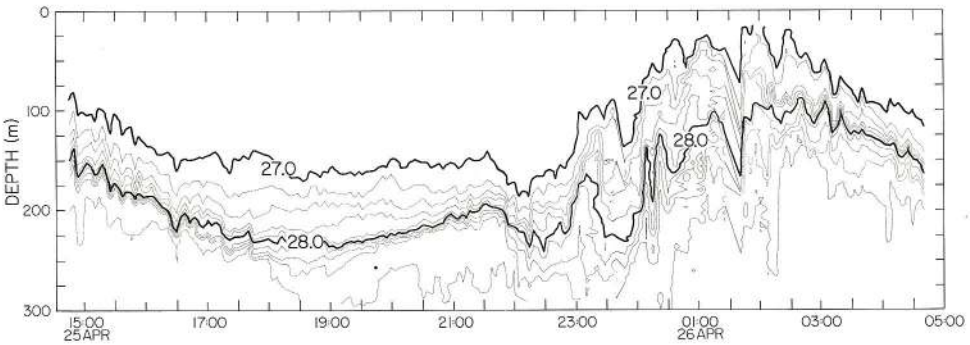
0
100
200
300
DEPTH (m)
27.0
28.0
27.0
28.0
15·00
25 APR
17·00
19·00
21·00
23·00
01·00
26 APR
03·00
05·00

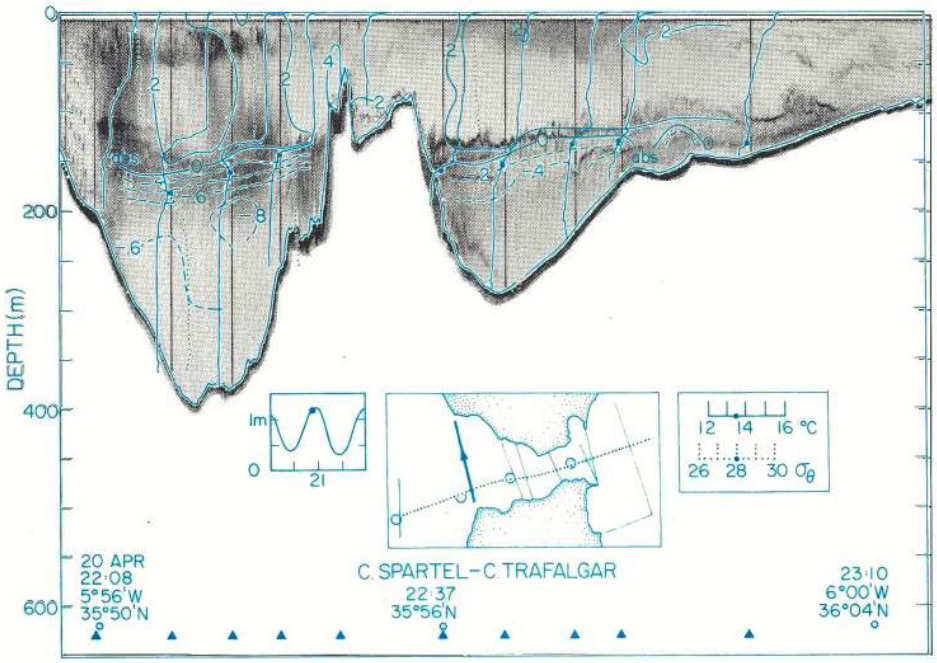
DEPTH (m)
0
200
400
600
abs
abs
1m
0
21
12 14 16 °C
26 28 30 $\sigma_\theta$
20 APR
22:08
5°56'W
35°50'N
C. SPARTEL–C. TRAFALGAR
22:37
35°56'N
23:10
6°00'W
36°04'N

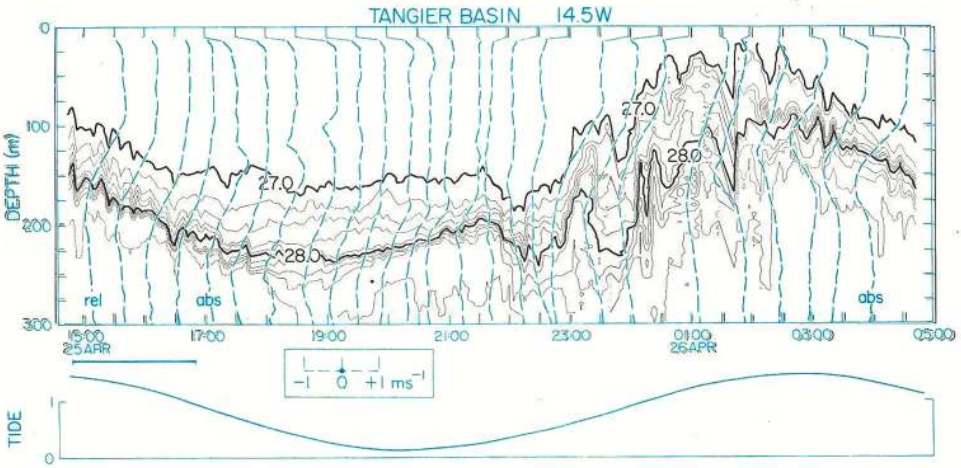
TANGIER BASIN 14.5W
DEPTH (m)
0
100
200
300
27.0
28.0
27.0
28.0
rel
abs
abs
15:00
25 APR
17:00
19:00
21:00
23:00
01:00
26 APR
03:00
05:00
−1 0 +1 ms⁻¹
TIDE
1
0

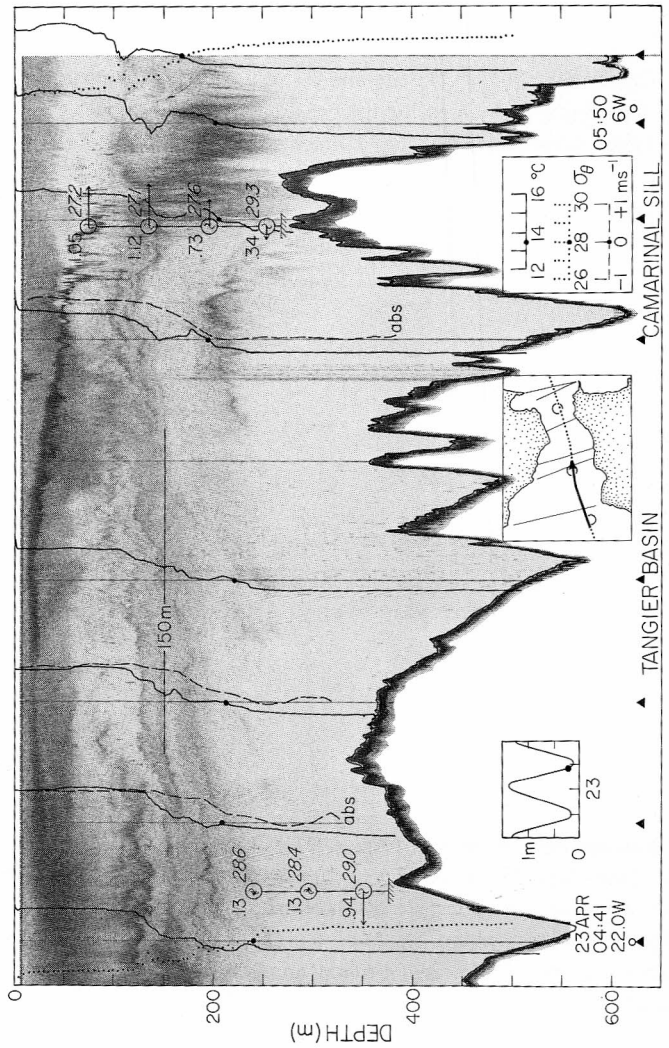
DEPTH (m)
0
200
400
600
23 APR
04·41
22·0W
.13 286
.13 284
.94 290
150m
abs
1m
0
23
TANGIER BASIN
CAMARINAL SILL
05·50
6W
12 14 16 °C
26 28 30 $\sigma_\theta$
−1 0 +1 ms$^{-1}$
.99 272
1.12 277
.73 276
.34 293
abs

*Fig. 7.1.* Transect at Camarinal Sill. The detailed structure of the internal response is sensitive to the bottom topography, which is highly irregular at this location.
*Overlay.* Temperature (solid lines), density (dotted lines) and contours of constant along-axis velocity (dashed lines).

*Fig. 7.2.* Contours of constant density derived from a CTD time series at station 7W over the crest of Camarinal Sill. Isopycnals less than 27.0 and greater than 29.0 have been excluded to simplify the presentation and make the interface displacement more clearly visible.
*Overlay.* Doppler velocity profiles (along channel component, dashed lines) and moored current meter measurements (arrows). Internal Froude numbers of the upper layer ($F_1^2$) and lower layer ($F_2^2$) are shown above.

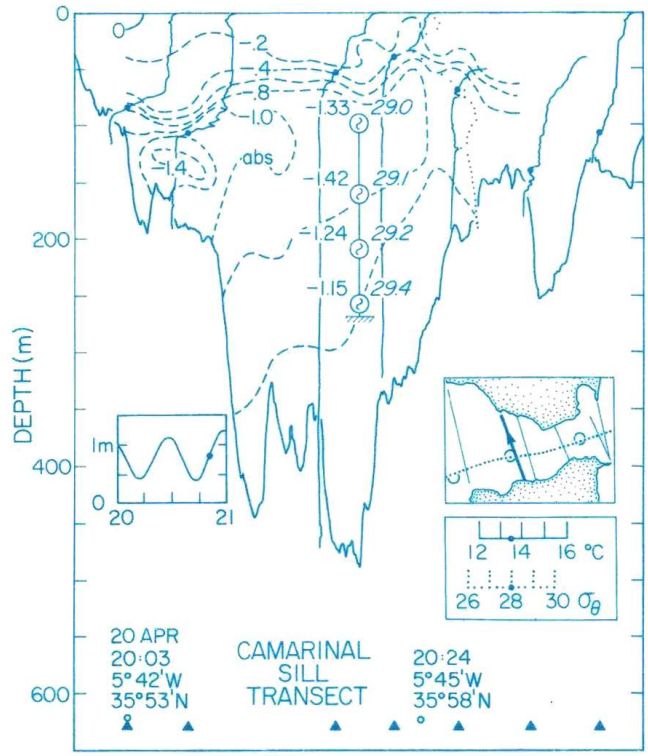
DEPTH (m)
0
200
400
600
-2
-4
-8
-1.0
-1.4
abs
-1.33
29.0
-1.42
29.1
-1.24
29.2
-1.15
29.4
1m
0
20
21
12 14 16 °C
26 28 30 $\sigma_\theta$
20 APR
20:03
5°42'W
35°53'N
CAMARINAL
SILL
TRANSECT
20:24
5°45'W
35°58'N

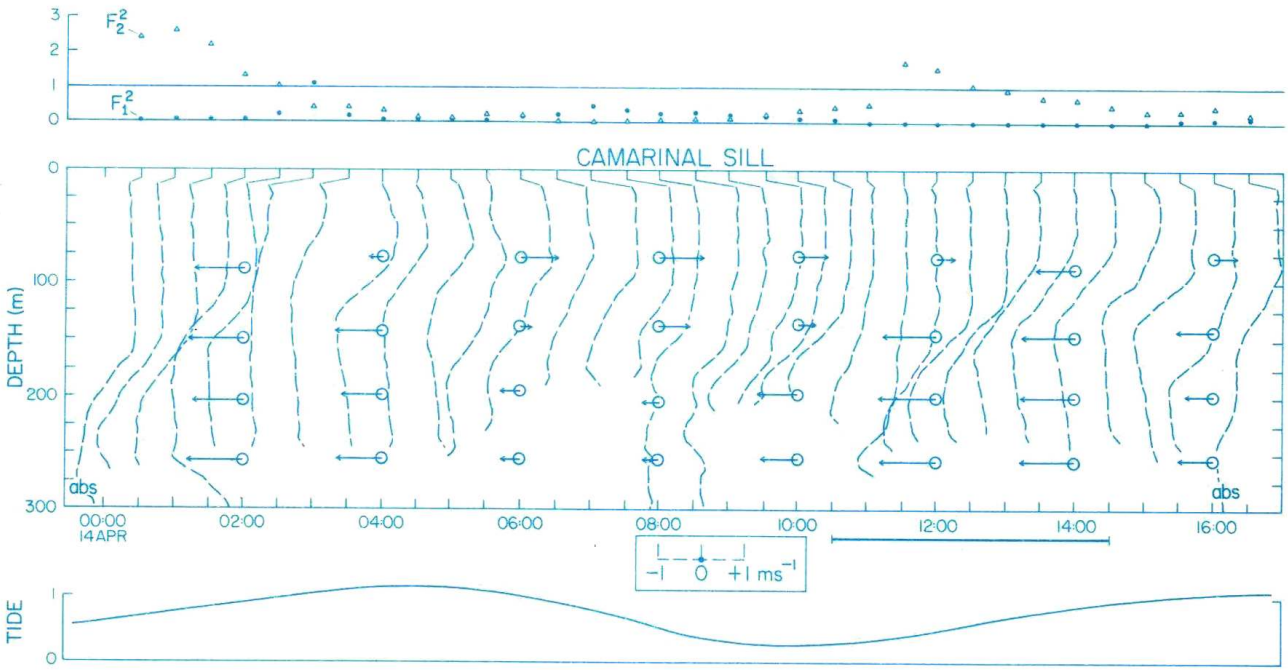
$F_2^2$
$F_1^2$
CAMARINAL SILL
DEPTH (m)
abs
abs
00:00
14 APR
02:00
04:00
06:00
08:00
10:00
12:00
14:00
16:00
−1 0 +1 ms$^{-1}$
TIDE

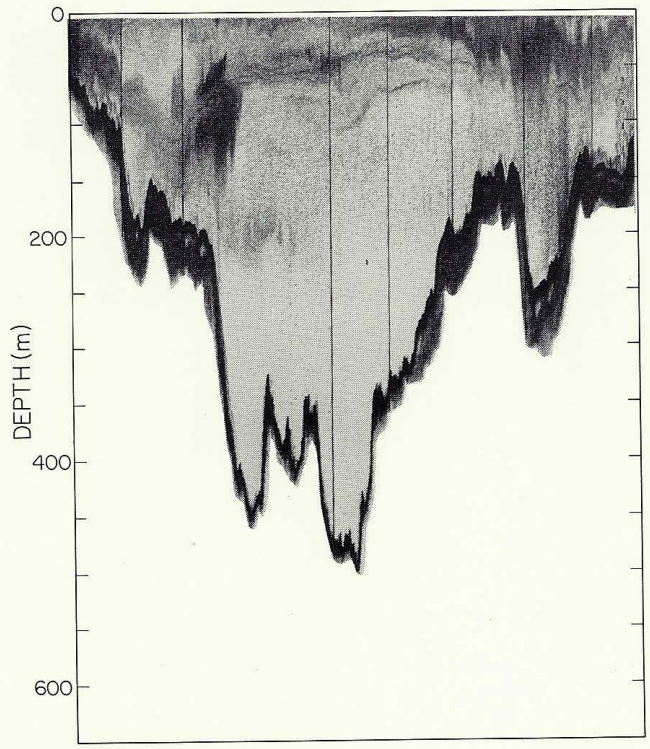
0
200
400
600
DEPTH (m)

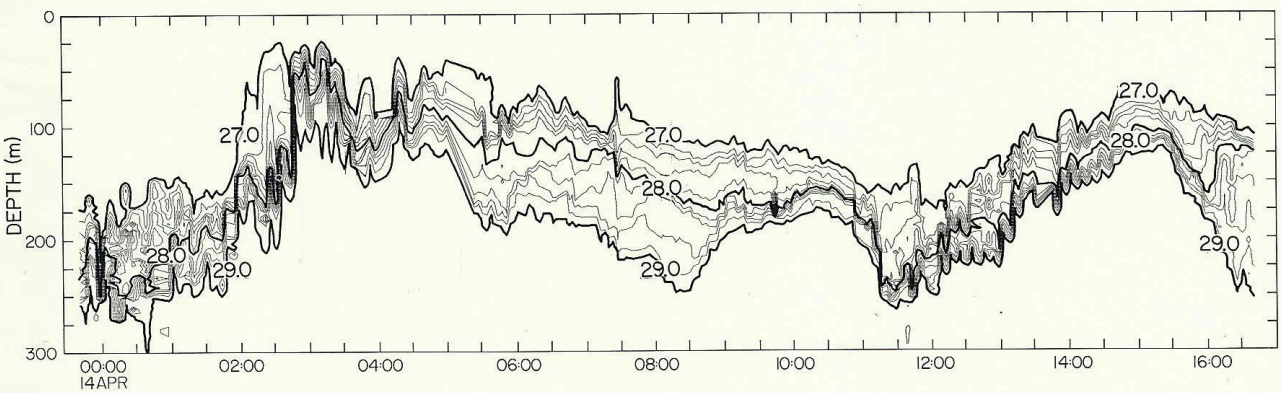
0
100
200
300
DEPTH (m)
27.0
28.0
29.0
00:00
14 APR
02:00
04:00
06:00
08:00
10:00
12:00
14:00
16:00

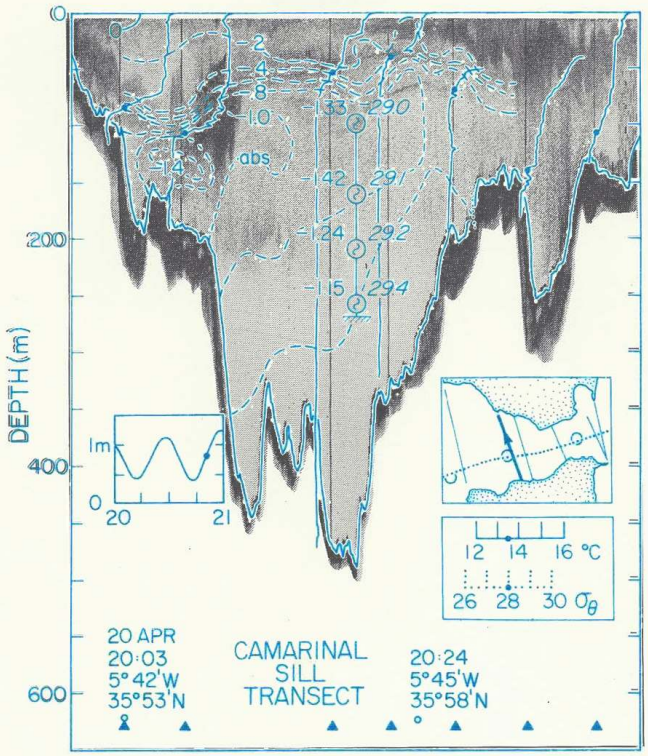
DEPTH (m)
0
200
400
600
abs
1.33
290
1.42
291
1.24
292
1.15
294
1m
0
20
21
12 14 16 °C
26 28 30 σθ
20 APR
20:03
5°42'W
35°53'N
CAMARINAL
SILL
TRANSECT
20:24
5°45'W
35°58'N

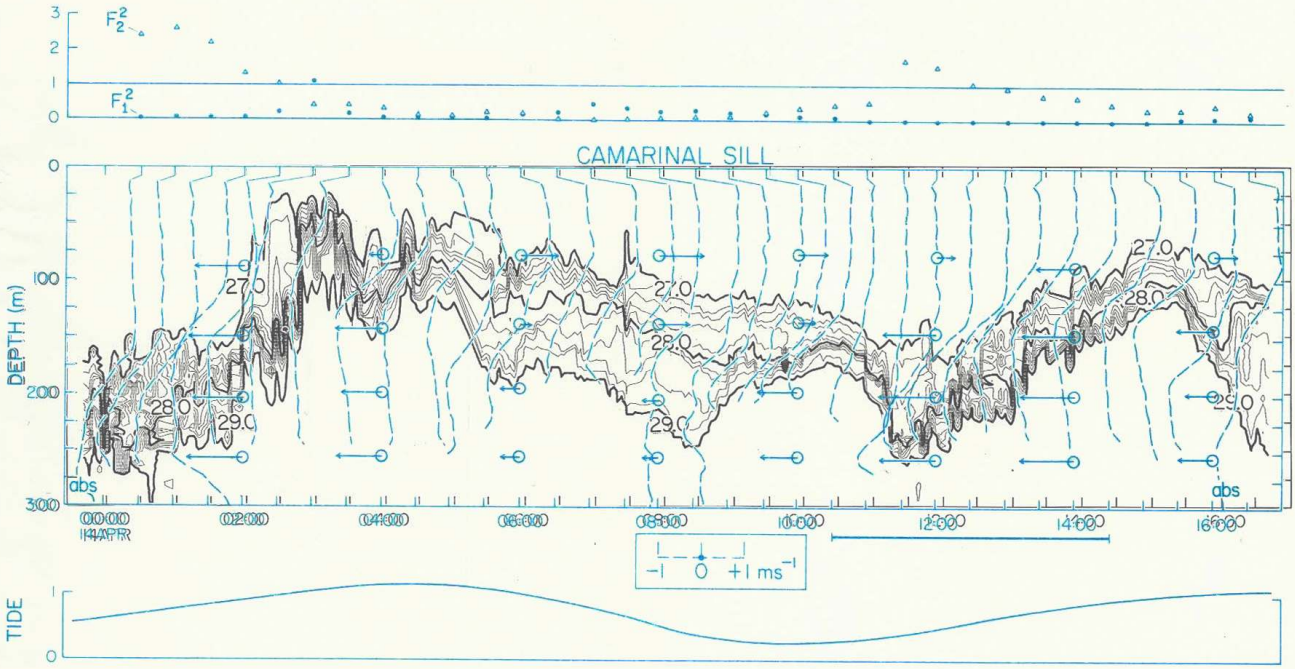
F2²
F1²
CAMARINAL SILL
DEPTH (m)
27.0
28.0
29.0
abs
14 APR
−1 0 +1 ms⁻¹
TIDE

CAMARINAL SILL

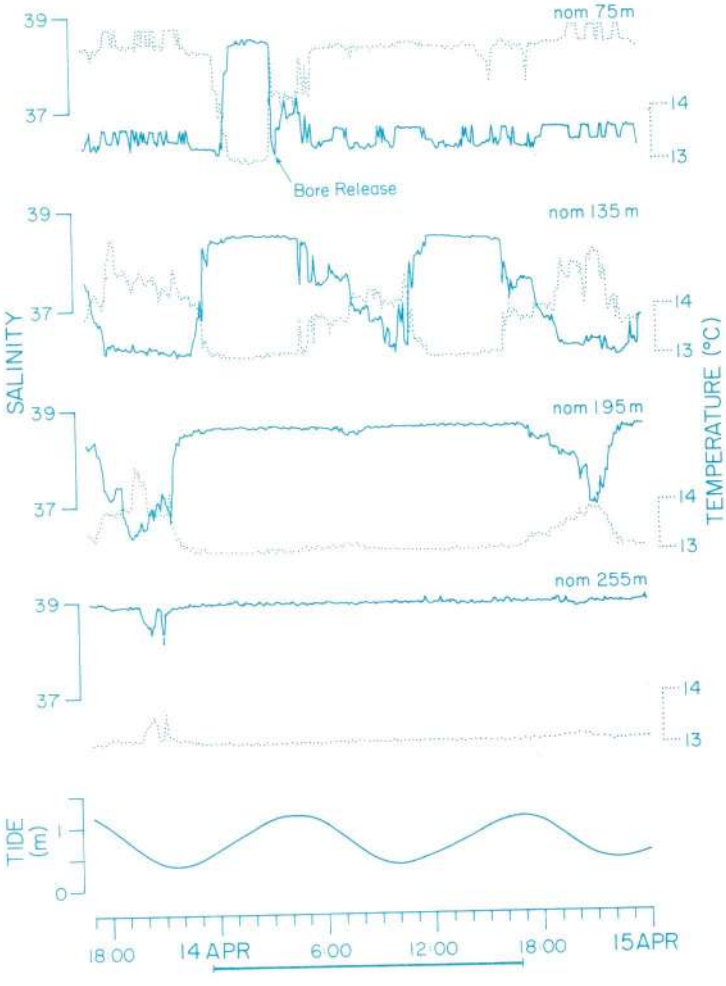

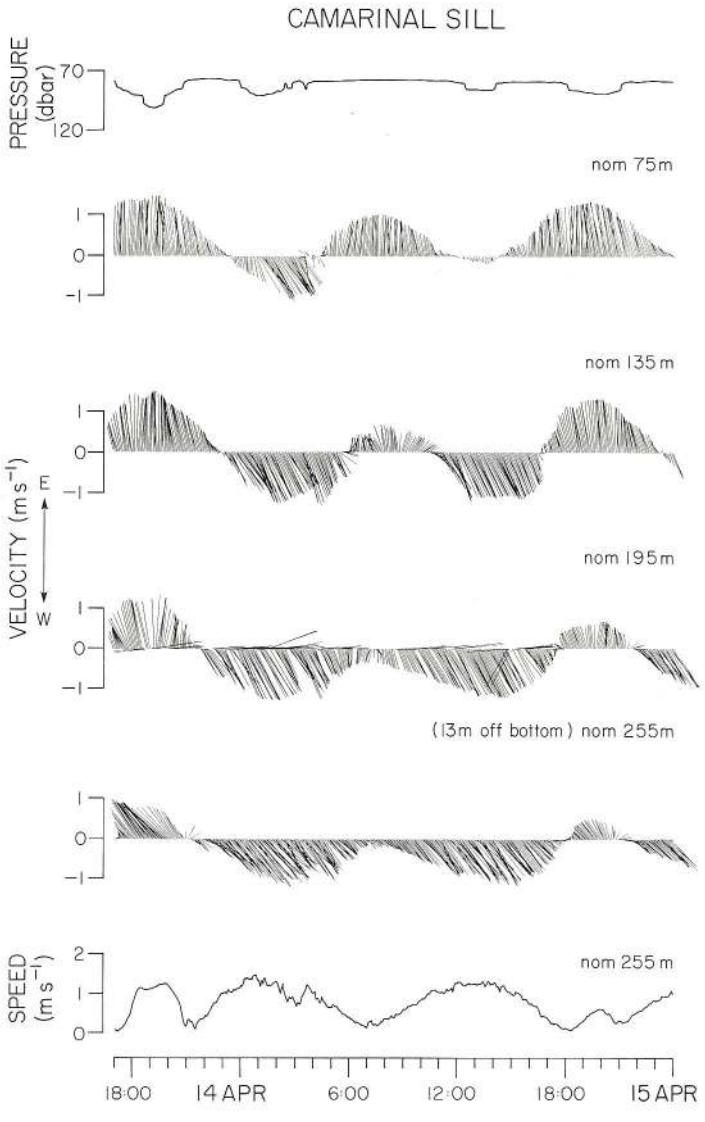


*Fig. 7.3.* Current vectors from four instruments over Camarinal Sill, together with pressure at the uppermost and speed at the deepest current meter.
*Overlay.* Temperature (dotted lines) and salinity (solid lines) time series for each instrument, together with predicted tidal height. The horizontal line (14 April 0000 - 1600h) corresponds to the period covered by the time series CTD data shown in Fig. 7.2.

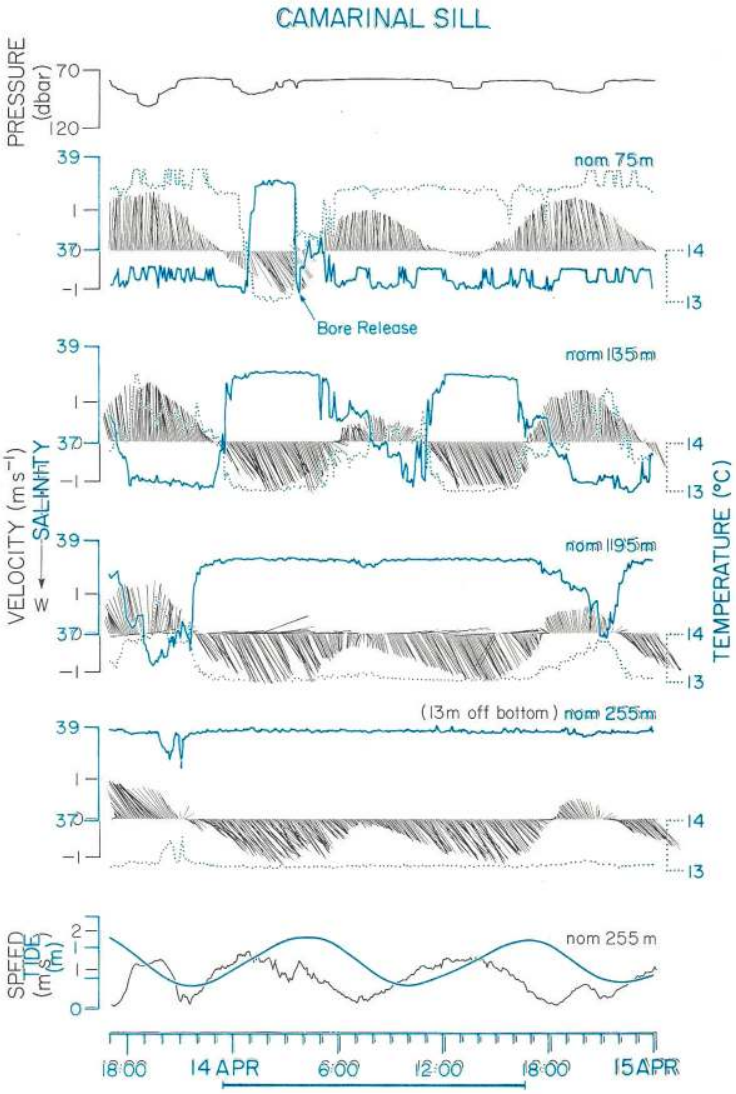


*Fig. 7.3.* Current vectors from four instruments over Camarinal Sill, together with pressure at the uppermost and speed at the deepest current meter.

*Overlay.* Temperature (dotted lines) and salinity (solid lines) time series for each instrument, together with predicted tidal height. The horizontal line (14 April 0000 - 1600h) corresponds to the period covered by the time series CTD data shown in Fig. 7.2.

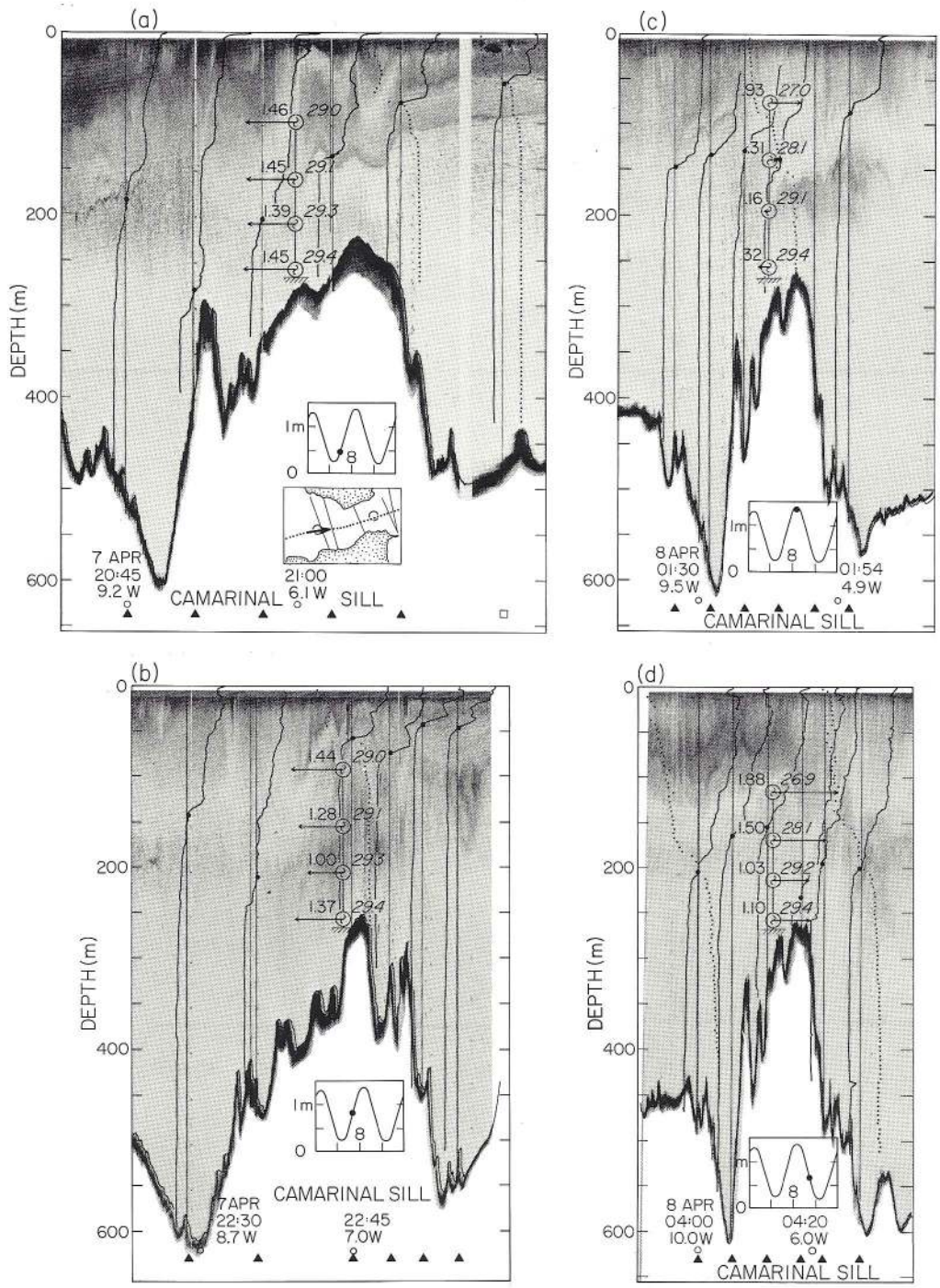


*Fig. 7.4a-h.* A sequence of runs across Camarinal Sill with temperature profiles (solid lines), density (dotted lines) and recording current meter speeds (horizontal arrows) and densities. The times of each run are indicated by solid triangles along the time axis of Fig. 7.5.

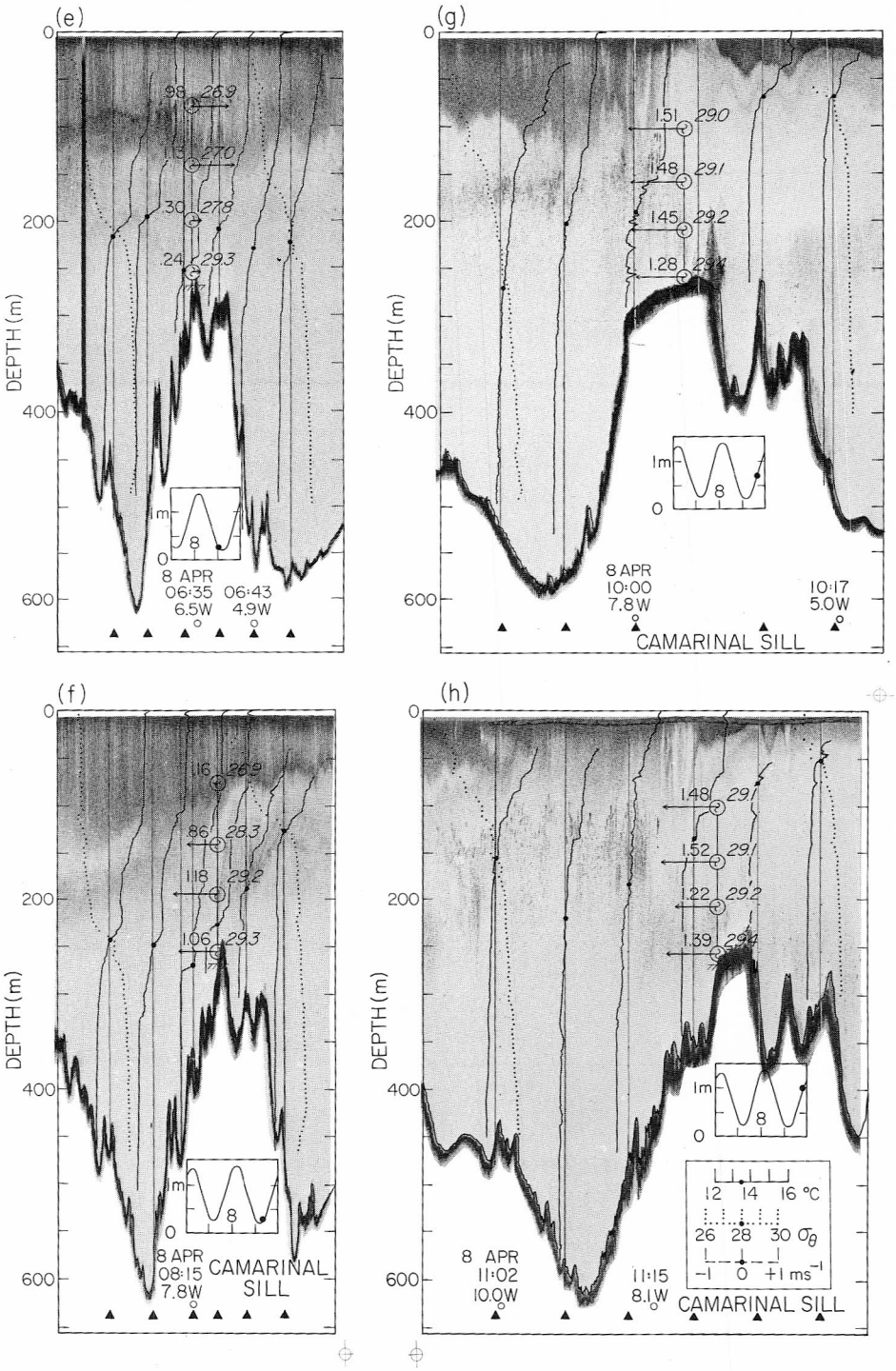
(e)
0
200
400
600
DEPTH (m)
.98 26.9
1.13 27.0
.30 27.8
.24 29.3
1m
0
8
8 APR
06:35 06:43
6.5W 4.9W
(g)
1.51 29.0
1.48 29.1
1.45 29.2
1.28 29.4
1m
0
8
8 APR
10:00
7.8W
10:17
5.0W
CAMARINAL SILL
(f)
.16 26.9
.86 28.3
1.18 29.2
1.06 29.3
1m
0
8
8 APR
08:15
7.8W
CAMARINAL SILL
(h)
1.48 29.1
1.52 29.1
1.22 29.2
1.39 29.2
1m
0
8
12 14 16 °C
26 28 30 σθ
−1 0 +1 ms−1
8 APR
11:02
10.0W
11:15
8.1W
CAMARINAL SILL

# CAMARINAL SILL

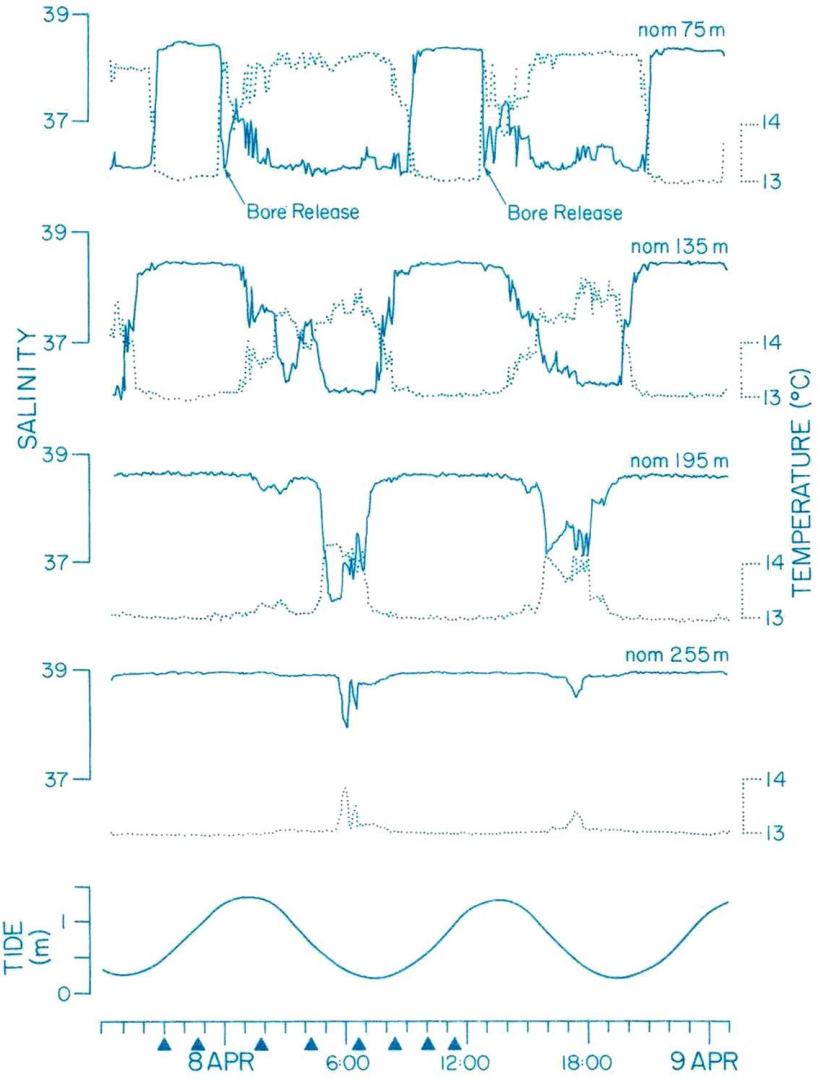

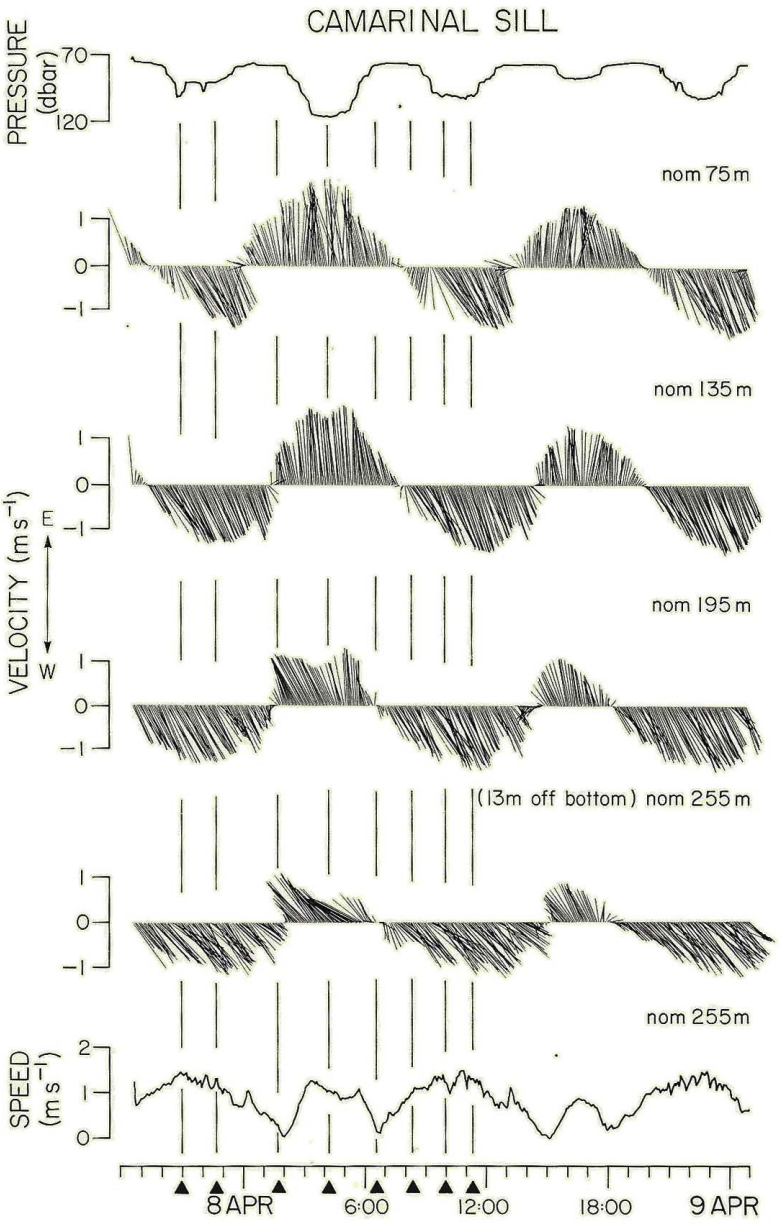


*Fig 7.5.* Current vectors from four instruments over Camarinal Sill, together with pressure at the uppermost and speed at the deepest current meter.
*Overlay.* Temperature (dotted lines) and salinity (solid lines) time series for each instrument, together with predicted tidal height. The solid triangles along the time axis show times of successive runs across the sill presented in Fig. 7.4. The time of release of the bore is shown on the 75m time series.

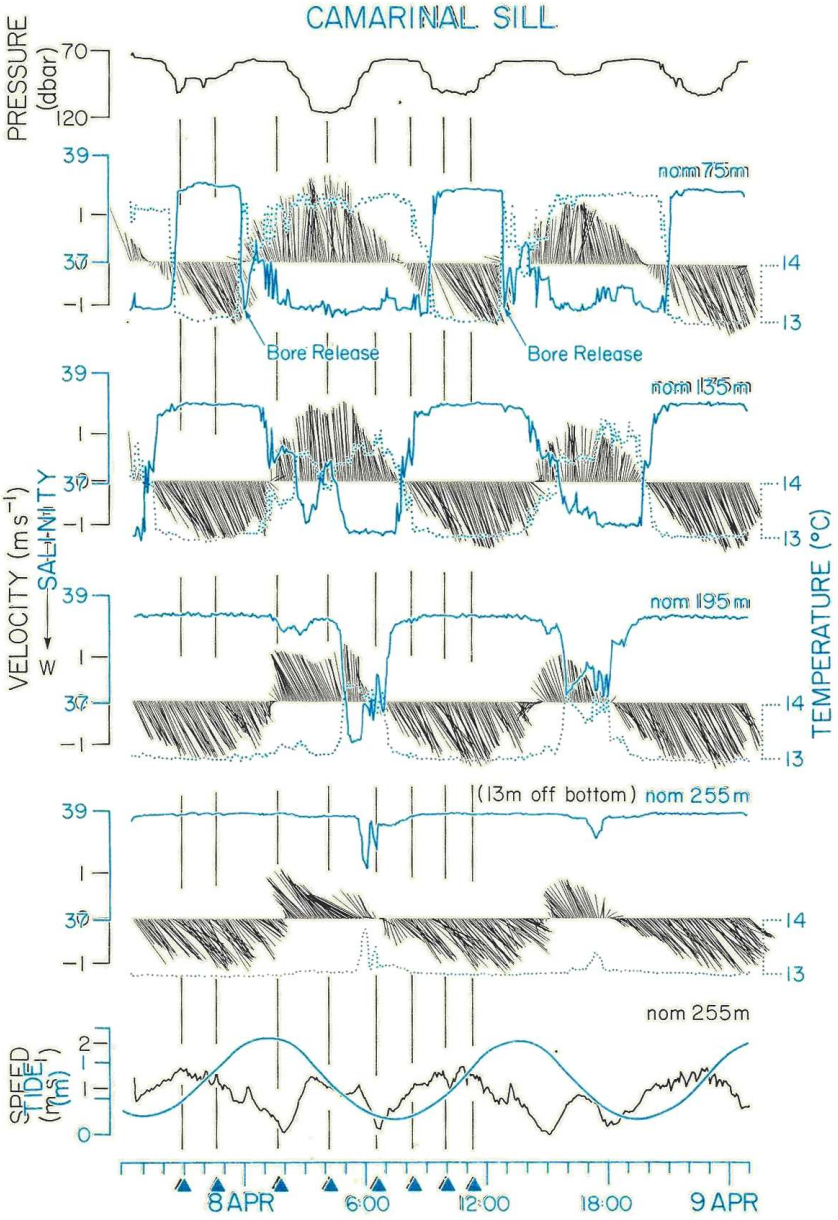


*Fig 7.5.* Current vectors from four instruments over Camarinal Sill, together with pressure at the uppermost and speed at the deepest current meter.

*Overlay.* Temperature (dotted lines) and salinity (solid lines) time series for each instrument, together with predicted tidal height. The solid triangles along the time axis show times of successive runs across the sill presented in Fig. 7.4. The time of release of the bore is shown on the 75m time series.

CAMARINAL SILL

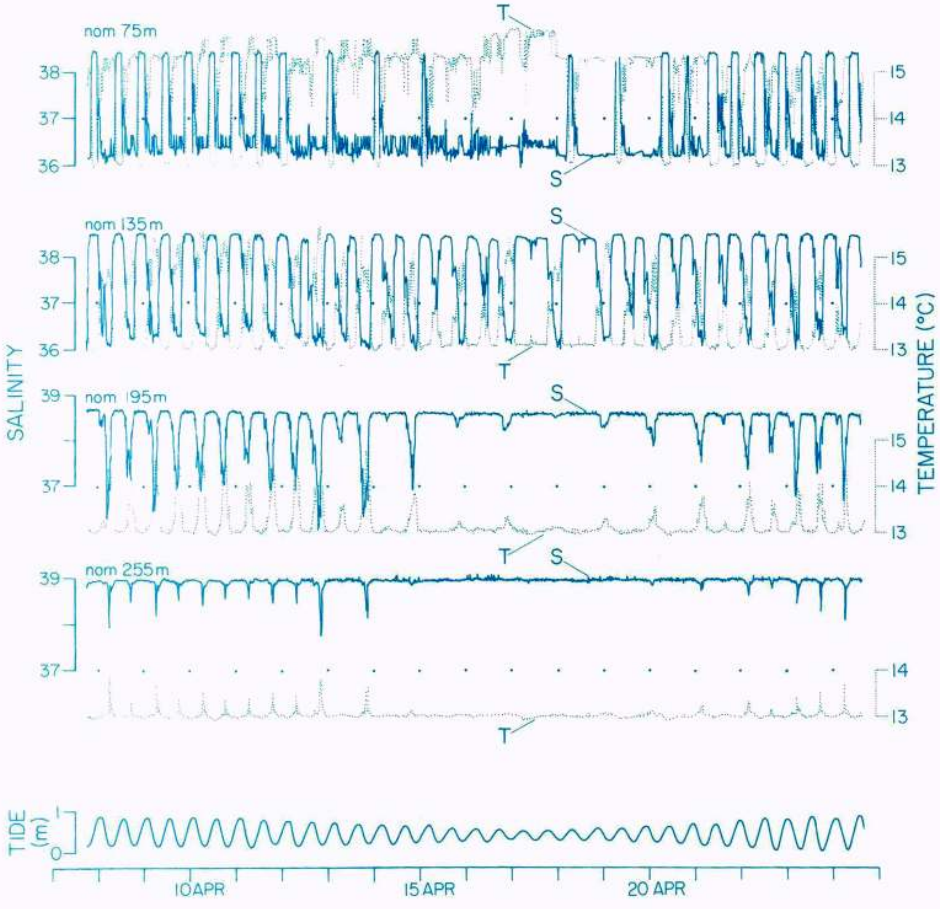

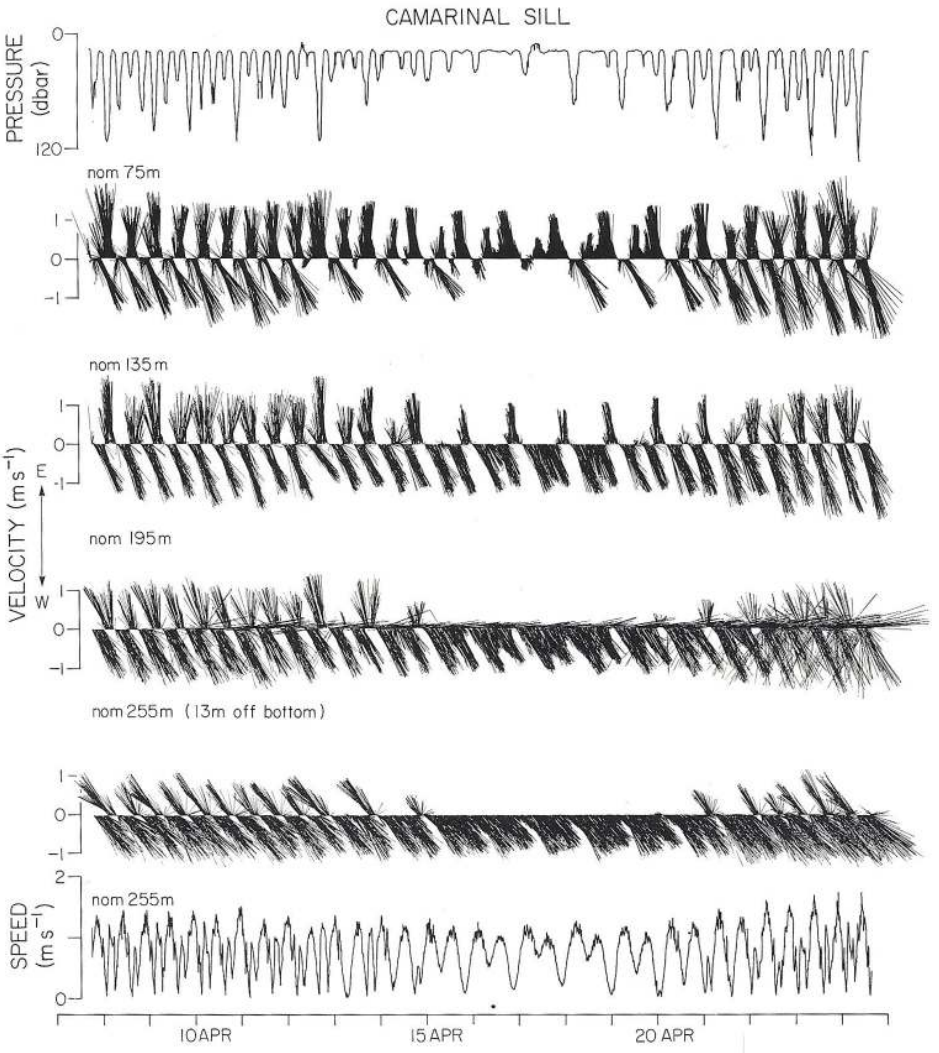


*Fig. 7.6.* Current vectors from four instruments over Camarinal Sill, together with pressure at the uppermost and speed at the deepest current meter.
*Overlay.* Temperature (dotted lines) and salinity (solid lines) time series for each instrument, together with predicted tidal height.

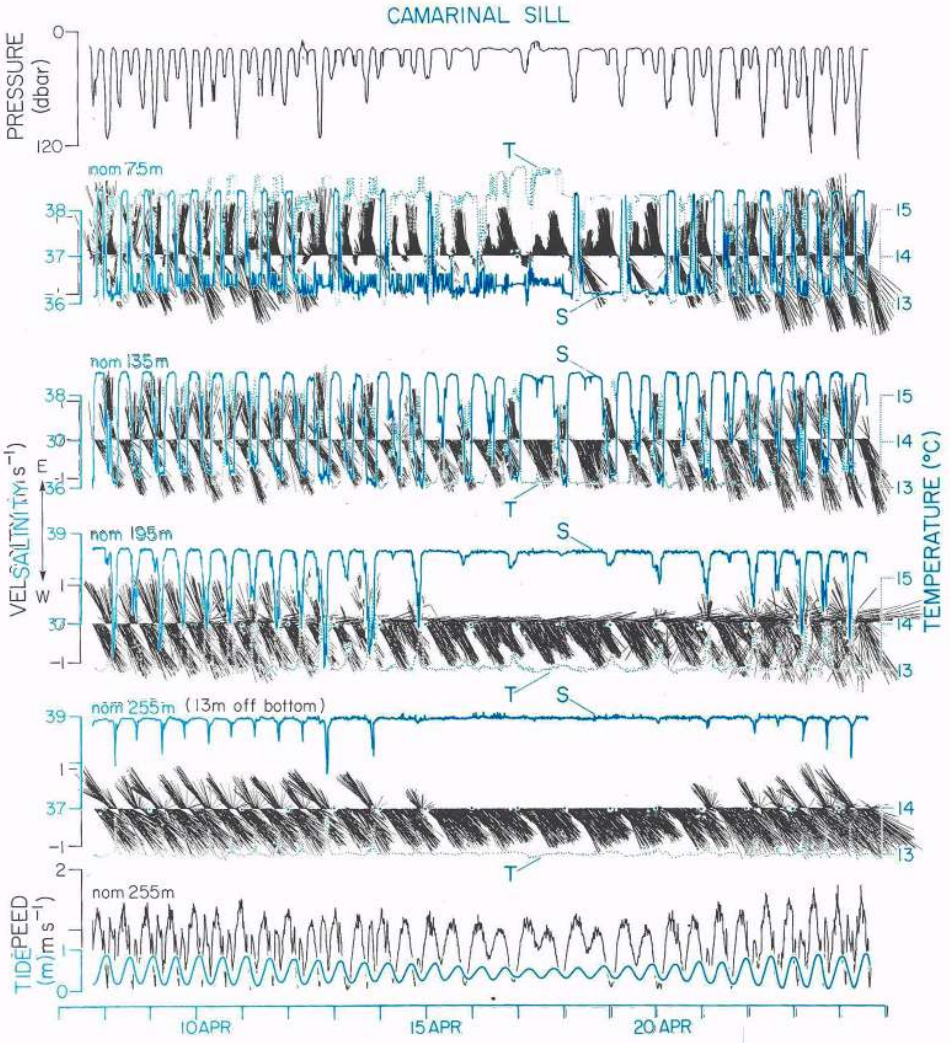


*Fig. 7.6.* Current vectors from four instruments over Camarinal Sill, together with pressure at the uppermost and speed at the deepest current meter.
*Overlay.* Temperature (dotted lines) and salinity (solid lines) time series for each instrument, together with predicted tidal height.

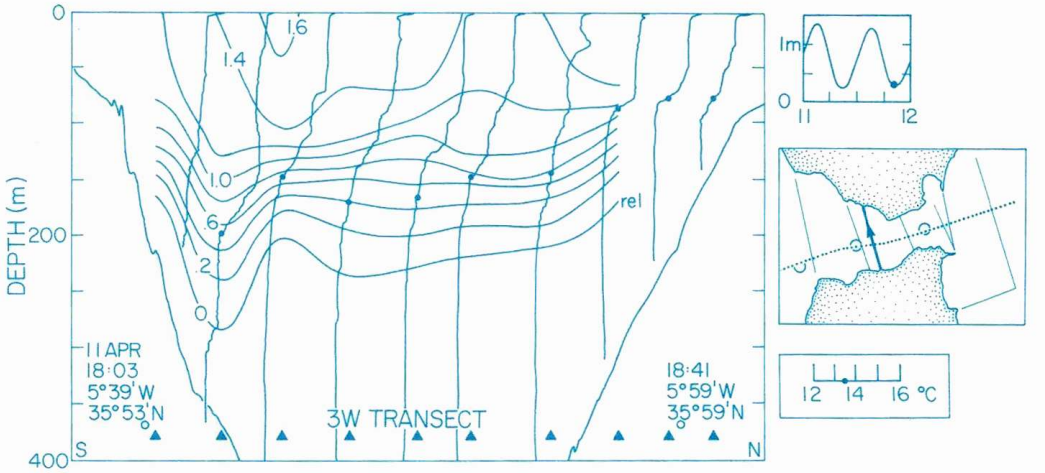
DEPTH (m)
0
200
400
1.6
1.4
1.0
.6
.2
0
rel
11 APR
18:03
5°39'W
35°53'N
3W TRANSECT
18:41
5°59'W
35°59'N
S
N
Im
0
11
12
12 14 16 °C

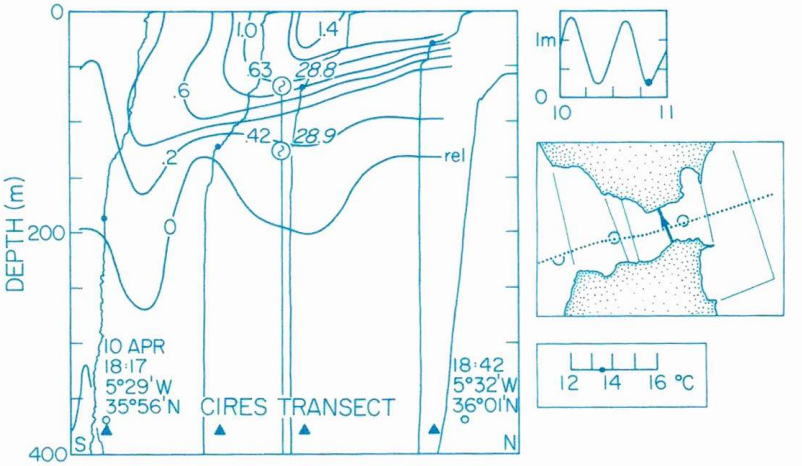
DEPTH (m)
0
200
400
1.0
1.4
.63
≤28.8
.6
.42
28.9
.2
0
rel
10 APR
18:17
5°29'W
35°56'N
CIRES TRANSECT
18:42
5°32'W
36°01'N
S
N
Im
0
10
11
12 14 16 °C

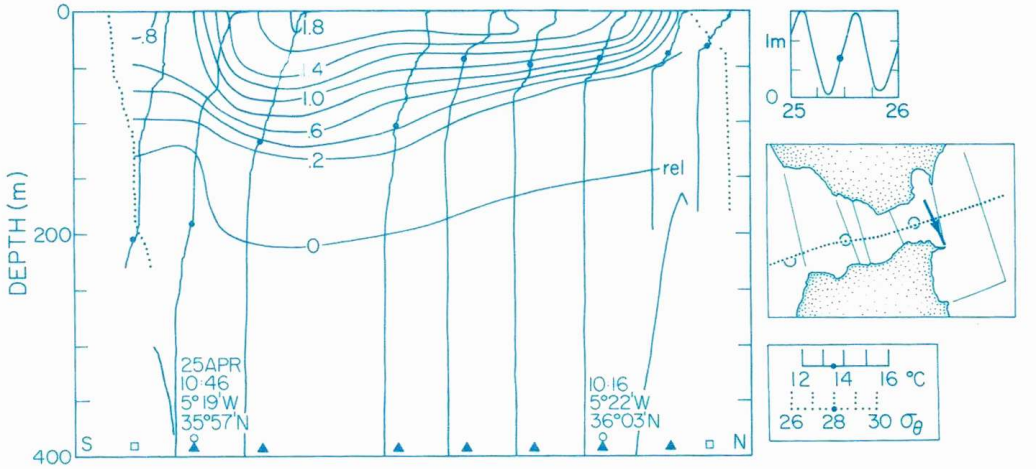
DEPTH (m)
0
200
400
-.8
1.8
1.4
1.0
.6
.2
0
rel
25APR
10:46
5°19'W
35°57'N
10:16
5°22'W
36°03'N
S
N
Im
0
25
26
12 14 16 °C
26 28 30 σθ

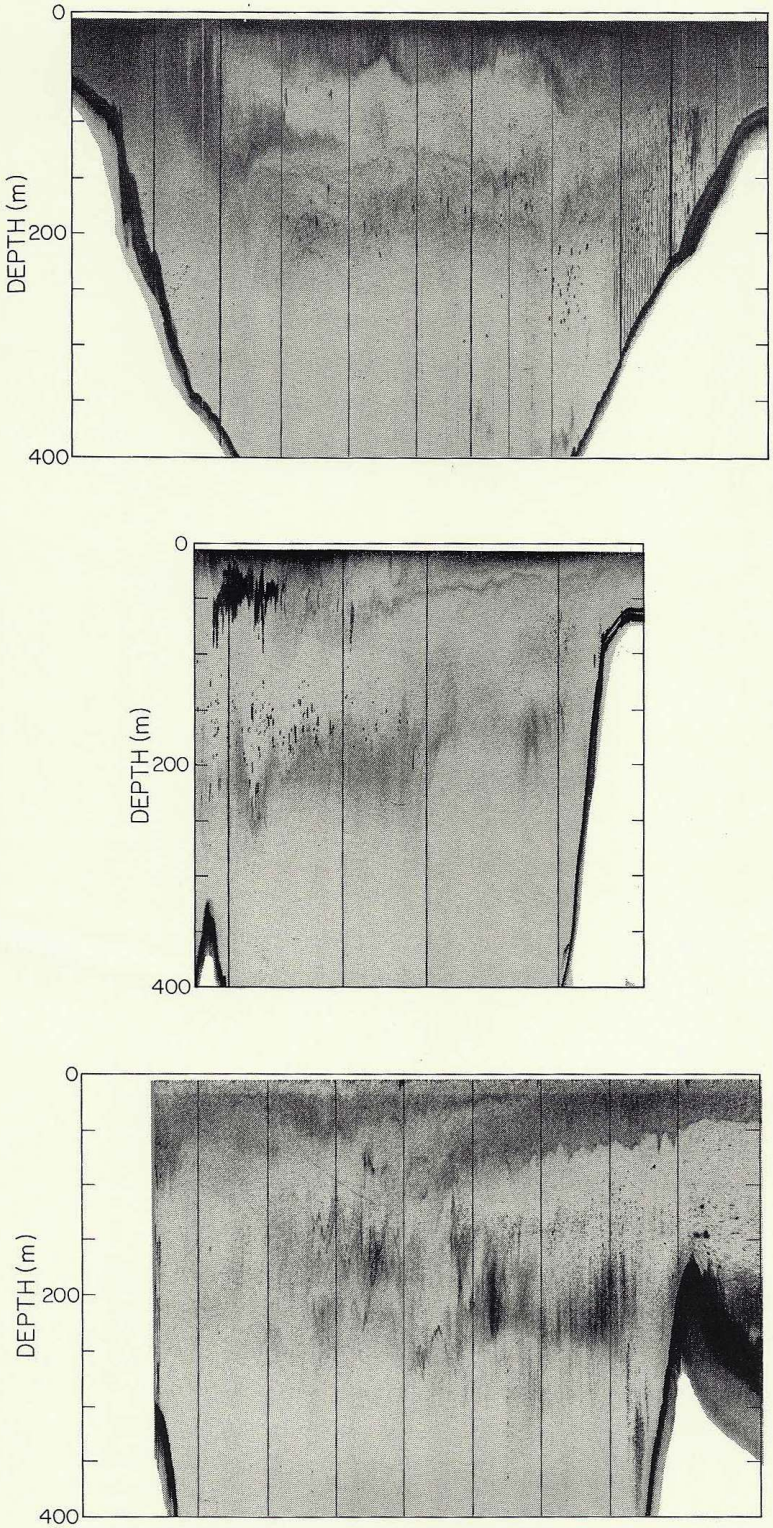


*Fig. 8.1a,b,c.* Transects, looking east, in Tarifa Narrows across 3W, 5E and 13.5E. *Overlay.* Temperature (solid lines), density (dotted lines) and contours of along-channel component of flow in $ms^{-1}$. For the Cires transect (5E) the Tarifa Narrows (9E) current meter data is included for reference. Note that 8.1c was obtained with a southward transect, but the image has been inverted for consistency with the preceding figures.

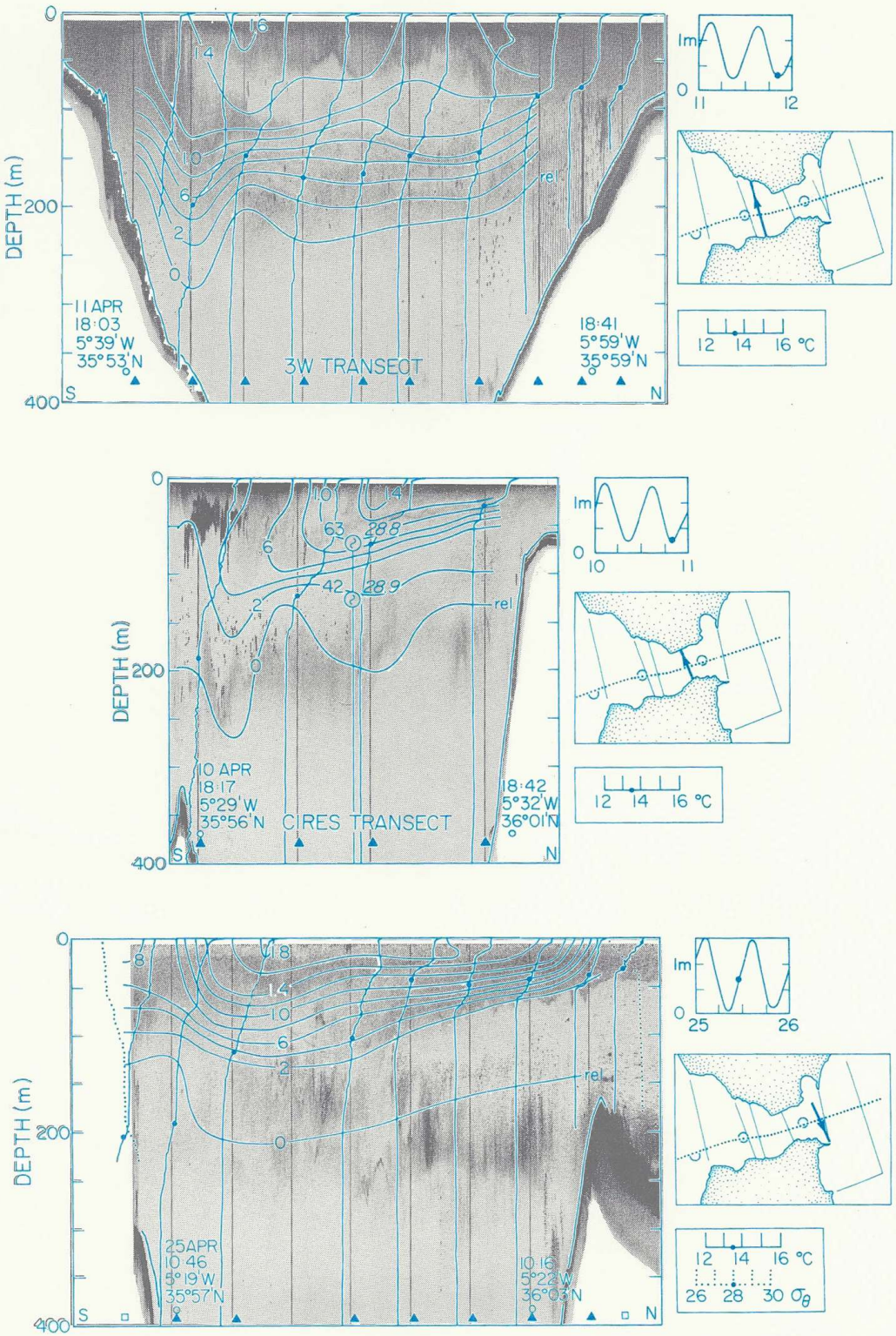


*Fig. 8.1a,b,c.* Transects, looking east, in Tarifa Narrows across 3W, 5E and 13.5E. *Overlay.* Temperature (solid lines), density (dotted lines) and contours of along-channel component of flow in $ms^{-1}$. For the Cires transect (5E) the Tarifa Narrows (9E) current meter data is included for reference. Note that 8.1c was obtained with a southward transect, but the image has been inverted for consistency with the preceding figures.

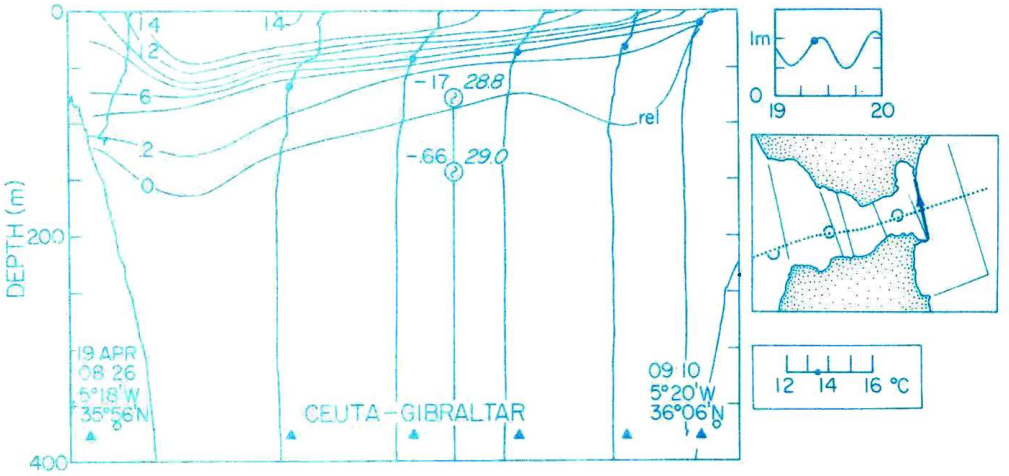
DEPTH (m)
0
200
400
14
12
6
2
0
-17 28.8
-.66 29.0
rel
19 APR
08 26
5°18'W
35°56'N
CEUTA–GIBRALTAR
09 10
5°20'W
36°06'N
1m
0
19
20
12 14 16 °C

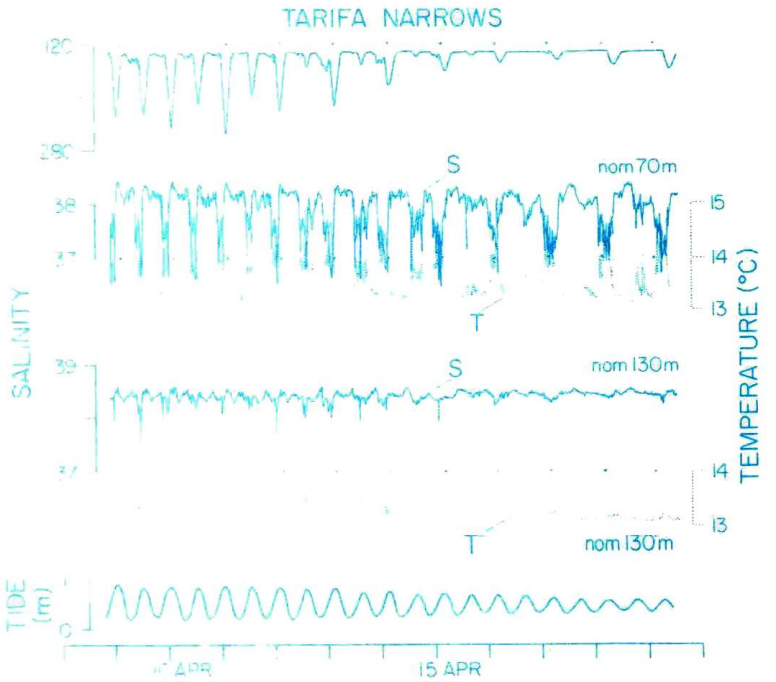
TARIFA NARROWS
120
280
S
nom 70m
38
34
15
14
13
T
SALINITY
39
37
S
nom 130m
14
13
T
nom 130m
TEMPERATURE (°C)
TIDE (m)
0
14 APR
15 APR

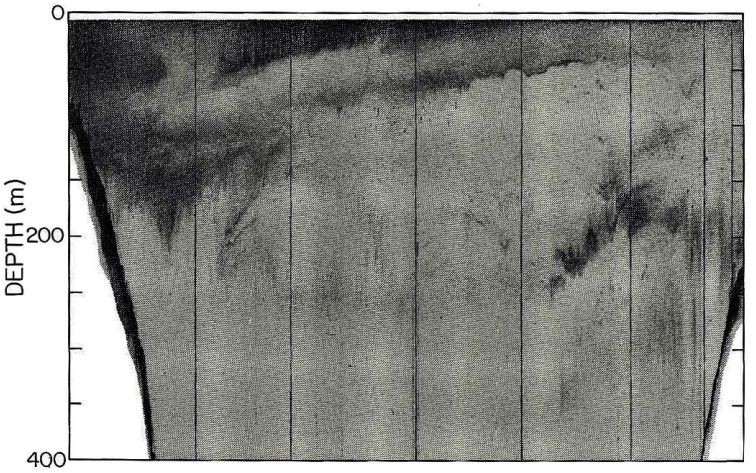


*Fig. 8.2.* Transect, looking east, between Cueta and Gibraltar.
*Overlay.* Temperature profiles and contours of flow in $ms^{-1}$. The Tarifa Narrows (9E) current meter data is included for reference.

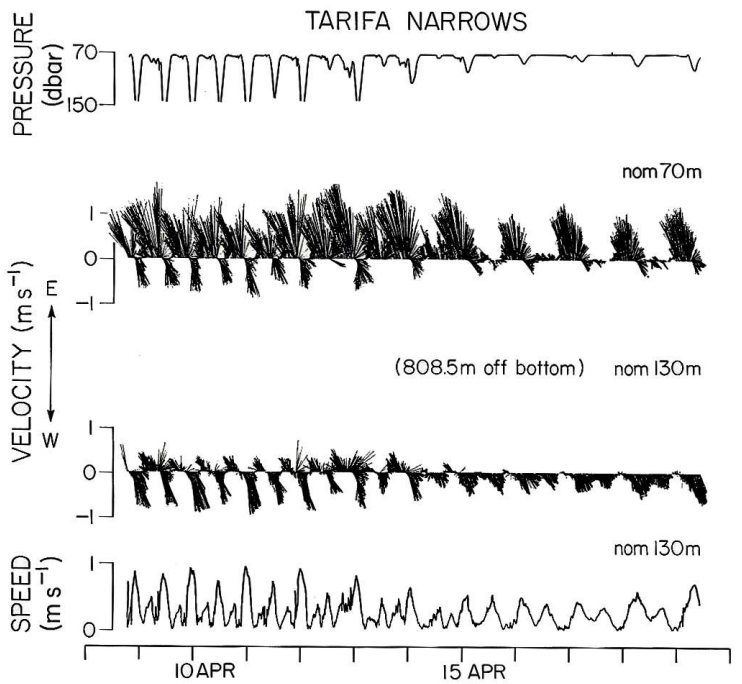


*Fig. 8.3.* Current vectors from two instruments in Tarifa Narrows (9E), together with pressure at the uppermost and speed at the deepest current meter.
*Overlay.* Temperature (dotted lines) and salinity (solid lines) time series for each instrument, together with predicted tidal height. Pressure at the deepest current meter is also shown.

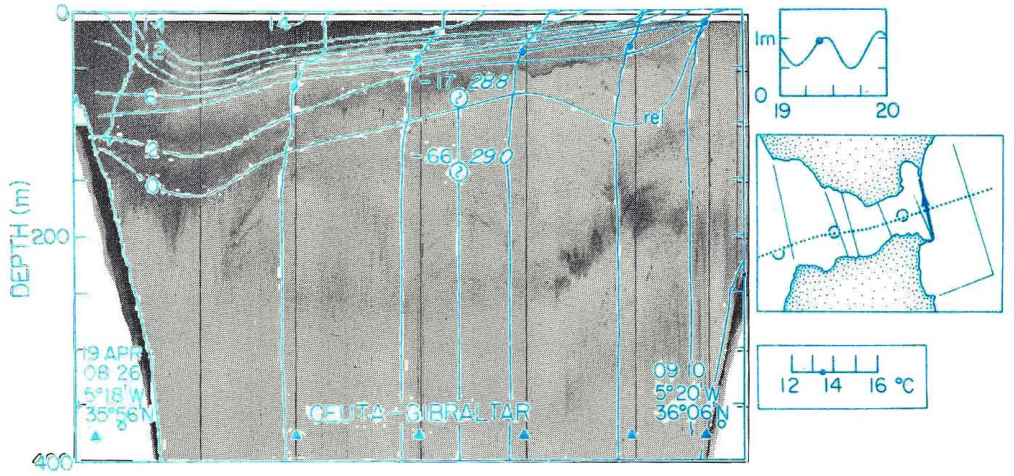


*Fig. 8.2.* Transect, looking east, between Cueta and Gibraltar.
*Overlay.* Temperature profiles and contours of flow in $ms^{-1}$. The Tarifa Narrows (9E) current meter data is included for reference.

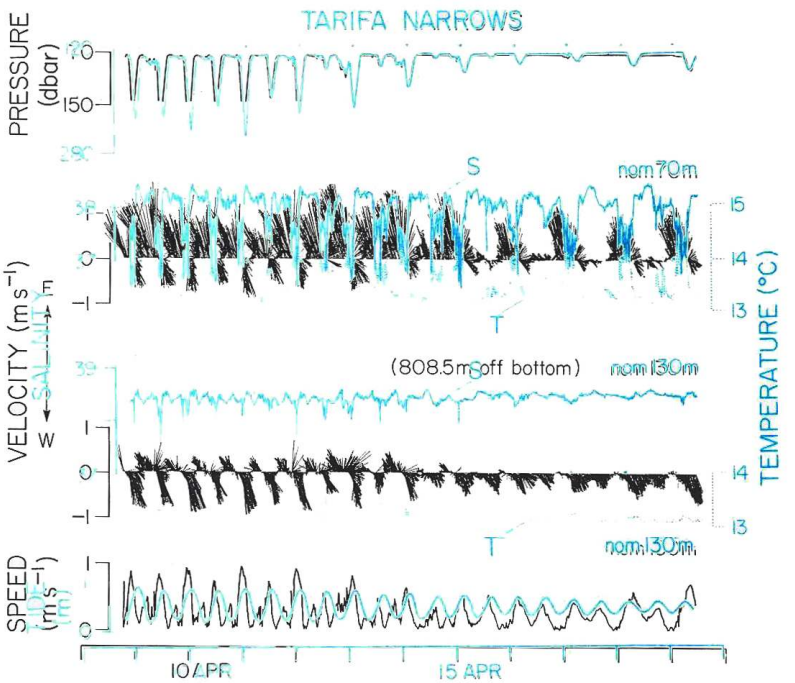


*Fig. 8.3.* Current vectors from two instruments in Tarifa Narrows (9E), together with pressure at the uppermost and speed at the deepest current meter.
*Overlay.* Temperature (dotted lines) and salinity (solid lines) time series for each instrument, together with predicted tidal height. Pressure at the deepest current meter is also shown.

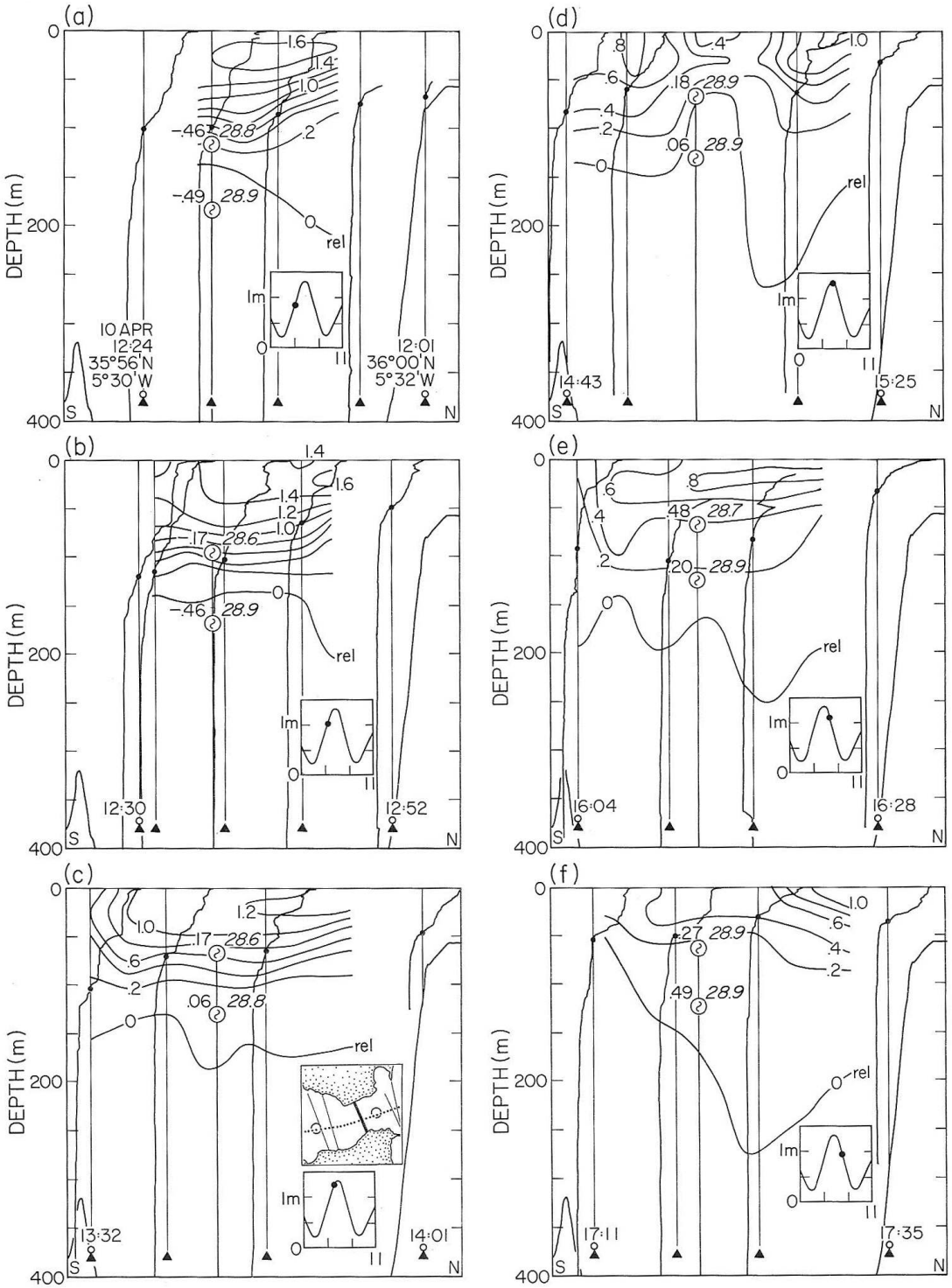


*Fig. 8.4a-f.* Rapid sequence of transects at station 5E showing temperature (solid lines) and contours of velocity together with along strait velocities and densities from the nearby mooring (9E), incorporated at actual depths.

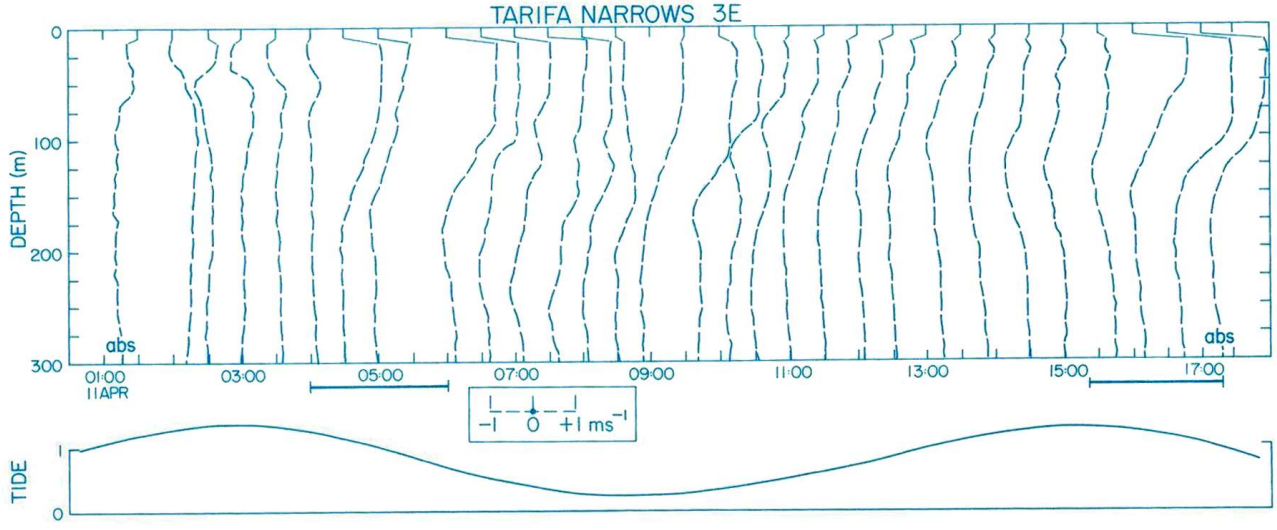
TARIFA NARROWS 3E
DEPTH (m)
0
100
200
300
abs
abs
01·00
11 APR
03·00
05·00
07·00
09·00
11·00
13·00
15·00
17·00
−1 0 +1 ms⁻¹
TIDE
1
0

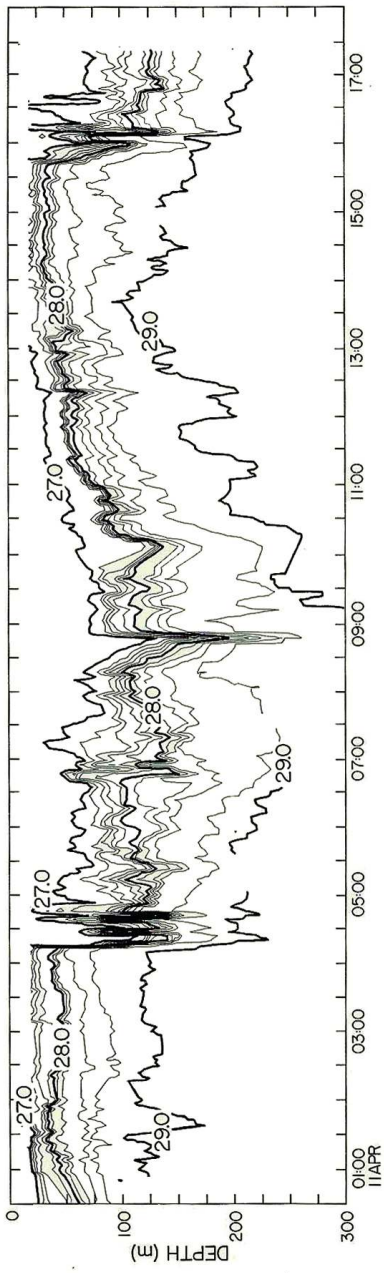


*Fig. 8.5.* Contours of constant density derived from a CTD time series at station 3E in Tarifa Narrows. Isopycnals less than 27.0 and greater than 29.0 have been excluded to simplify the presentation and make the interface displacement more clearly visible.
*Overlay.* Doppler velocity profiles (dashed lines). The horizontal bars (0400-0600 h) and (1520-1720 h) indicate periods during which the mode 1 internal bore travels eastward past the station, shown in detail in Fig. 12.3a & b.

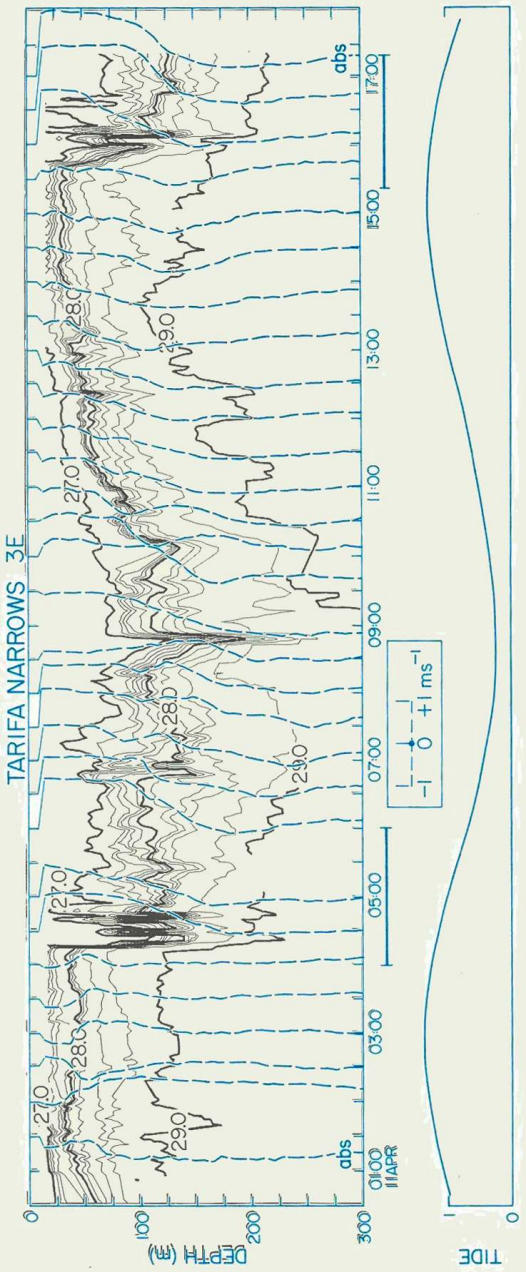


*Fig. 8.5.* Contours of constant density derived from a CTD time series at station 3E in Tarifa Narrows. Isopycnals less than 27.0 and greater than 29.0 have been excluded to simplify the presentation and make the interface displacement more clearly visible.
*Overlay.* Doppler velocity profiles (dashed lines). The horizontal bars (0400-0600 h) and (1520-1720 h) indicate periods during which the mode 1 internal bore travels eastward past the station, shown in detail in Fig. 12.3a & b.

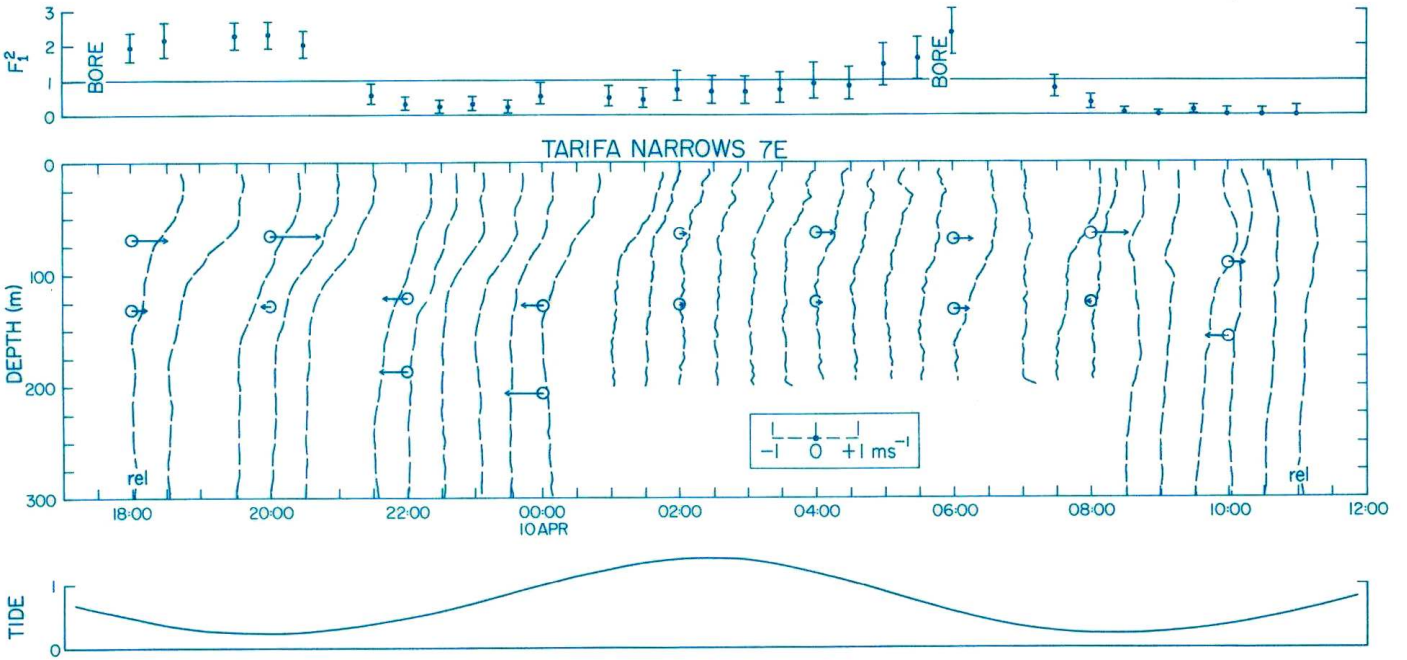
$F_1^2$
3
2
1
0
BORE
BORE
TARIFA NARROWS 7E
DEPTH (m)
0
100
200
300
rel
rel
−1 0 +1 ms⁻¹
18·00
20·00
22·00
00·00
10 APR
02·00
04·00
06·00
08·00
10·00
12·00
TIDE
1
0

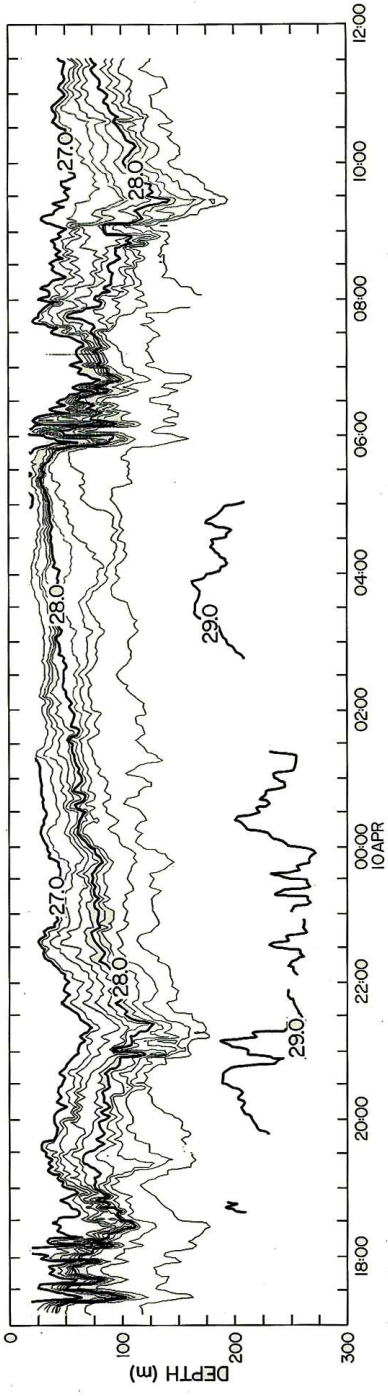


*Fig. 8.6.* Contours of constant density derived from a CTD time series at station 7E in Tarifa Narrows. Isopycnals less than 27.0 and greater than 29.0 have been excluded to simplify the presentation and make the interface displacement more clearly visible.
*Overlay.* Doppler velocity profiles (dashed lines) and corresponding current speed (arrows) at actual depths from the nearby mooring (9E). Internal Froude numbers of the upper layer are shown above.

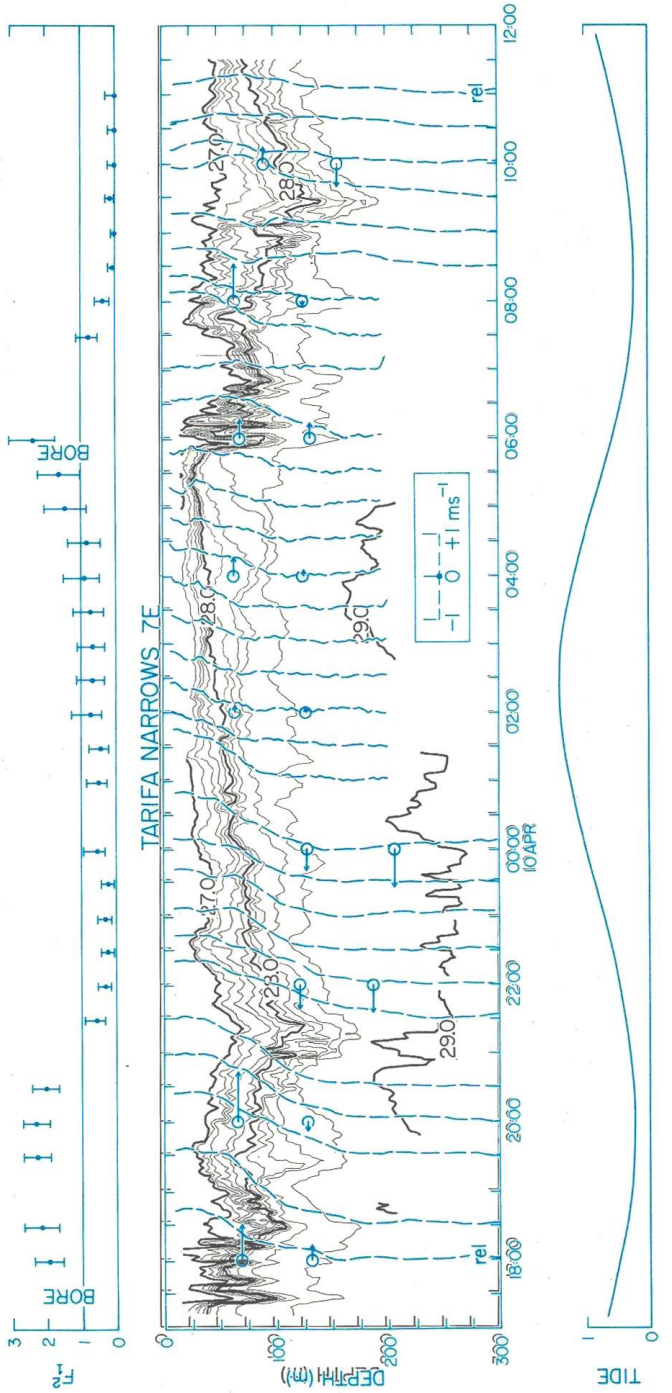


*Fig. 8.6.* Contours of constant density derived from a CTD time series at station 7E in Tarifa Narrows. Isopycnals less than 27.0 and greater than 29.0 have been excluded to simplify the presentation and make the interface displacement more clearly visible.
*Overlay.* Doppler velocity profiles (dashed lines) and corresponding current speed (arrows) at actual depths from the nearby mooring (9E). Internal Froude numbers of the upper layer are shown above.

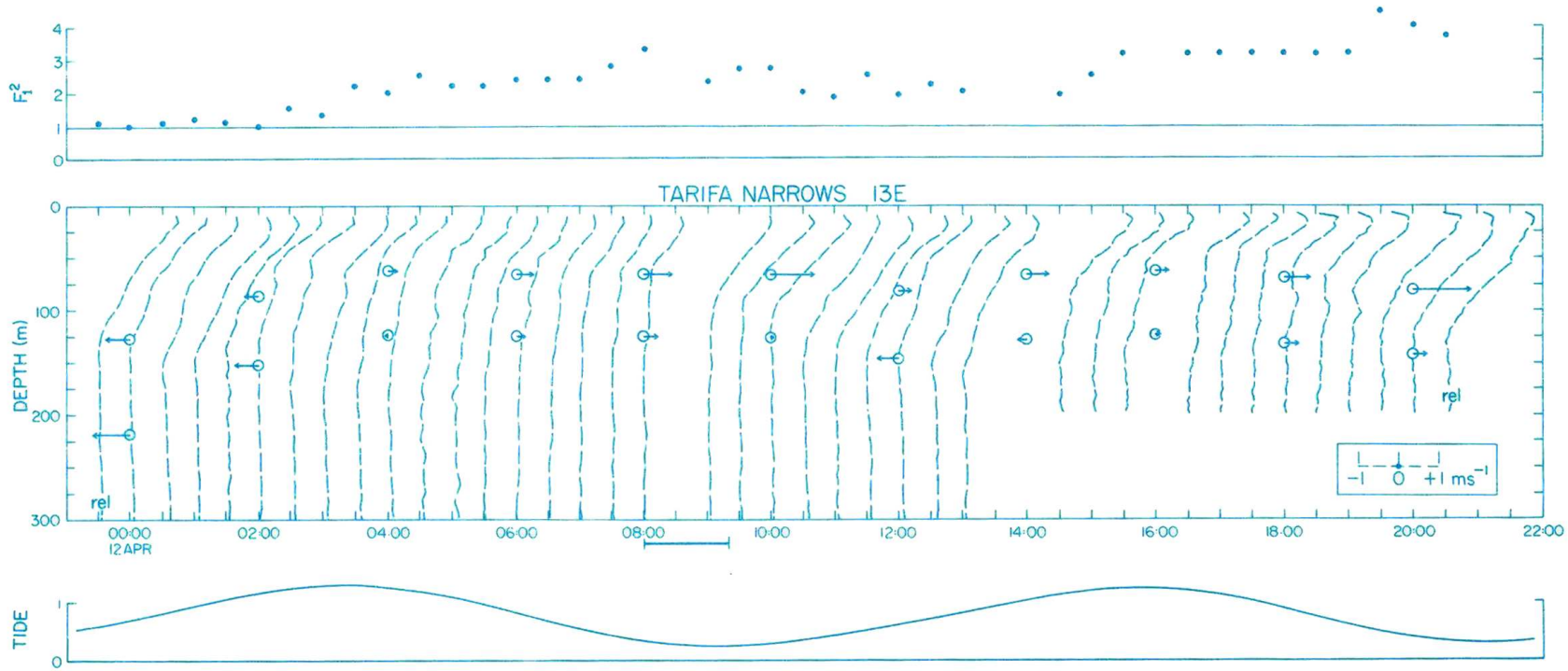
$F_1^2$
4
3
2
1
0
TARIFA NARROWS 13E
DEPTH (m)
0
100
200
300
rel
rel
−1 0 +1 ms⁻¹
00:00
12 APR
02:00
04:00
06:00
08:00
10:00
12:00
14:00
16:00
18:00
20:00
22:00
TIDE
1
0

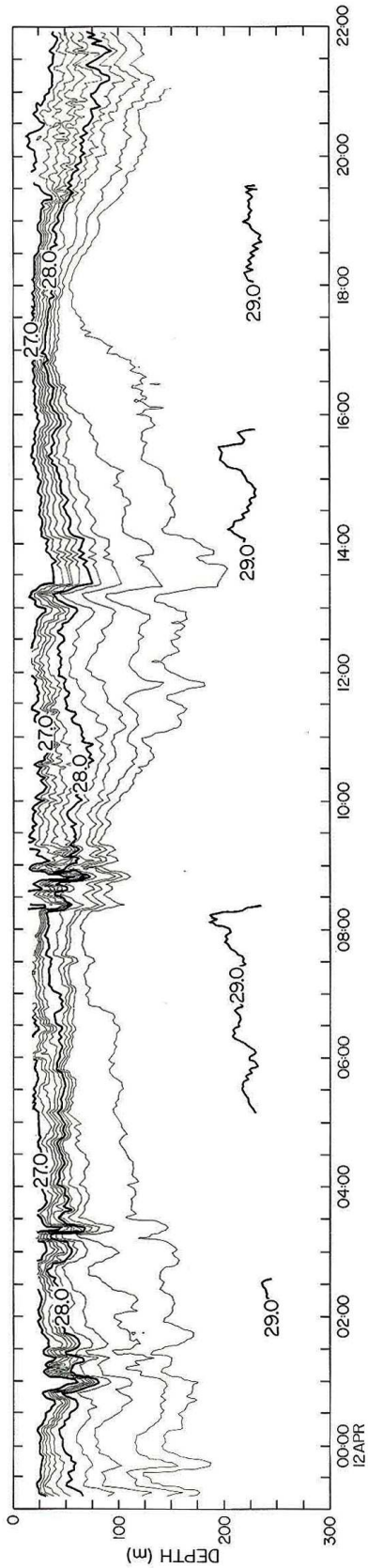


*Fig. 8.7.* Contours of constant density derived from a CTD time series at station 13E in Tarifa Narrows. Isopycnals less than 27.0 and greater than 29.0 have been excluded to simplify the presentation and make the interface displacement more clearly visibile.
*Overlay.* Doppler velocity profiles (dashed lines) and corresponding current speed (arrows) at actual depths from mooring at 9E. The horizontal bar indicates period during which the mode 1 internal bore travels eastward past the station, shown in detail in Fig. 12.4. Internal Froude numbers of the upper layer are shown above.

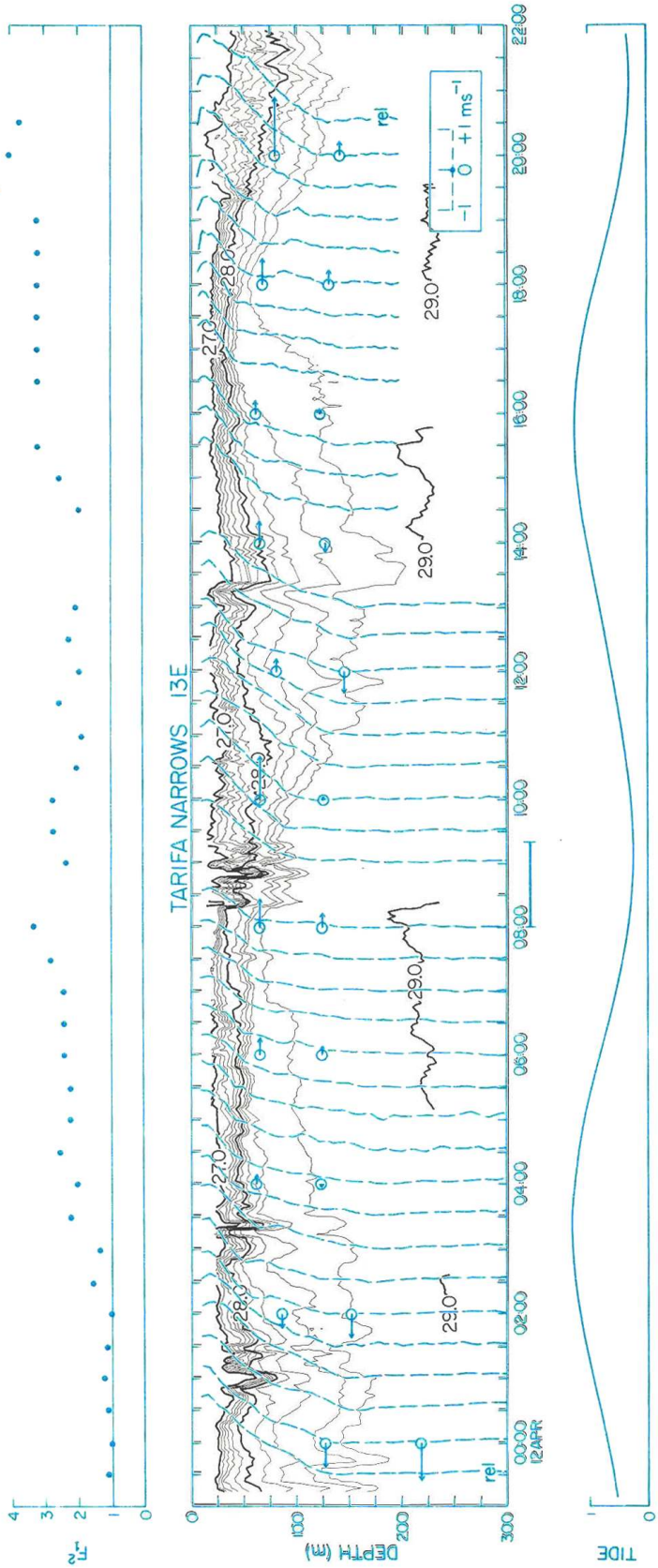


*Fig. 8.7.* Contours of constant density derived from a CTD time series at station 13E in Tarifa Narrows. Isopycnals less than 27.0 and greater than 29.0 have been excluded to simplify the presentation and make the interface displacement more clearly visibile.
*Overlay.* Doppler velocity profiles (dashed lines) and corresponding current speed (arrows) at actual depths from mooring at 9E. The horizontal bar indicates period during which the mode 1 internal bore travels eastward past the station, shown in detail in Fig. 12.4. Internal Froude numbers of the upper layer are shown above.

*Fig. 8.8.* A run along the strait from Tangier Basin to well past Gibraltar. The acoustic image is shown with temperature profiles (solid lines) and density profiles (dotted lines).

*Fig. 9.1.* This transect bounds the volume of interest in the east and includes a corner with an additional segment running back to the African coast. The image shows the Atlantic surface layer (generally dark), the presence of internal waves, and a very small backscatter signal associated with the visible surface slick. Doppler contours illustrate the wedge-shaped structure of the jet. South of this jet lies a thick ( ~100m) layer of almost motionless Atlantic water.

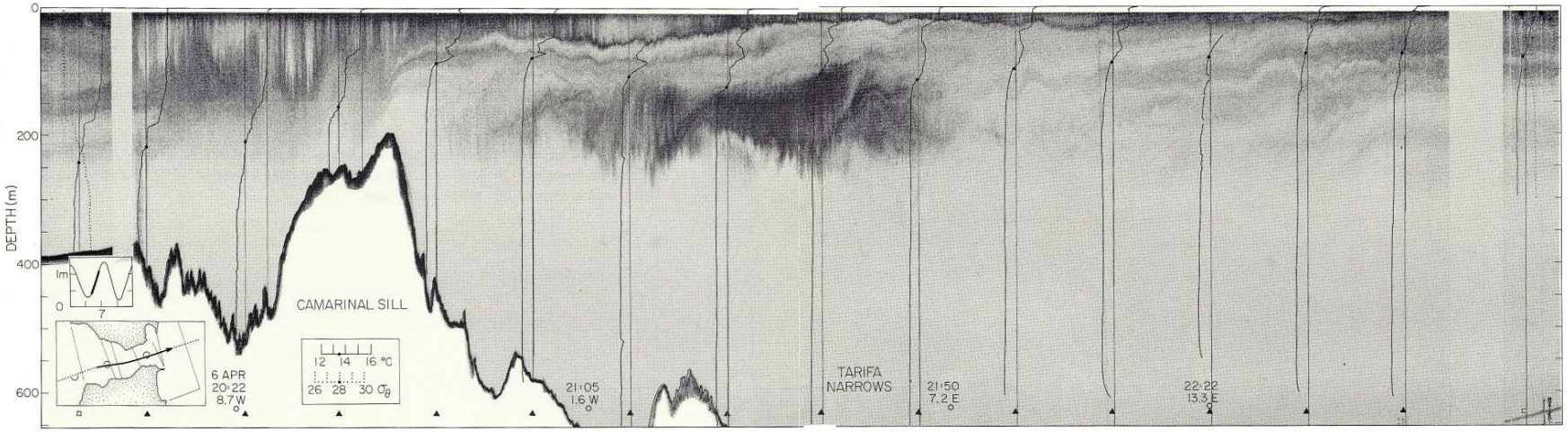
DEPTH (m)
0
200
400
600
CAMARINAL SILL
6 APR
20·22
8·7 W
21·05
1·6 W
TARIFA
NARROWS
21·50
7·2 E
22·22
13·3 E
12 14 16 °C
26 28 30 σθ
1m
0
7

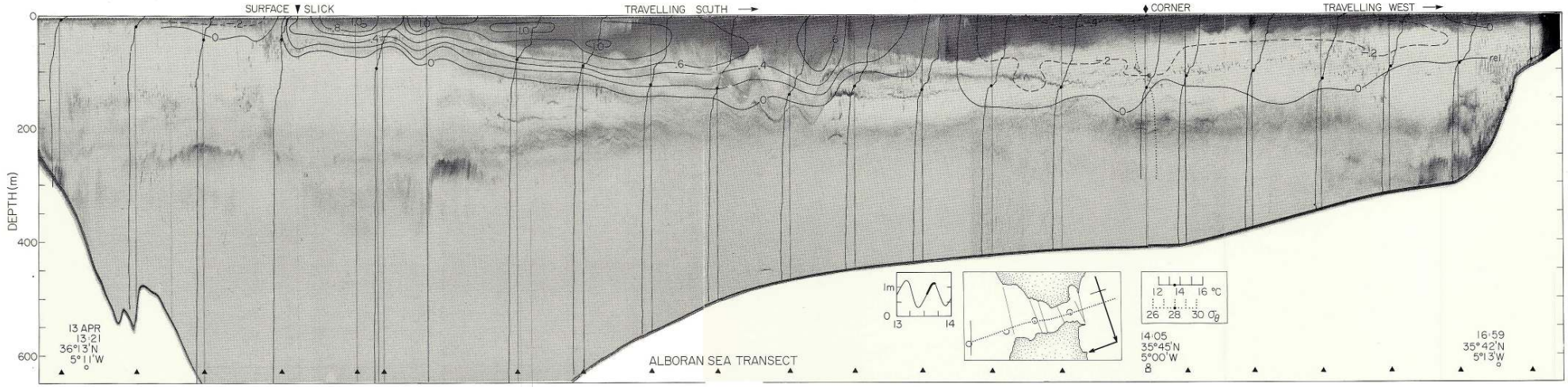
SURFACE ▼ SLICK
TRAVELLING SOUTH →
◆ CORNER
TRAVELLING WEST →
DEPTH (m)
0
200
400
600
13 APR
13·21
36°13'N
5°11'W
ALBORAN SEA TRANSECT
14·05
35°45'N
5°00'W
16·59
35°42'N
5°13'W
12 14 16 °C
26 28 30 σθ
1m
0
13
14
rel

*Fig. 10.1.* Acoustic image of a run along the length of the strait illustrating the main hydraulic features on 20 October 1985.
*Overlay.* Temperature profiles (solid lines), and velocity profiles (dashed lines) obtained from XCPs. The dot on each temperature profile indicates the drop position, and a temperature of 13.5°C for comparison with April data, and the '+' symbol is located at 15°C. At this time of year, the interface spans this temperature range.

*Fig. 10.2.* As for Fig.10.1, but 21 October.

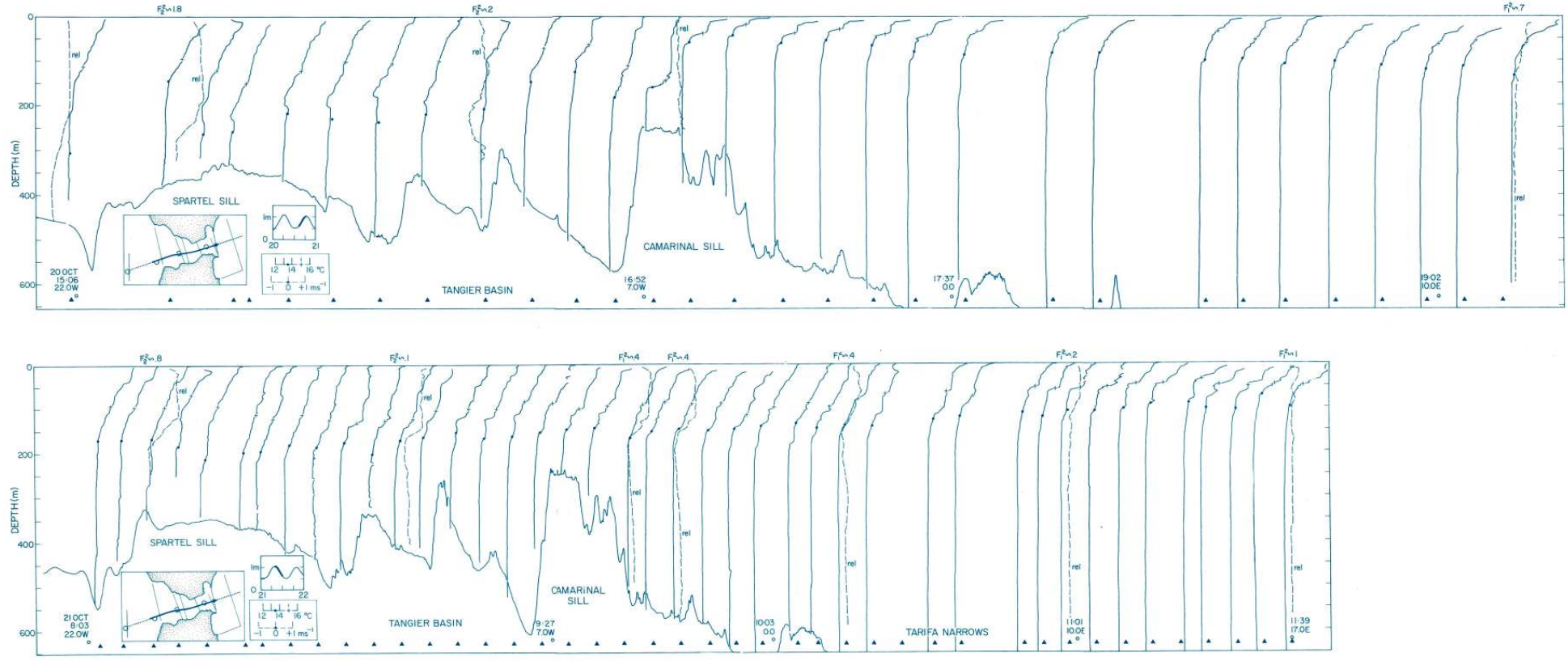
$F_2^2$m.18
$F_2^2$m.2
$F_1^2$m.7
DEPTH (m)
0
200
400
600
rel
SPARTEL SILL
lm
0
20
21
12
14
16 °C
-1
0
+1 ms⁻¹
20 OCT
15·06
22·0W
TANGIER BASIN
CAMARINAL SILL
16·52
7·0W
17·37
0·0
19·02
10·0E
$F_2^2$m.8
$F_2^2$m.1
$F_2^2$m.4
$F_1^2$m.4
$F_1^2$m.4
$F_1^2$m.2
$F_1^2$m.1
21 OCT
8·03
22·0W
21
22
9·27
7·0W
10·03
0·0
TARIFA NARROWS
11·01
10·0E
11·39
17·0E

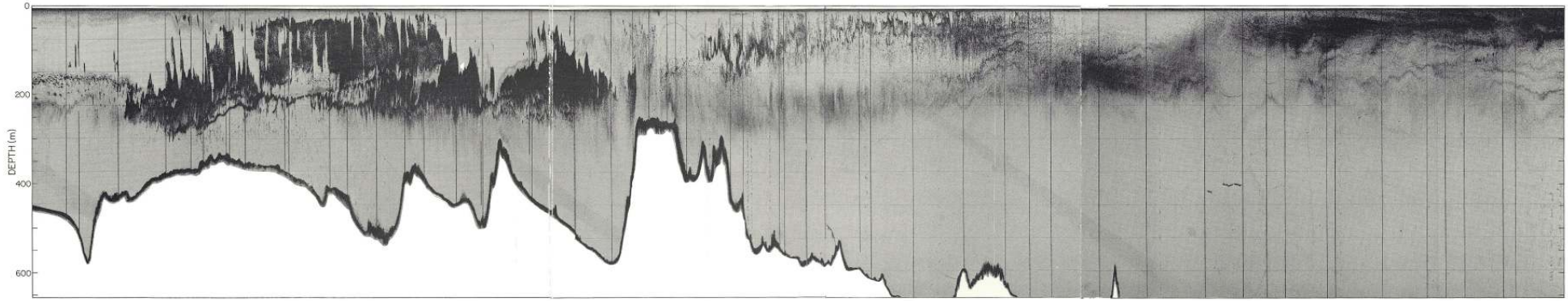
0
200
400
600
DEPTH (m)

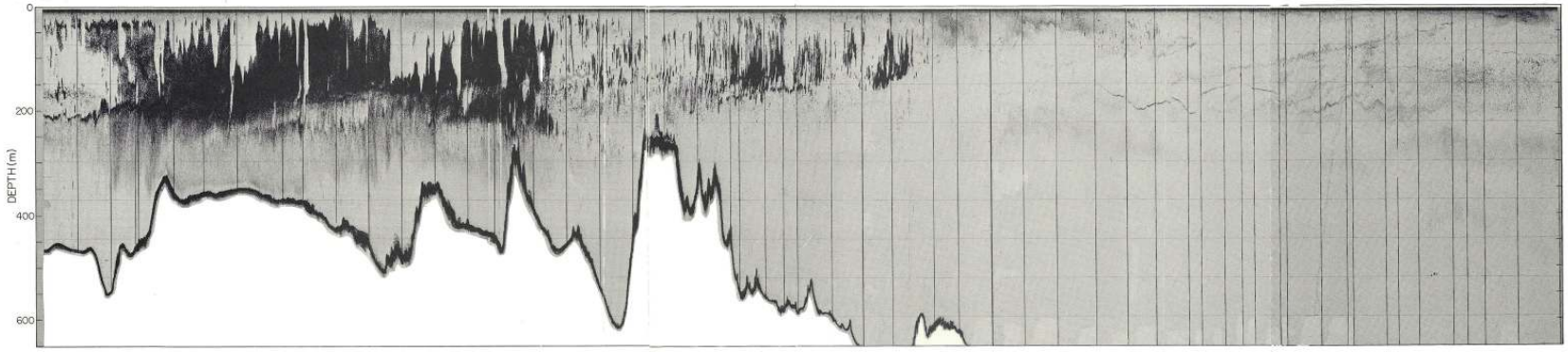
0
200
400
600
DEPTH (m)

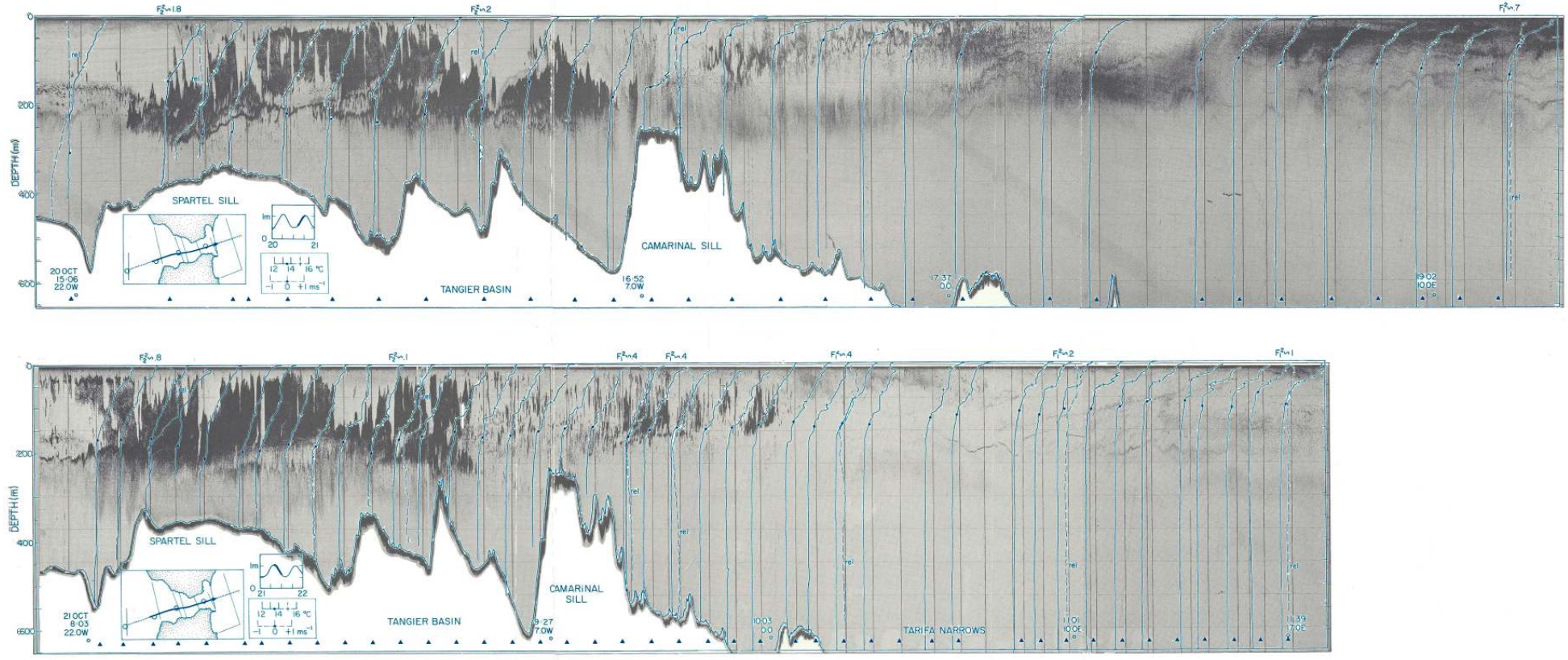
F2m18
F2m2
F1m7
DEPTH (m)
0
200
400
600
rel
SPARTEL SILL
CAMARINAL SILL
TANGIER BASIN
20 OCT
15·06
22·0W
16·52
7·0W
17·37
0·0
19·02
10·0E
F2m8
F2m1
F1m4
F1m4
F1m4
F1m2
F1m1
SPARTEL SILL
CAMARINAL SILL
TANGIER BASIN
TARIFA NARROWS
21 OCT
8·03
22·0W
9·27
7·0W
10·03
0·0
11·01
10·0E
11·39
7·0E

*Fig. 11.1.* Radar image (courtesy of Gary Watson, University of Southampton) showing surface slick on 25 April. The radar observations were made from the Rock of Gibraltar and the image is superimposed on a chart of the Gibraltar-Ceuta area (adapted from Fig. 2.1). Also shown is a segment from the Alboran Sea transect (see Fig. 9.1) showing location of surface slick at the same stage of tide, but on 13 April.

*Fig. 11.2.* Cartoon showing three-dimensional perspective view of the jet and surface slick. The velocity field is derived from data in Figs. 8.1b (10 April), 8.1c (25 April) and 9.1 (13 April).

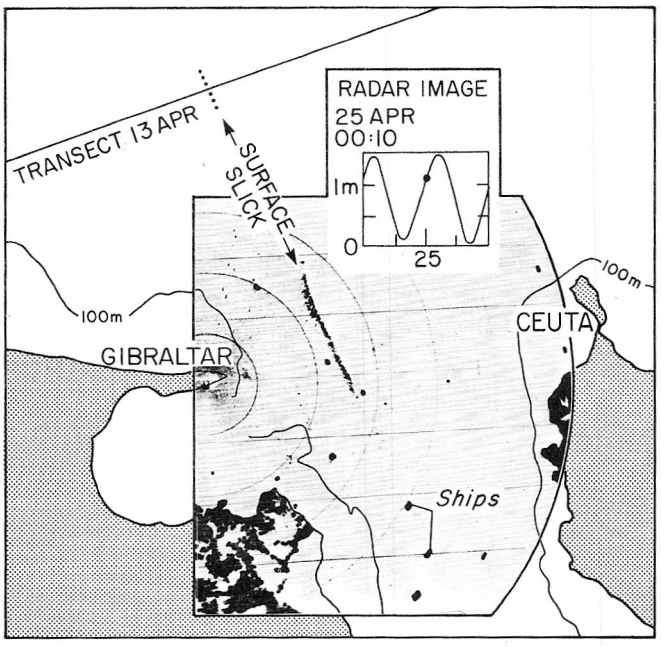
TRANSECT 13 APR
SURFACE SLICK
RADAR IMAGE
25 APR
00:10
1m
0
25
100m
100m
GIBRALTAR
CEUTA
Ships

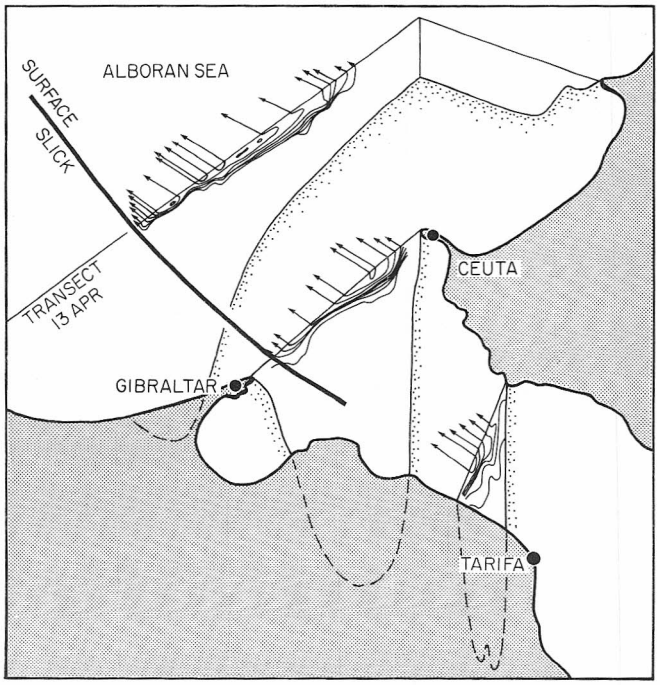
SURFACE SLICK
ALBORAN SEA
TRANSECT 13 APR
CEUTA
GIBRALTAR
TARIFA

*Fig. 12.1a.* Bore over Camarinal Sill at the time of its release.
Current meter velocity (horizontal arrows) and density and Doppler profiles (dashed lines) are also shown. (see Fig. 12.2).

*Fig. 12.1b.* Structure over Camarinal Sill two hours after Fig 12.1a, during period of reverse flow.

*Fig. 12.1c.* Lee waves generated on east flank of Camarinal Sill during reverse flow.

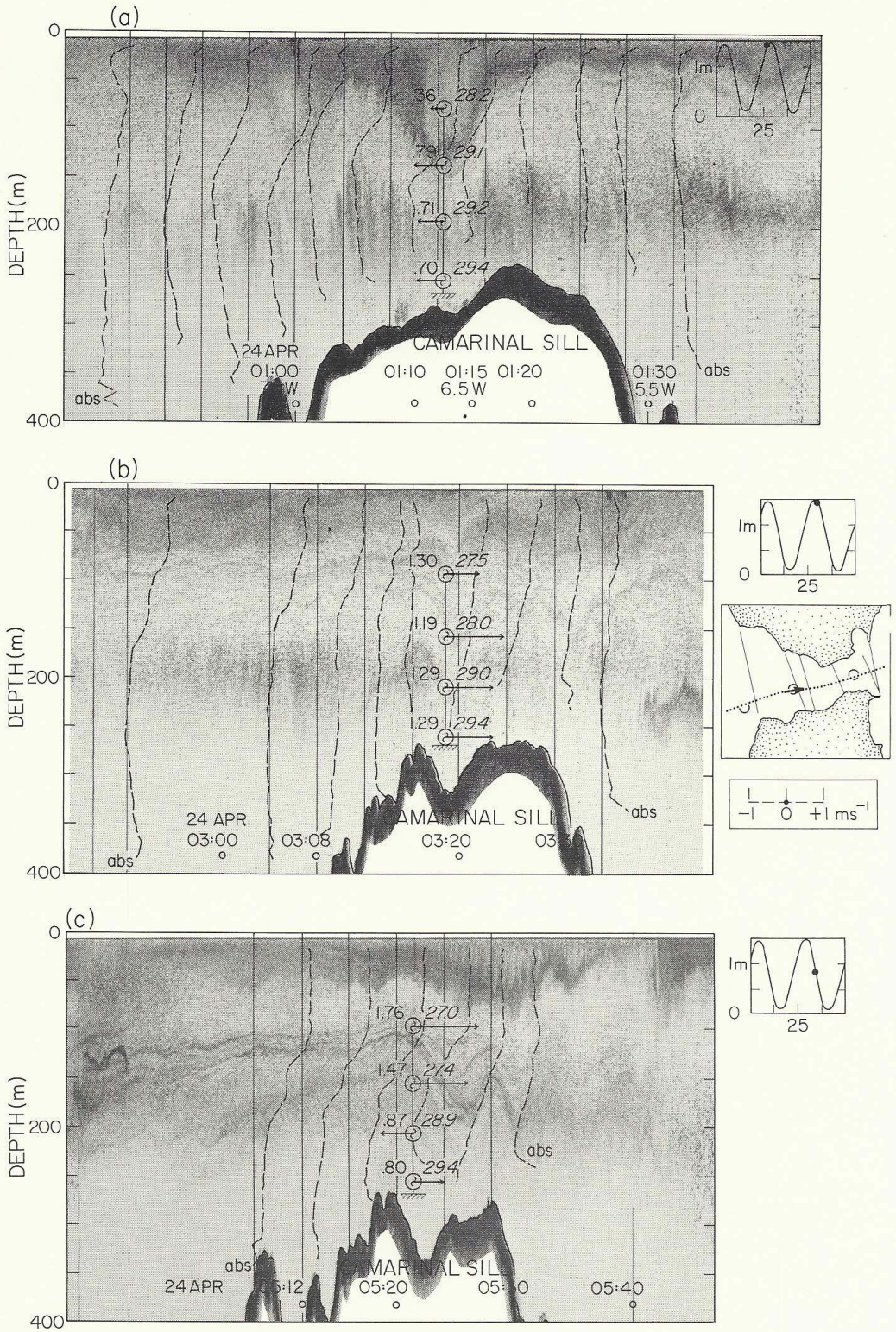
(a)
0
DEPTH (m)
200
400
1m
0
25
36 28.2
.79 29.1
.71 29.2
.70 29.4
CAMARINAL SILL
24 APR
01:00
01:10 01:15 01:20
01:30
6.5 W
5.5 W
abs
abs
(b)
1.30 27.5
1.19 28.0
1.29 29.0
1.29 29.4
24 APR
03:00
03:08
03:20
abs
abs
−1 0 +1 ms⁻¹
(c)
1.76 27.0
1.47 27.4
.87 28.9
.80 29.4
abs
24 APR
05:20
05:30
05:40

CAMARINAL SILL

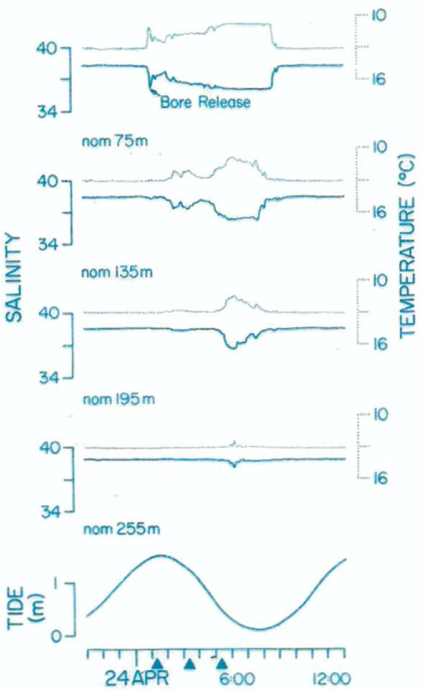

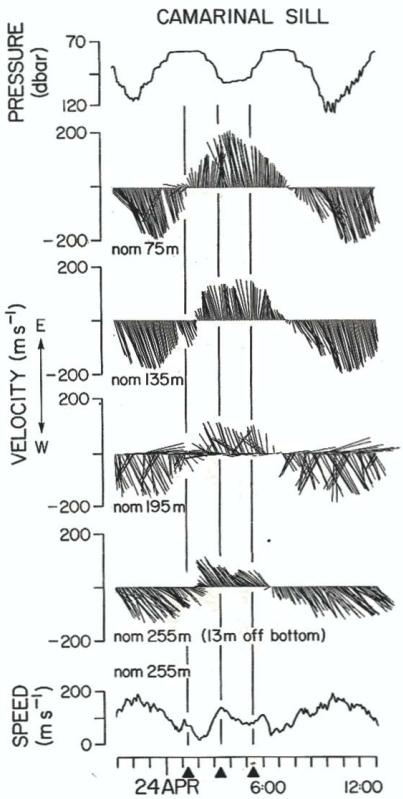


*Fig. 12.2.* Current vectors from the current meters over Camarinal Sill, together with pressure at the uppermost and speed at the deepest meter, displayed on an expanded scale for the period of bore release shown in Fig. 12.1. The vertical lines correspond to the time at which the vessel passed near the mooring for each of the three figures respectively.
*Overlay.* Temperature (dotted lines) and salinity (solid lines) time series for each instrument, together with predicted tidal height.

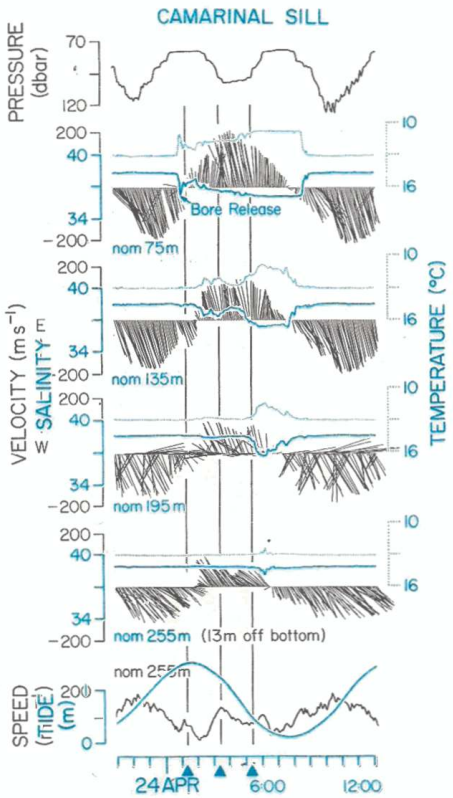


*Fig. 12.2.* Current vectors from the current meters over Camarinal Sill, together with pressure at the uppermost and speed at the deepest meter, displayed on an expanded scale for the period of bore release shown in Fig. 12.1. The vertical lines correspond to the time at which the vessel passed near the mooring for each of the three figures respectively.
*Overlay.* Temperature (dotted lines) and salinity (solid lines) time series for each instrument, together with predicted tidal height.

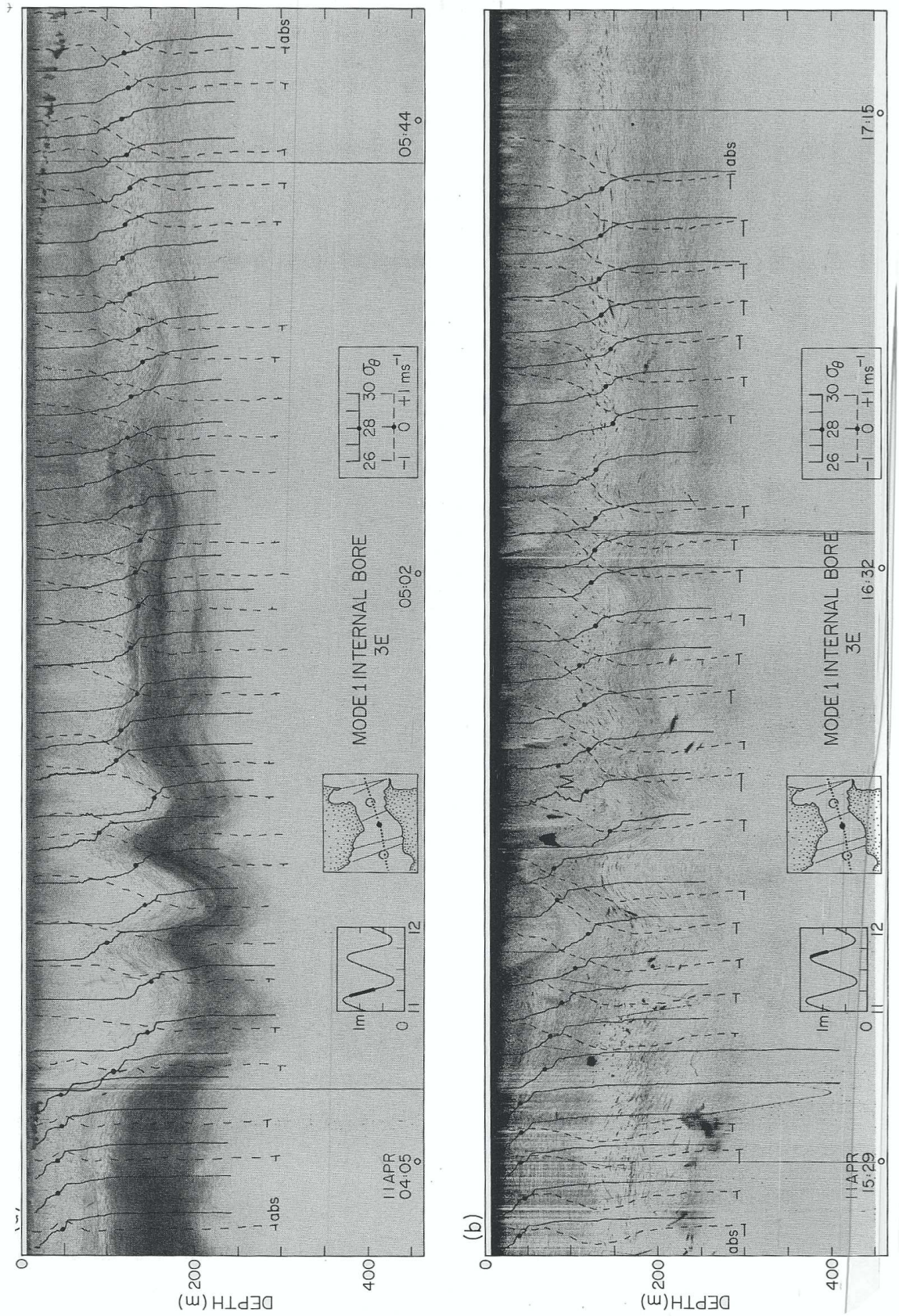
(b)
DEPTH (m)
0
200
400
11 APR
04·05
05·02
05·44
MODE 1 INTERNAL BORE
3E
abs
26 28 30 $\sigma_\theta$
−1 0 +1 ms$^{-1}$
0 1 2
km
11 APR
15·29
16·32
17·15

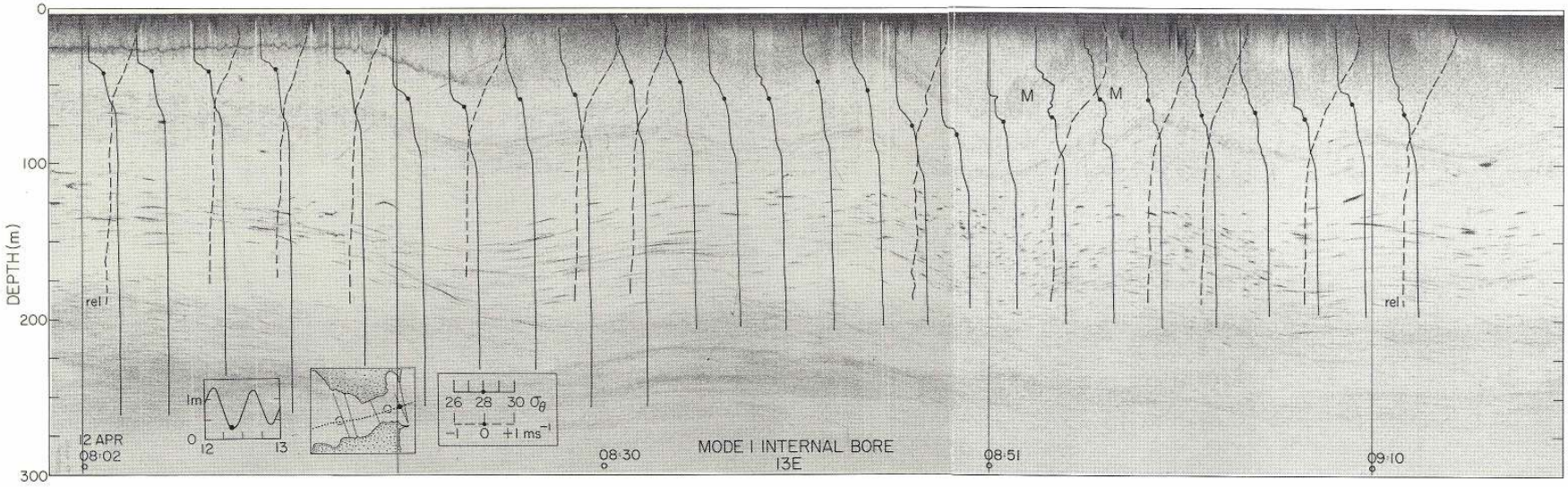


*Fig. 12.4.* Acoustic image of mode 1 internal bore, during the transition between spring and neap tides, passing station 13E. Doppler (dashed lines) and CTD density (solid lines) profiles; 'M' indicates finestructure in profile representative of turbulence and mixing.

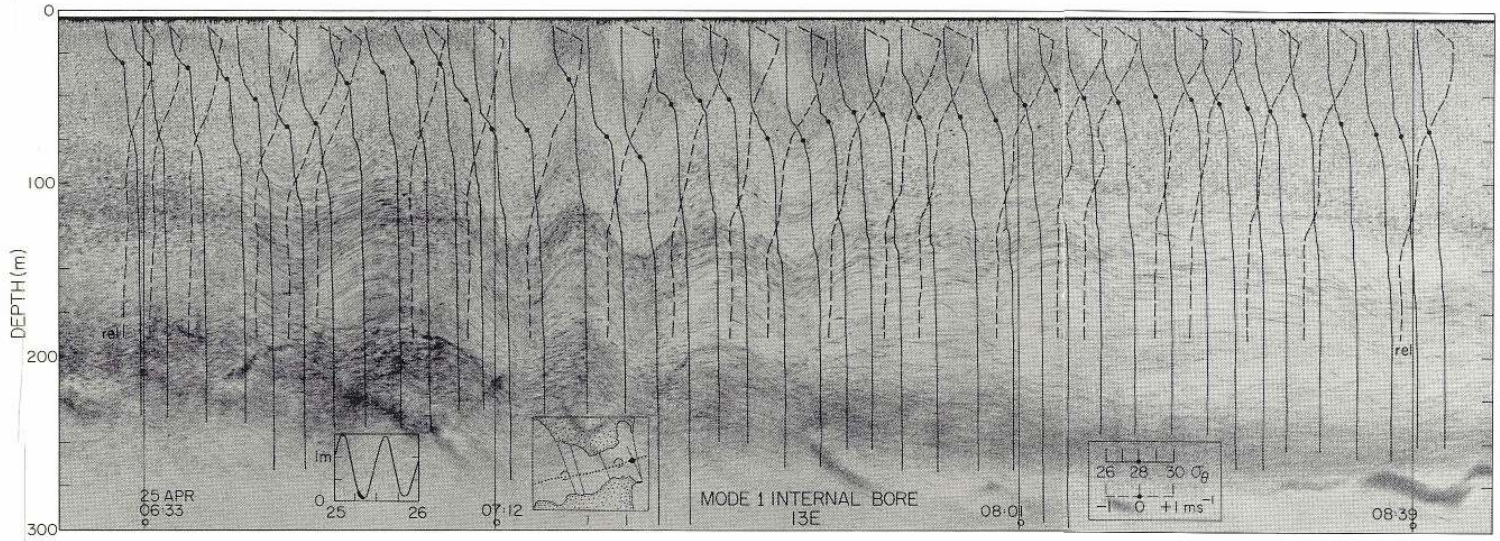


*Fig. 12.5.* As for Fig. 12.4 of mode 1 internal bore during a spring tide passing station 13E.

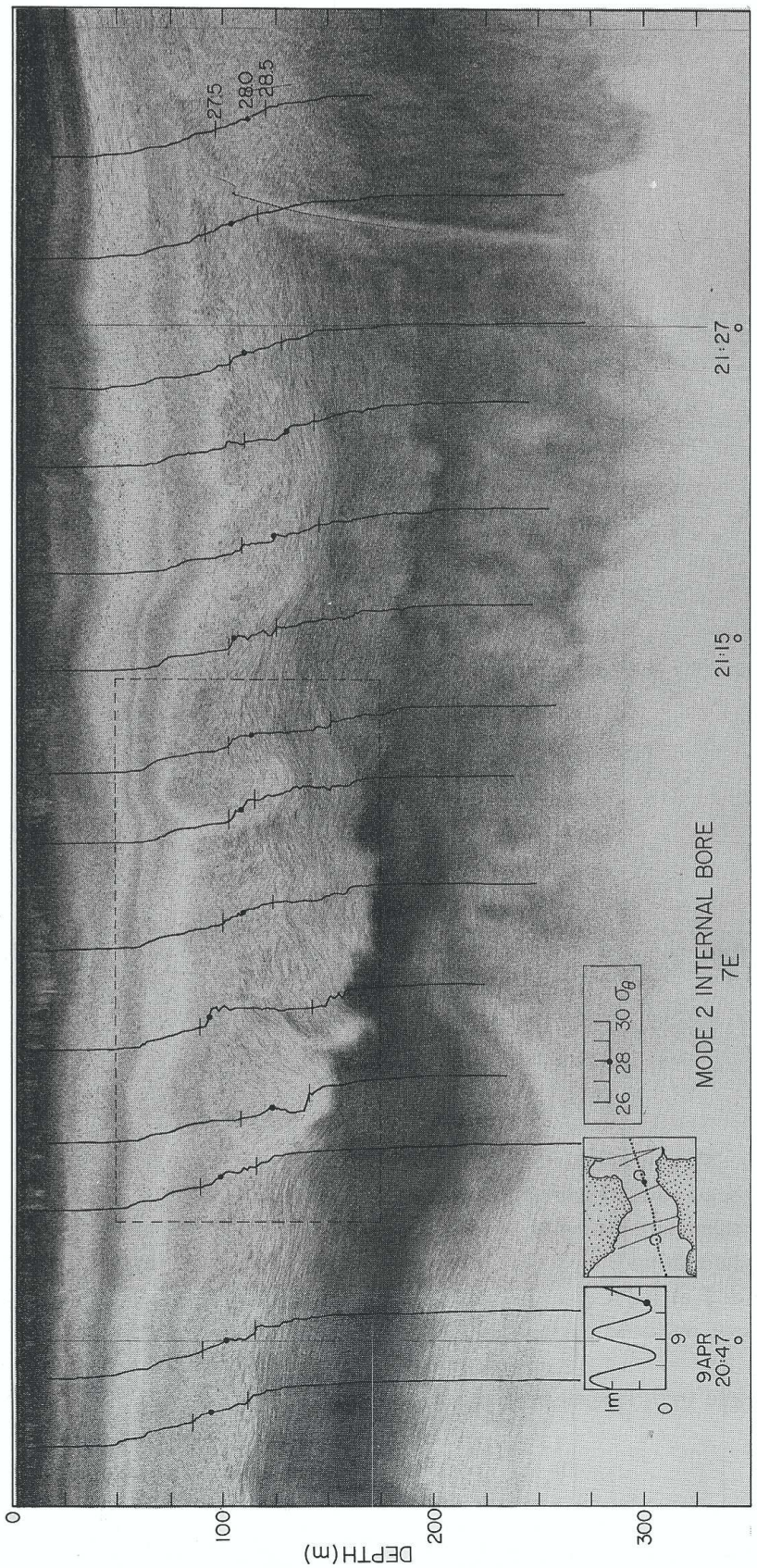


*Fig. 12.6.* Image of mode 2 bore passing station 7E. The bore appears as a spreading of the scatterers. Dashed box encloses location of scatterer spreading as the bore passes. Corresponding spreading of the isopycnals can also be identified in the CTD profiles. However, it should be noted that these are not perfectly aligned with the acoustic image, since a CTD profile takes approximately 3 minutes.

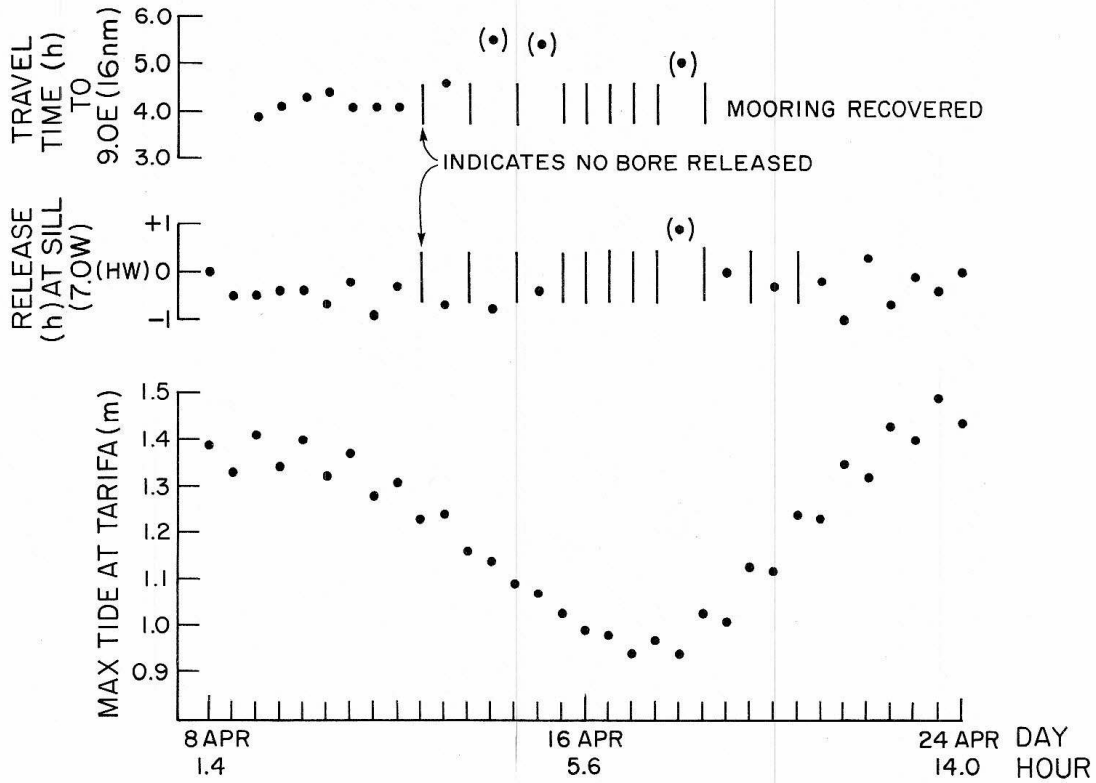


*Fig. 12.7 (Lower).* Height of maximum tide at Tarifa between 8 and 24 April. Each mark on the time axis is spaced so as to correspond with the tidal maximum.

*(Middle).* The corresponding time at which we observe the release of a bore at Camarinal Sill. Vertical bars indicate that no bore was released or detected. Data were derived from temperature and salinity recorded at the Camarinal Sill and station 9 moorings. The points enclosed in parentheses represent probable passage of the bore, for which the temperature/salinity signal is weak.

*(Upper).* Travel time from the sill to station 9E.

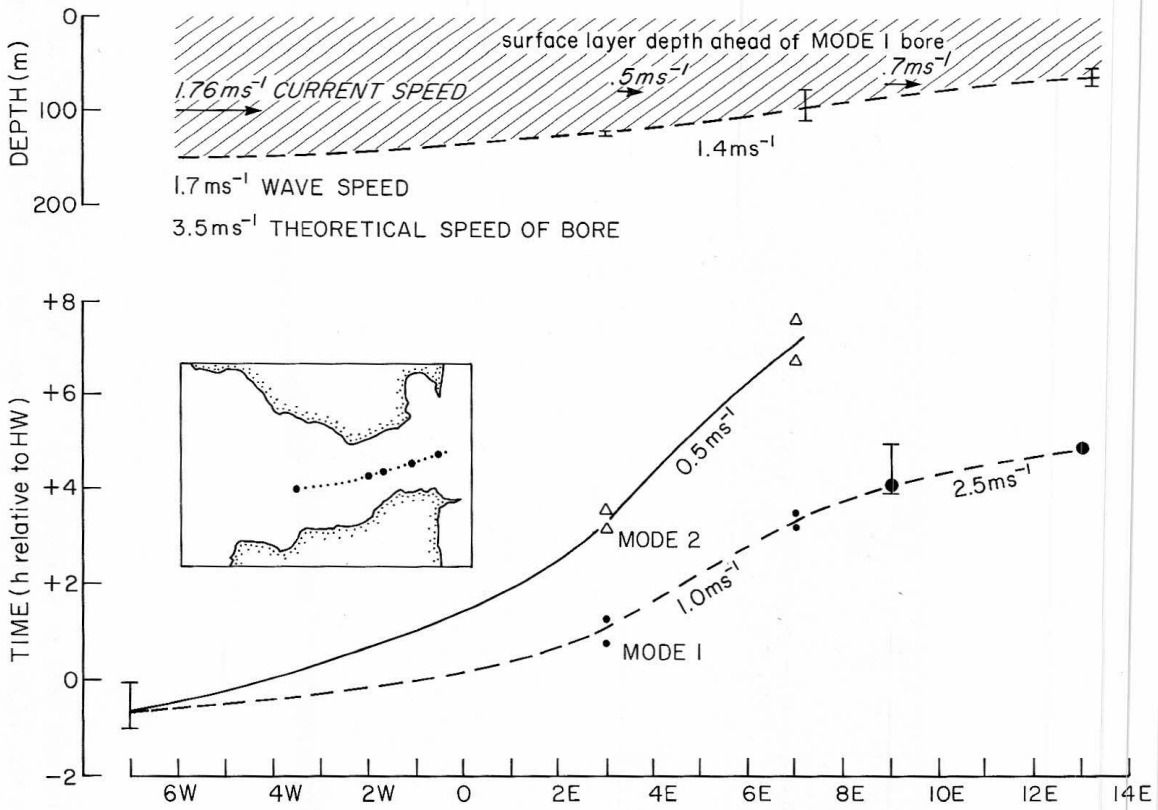


*Fig. 12.8 (Lower).* Space-time diagram showing propagation of both mode 1 and mode 2 bores along the strait. The bores travel more rapidly as they move through the eastern part of the strait.

*(Upper).* Representative interface depth, surface layer speed, and theoretical bore speed (mode 1) as á function of the distance from the sill.

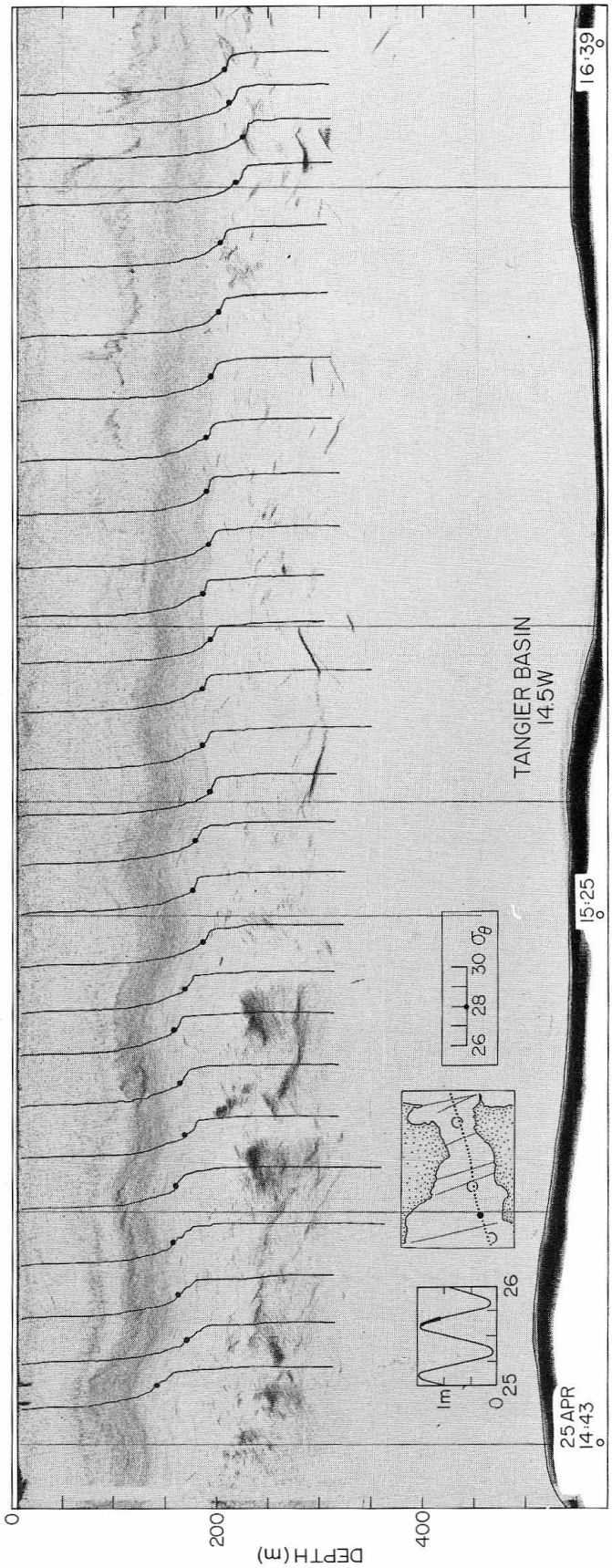


*Fig. 12.9.* Small internal bore in Tangier Basin. This bore is released following a strong inflowing tide (see Fig. 12.1c) and travels west through Tangier Basin. Shown with CTD density profiles (solid lines).

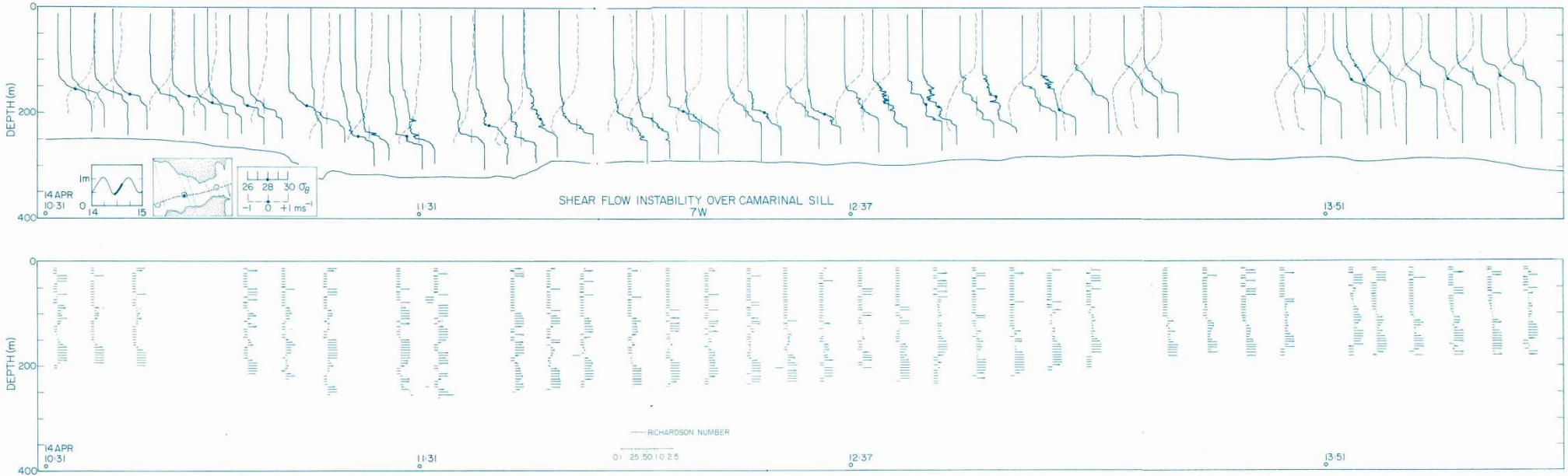
DEPTH (m)
0
200
400
1m
14 APR
10·31
0
14
15
26 28 30 $\sigma_\theta$
−1 0 +1 ms⁻¹
11·31
SHEAR FLOW INSTABILITY OVER CAMARINAL SILL
7W
12·37
13·51
DEPTH (m)
0
200
400
14 APR
10·31
RICHARDSON NUMBER
0·1 2·5 5·0 10 25
11·31
12·37
13·51

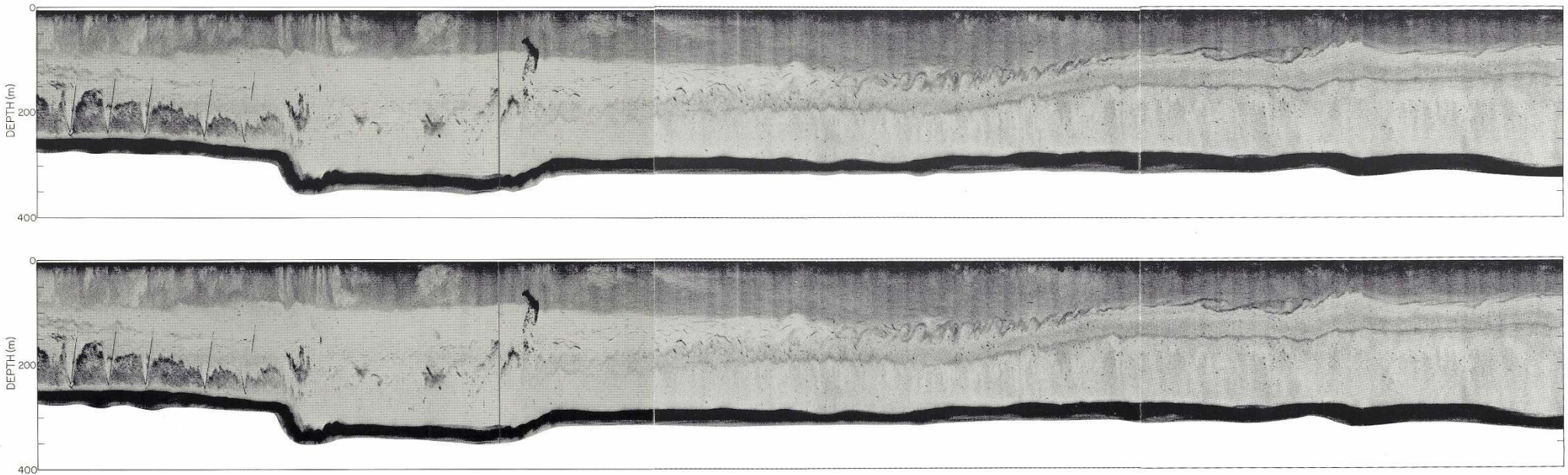


*Fig. 13.1a,b.* Image of shear flow instabilities obtained during a time series observation near the crest of Camarinal Sill.

*Overlay 13.1a.* CTD density (solid lines) and Doppler velocity (dashed lines) profiles. Short vertical line indicates position, and time and reference values (28.0, 0.0) simultaneously. Dot indicates position and reference value (28.0) for density profile when no simultaneous velocity data is shown. Finestructure in the density profiles appear at about 11.20 h, close to low water. As the tide rises the shear increases, instabilities appear in the image and finestructure in the density profiles is enhanced. Note that the instabilities occur in the uppermost portion of the interval of density stratification, or even at the base of the relatively well-mixed surface layer.

*Overlay 13.1b.* Richardson number profiles derived from the velocity and density profiles of Fig. 13.1a. These profiles are drawn on a logarithmic scale centered on Ri=0.25. Higher Richardson numbers occur in the deeper layer. Significantly lower values occur in, and especially just above, the interface, at the same depth as instabilities seen in the image.

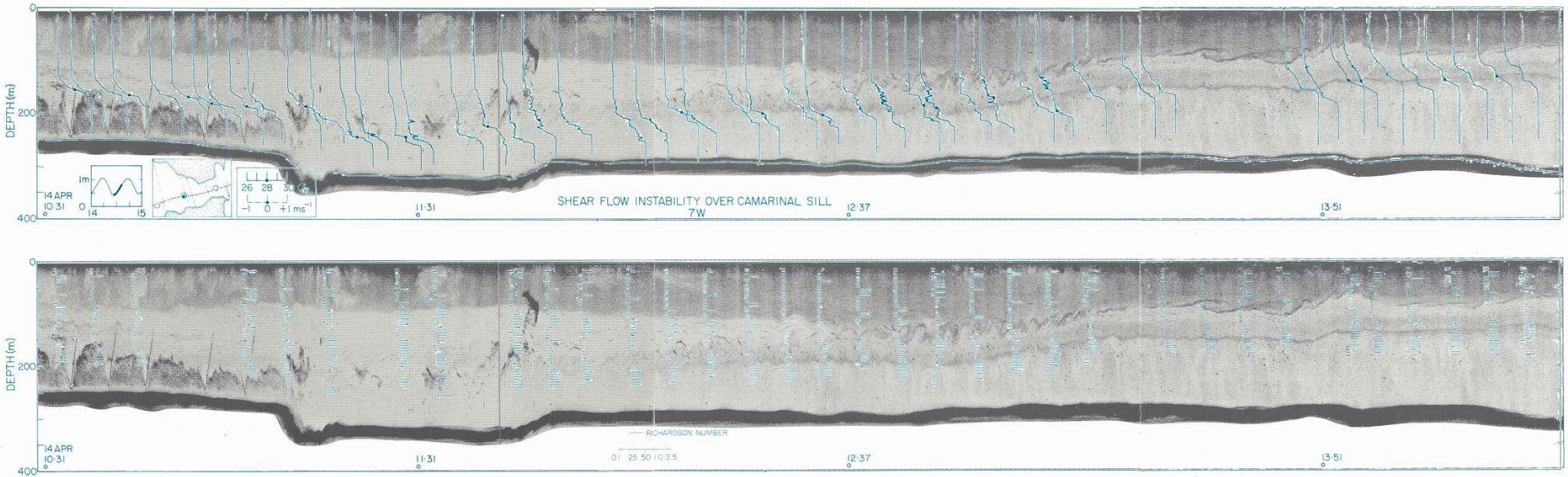


*Fig. 13.1a,b.* Image of shear flow instabilities obtained during a time series observation near the crest of Camarinal Sill.

*Overlay 13.1a.* CTD density (solid lines) and Doppler velocity (dashed lines) profiles. Short vertical line indicates position, and time and reference values (28.0, 0.0) simultaneously. Dot indicates position and reference value (28.0) for density profile when no simultaneous velocity data is shown. Finestructure in the density profiles appear at about 11.20 h, close to low water. As the tide rises the shear increases, instabilities appear in the image and finestructure in the density profiles is enhanced. Note that the instabilities occur in the uppermost portion of the interval of density stratification, or even at the base of the relatively well-mixed surface layer.

*Overlay 13.1b.* Richardson number profiles derived from the velocity and density profiles of Fig. 13.1a. These profiles are drawn on a logarithmic scale centered on Ri=0.25. Higher Richardson numbers occur in the deeper layer. Significantly lower values occur in, and especially just above, the interface, at the same depth as instabilities seen in the image.

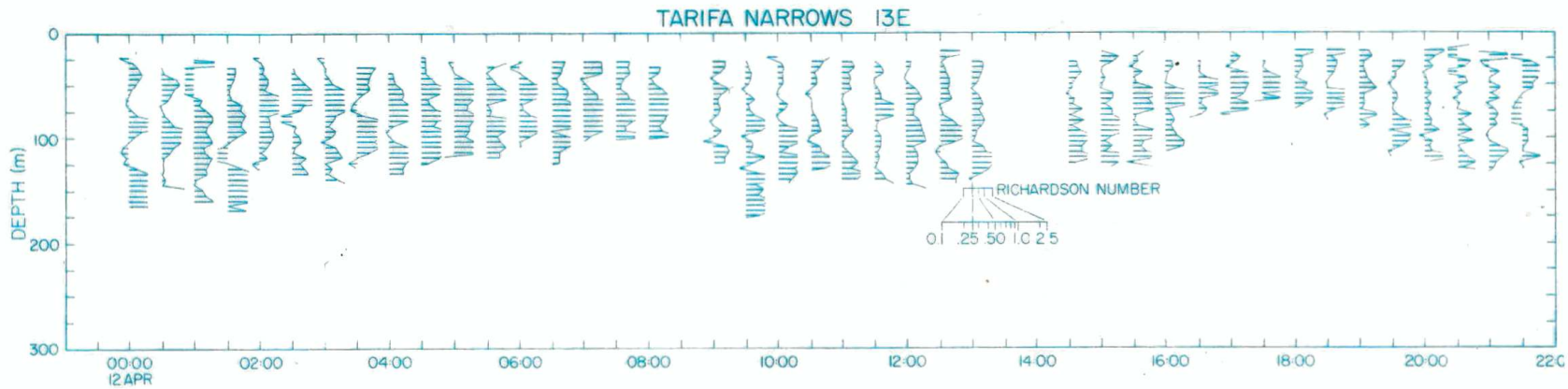
TARIFA NARROWS 13E
DEPTH (m)
0
100
200
300
00:00
12 APR
02:00
04:00
06:00
08:00
10:00
12:00
14:00
16:00
18:00
20:00
RICHARDSON NUMBER
0.1 .25 .50 1.0 2.5

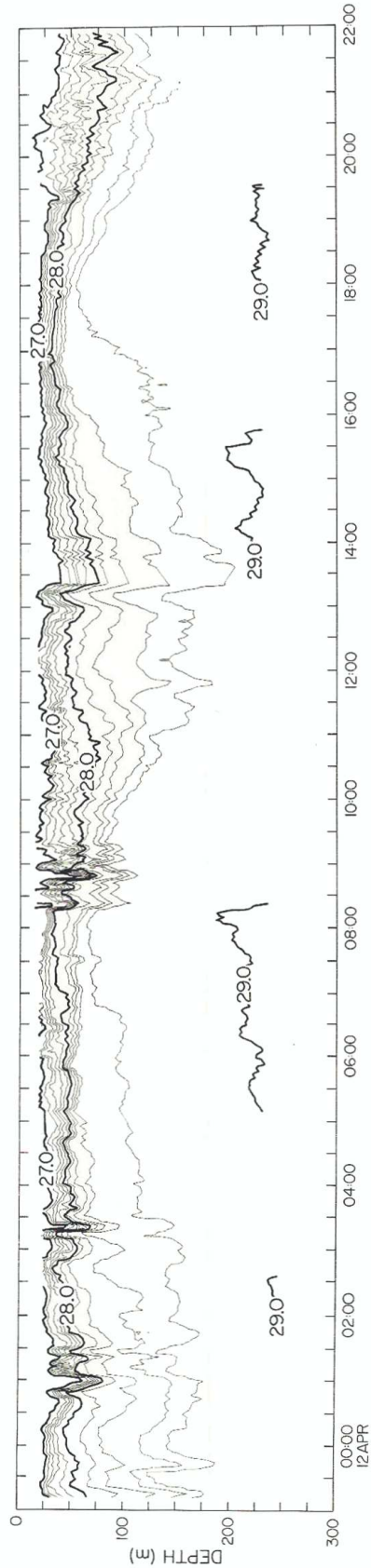


*Fig. 13.2.* Time series of density structure, showing isopycnals, at station 13E. Isopycnals less than 27.0 and greater than 29.0 have been excluded to simplify the presentation and make the interface displacement more clearly visible.

*Overlay.* Profiles of Richardson number. Note low values, corresponding to marginally stable or unstable flow, during the period of pycnocline deepening (0900-1100 and 1900-2100 h). Doppler velocity profiles and internal Froude numbers of the upper layer are shown on the overlay of Fig. 8.7.

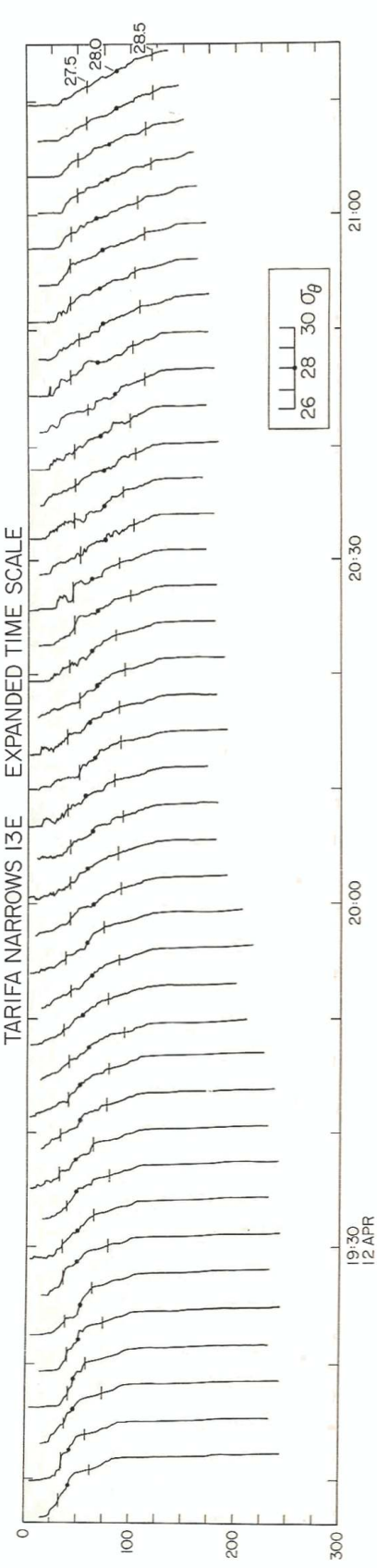


*Fig 13.3.* Individual CTD density profiles on an expanded time scale from Fig. 13.2, showing unambiguous evidence of instabilties associated with overturning.

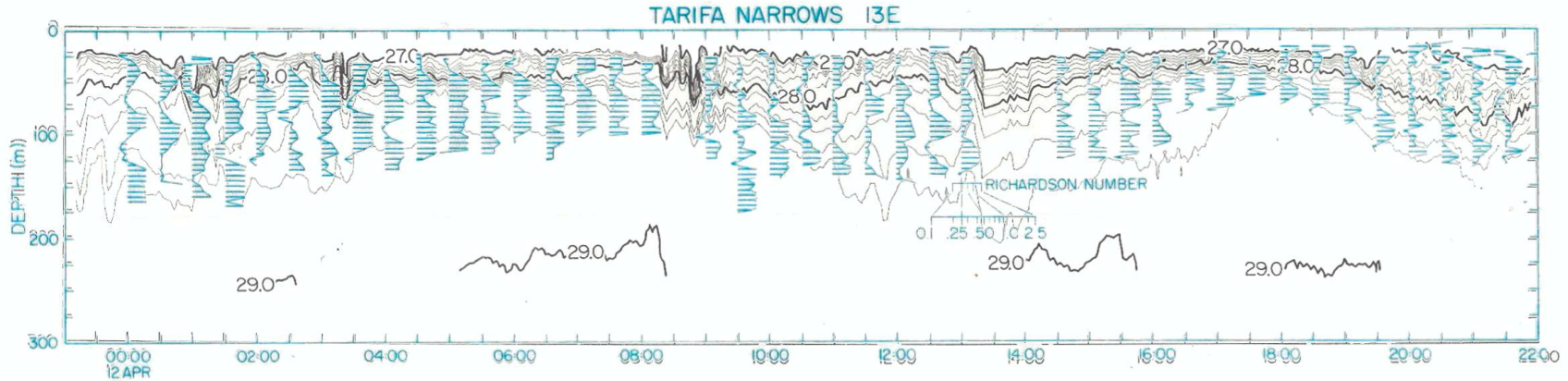


*Fig. 13.2.* Time series of density structure, showing isopycnals, at station 13E. Isopycnals less than 27.0 and greater than 29.0 have been excluded to simplify the presentation and make the interface displacement more clearly visible.

*Overlay.* Profiles of Richardson number. Note low values, corresponding to marginally stable or unstable flow, during the period of pycnocline deepening (0900-1100 and 1900-2100 h). Doppler velocity profiles and internal Froude numbers of the upper layer are shown on the overlay of Fig. 8.7.

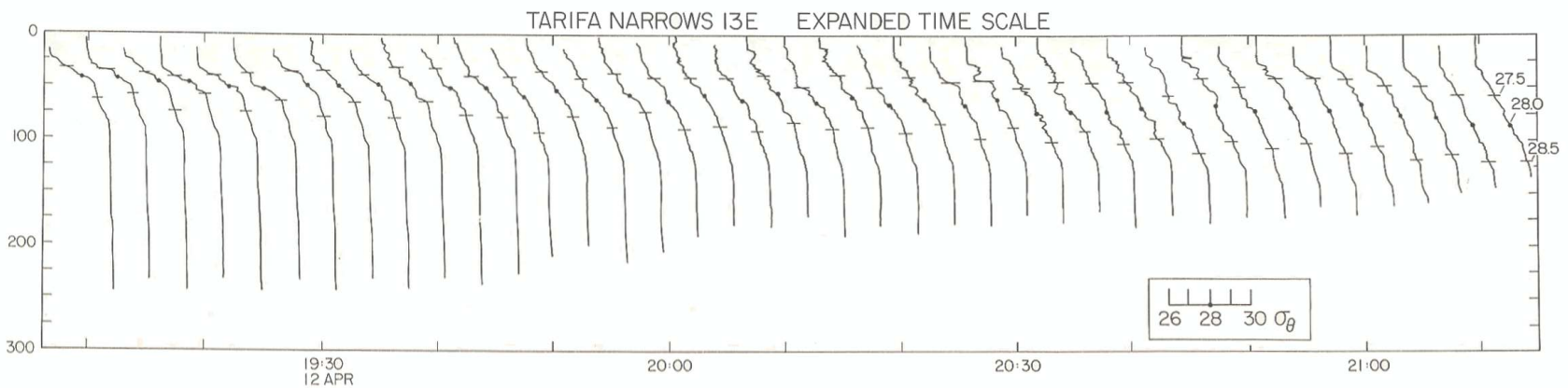


*Fig 13.3.* Individual CTD density profiles on an expanded time scale from Fig. 13.2, showing unambiguous evidence of instabilties associated with overturning.

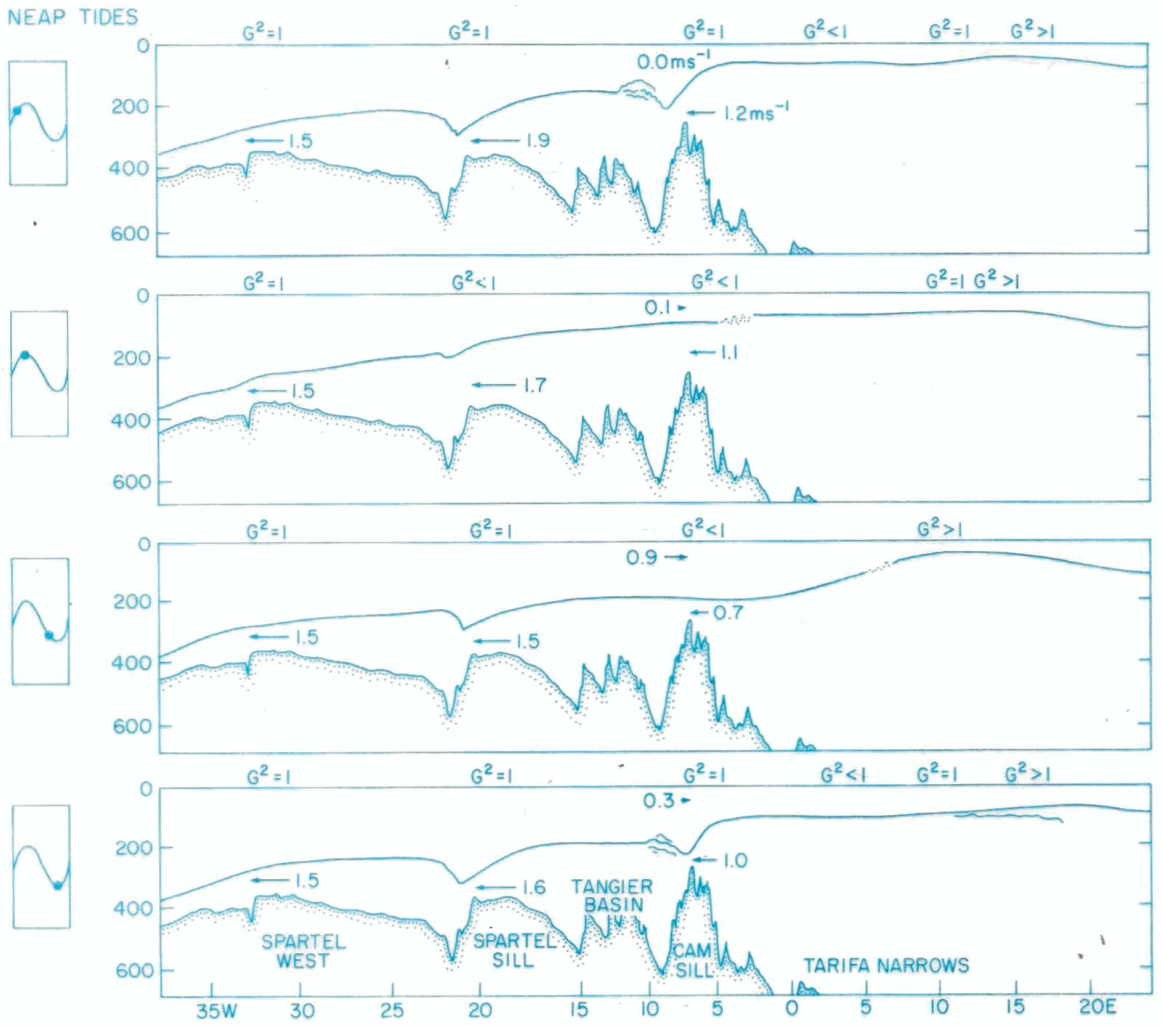


*Fig. 14.1b.* Schematic diagram summarizing the time dependent hydraulic response at different stages of the neap time. See text for details.

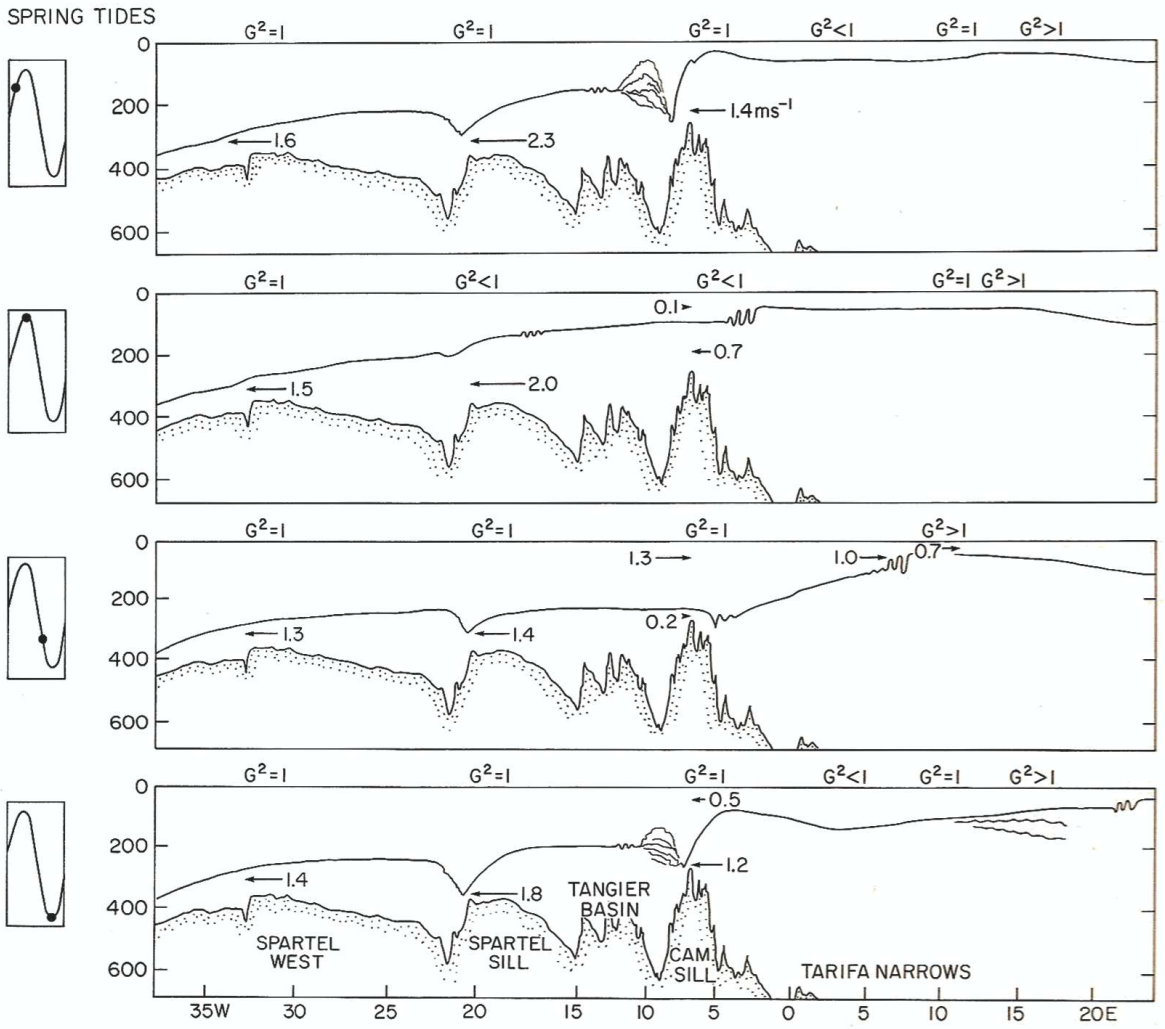


*Fig. 14.1a.* Schematic diagram summarizing the time dependent hydraulic response observed in the Strait of Gibraltar, at different stages of the spring tide. Flow velocities are representative of those discussed earlier in the paper. A detailed description of the processes sketched here is given in the text.

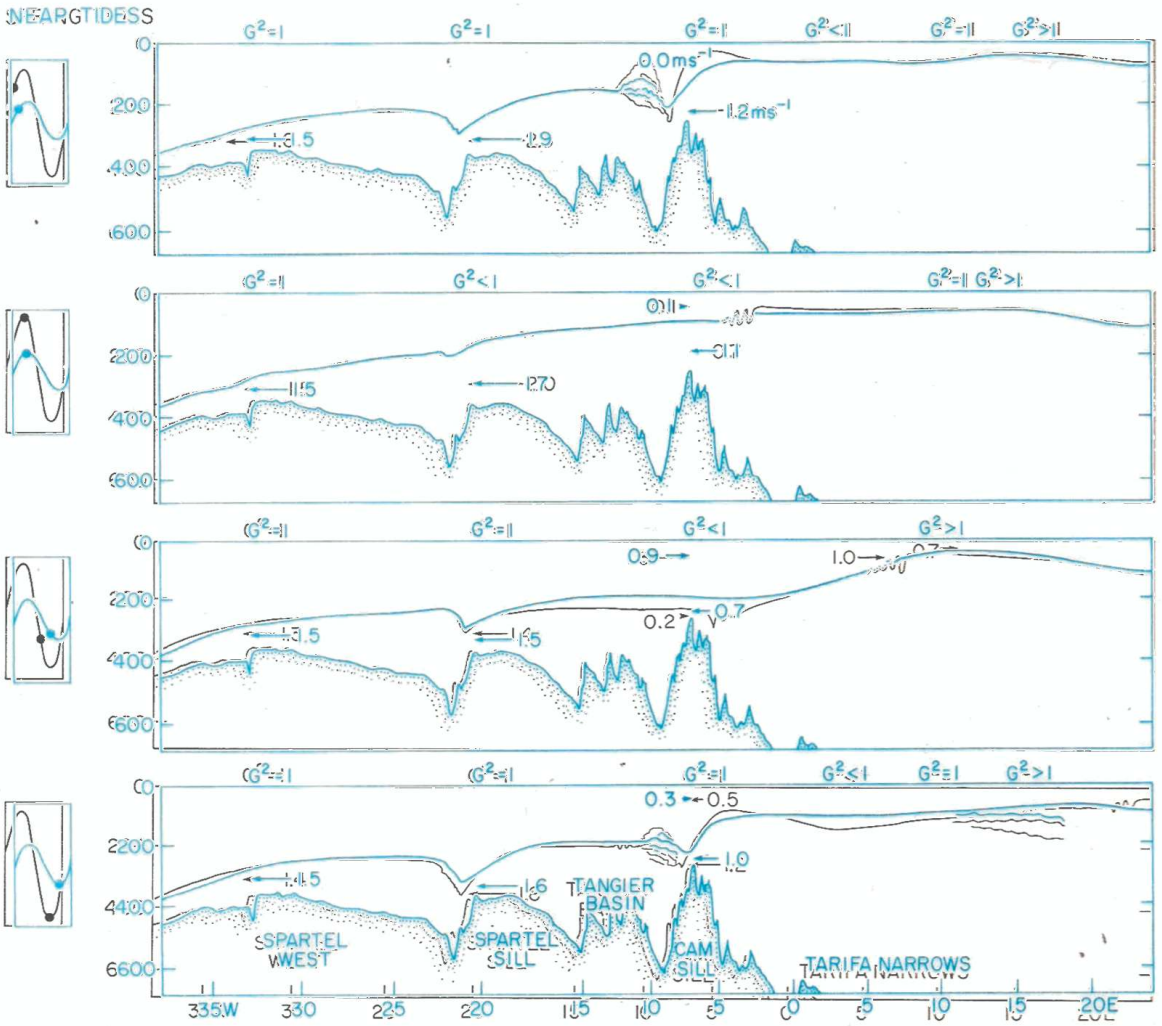


*Fig. 14.1a.* Schematic diagram summarizing the time dependent hydraulic response observed in the Strait of Gibraltar, at different stages of the spring tide. Flow velocities are representative of those discussed earlier in the paper. A detailed description of the processes sketched here is given in the text.

*Fig. 14.1b.* Schematic diagram summarizing the time dependent hydraulic response at different stages of the neap time. See text for details.